TESIS DE LA UNIVERSIDAD
DE ZARAGOZA
2024
276

Mohamad Asrardel

Isolated Droplet Evaporation Behaviors: An Integrated Experimental and Modeling Investigation

Director/es
Muelas Expósito, Álvaro
Ballester Castañer, Javier Manuel

ISSN 2254-7606

Prensas de la Universidad
Universidad Zaragoza

Universidad de Zaragoza
Servicio de Publicaciones

ISSN 2254-7606

Tesis Doctoral

ISOLATED DROPLET EVAPORATION BEHAVIORS: AN INTEGRATED EXPERIMENTAL AND MODELING INVESTIGATION

Autor

Mohamad Asrardel

Director/es

Muelas Expósito, Álvaro
Ballester Castañer, Javier Manuel

UNIVERSIDAD DE ZARAGOZA
Escuela de Doctorado

Programa de Doctorado en Mecánica de Fluidos

2024

PhD Dissertation

Isolated Droplet Evaporation Behaviors: An Integrated Experimental and Modeling Investigation

Author

Mohamad Asrardel

Thesis supervisors

Javier Ballester Castañer
Álvaro Muelas Expósito

Escuela de Ingeniería y Arquitectura

2023

To women of Iran

Acknowledgment

I extend my heartfelt gratitude to Prof. Javier Ballester for giving me the opportunity to undertake this doctoral thesis, and for his unwavering support, guidance, and counsel throughout the course of my PhD program. I would also like to express my appreciation to Dr. Alvaro Muelas, my co-supervisor, for his invaluable assistance and support in all aspects of my PhD journey, which has significantly shaped my research mindset.

I am deeply grateful to my colleagues at LIFEn, where I have had the privilege of collaborating with a remarkable group of people who have generously provided me with indispensable assistance over the years. I would like to express my gratitude to Álvaro Sobrino, whose guidance and expertise in working with micro-controllers were essential in initiating the research line of my thesis. I also extend my thanks to Santiago Jiménez for being always ready to solve any doubt related to optical instrumentations, and I reserve a special note of gratitude for Luis Ojeda, who assisted me in the preparation of experimental setups and troubleshooting laboratory issues. Furthermore, I express my appreciation to Taha Poonawala for his invaluable contributions to the design, construction, and execution of numerous experiments.

I would like to thank Antonio Pina and Olga Cebolla who deserve recognition for their indispensable assistance in processing the administrative aspects, including contracts, scholarships, procurement, shipping, and travel arrangements.

I would like to extend my gratitude to my former classmates, especially Dr. Ehsan Reyhanian and Dr. Mehdi Habibnia-Rami, for being the kind of friends anyone can wish for.

And last but not least, I am deeply indebted to my family, particularly my parents, sister, brother, and brother-in-law, Lena and Shaghayegh, for their unconditional support, which I hold in the highest regard.

Resumen

La combustión de *sprays* puede considerarse la tecnología dominante para la combustión de líquidos. La atomización del combustible líquido en pequeñas gotas aumenta la eficiencia del proceso de combustión, produciendo una mejor mezcla y una mayor liberación de energía a la vez que reduce la emisión de contaminantes. A pesar de su gran relevancia y uso generalizado, la combustión de *sprays* lleva aparejada importantes problemáticas, tanto ambientales como relacionadas con la salud. Abordar estos problemas de forma exitosa requiere una comprensión detallada del proceso de evaporación/combustión, para lo cual el estudio de gotas aisladas se convierte en una herramienta muy útil. Esta configuración canónica se utiliza habitualmente para simplificar el complejo proceso de la combustión de un *spray* ya que, a pesar de su simplicidad, retiene la mayor parte de los fenómenos que ocurren en la evaporación/combustión de líquidos. Por este motivo, la evaporación/combustión de líquidos ha sido abordada en esta tesis mediante el estudio de gotas aisladas.

Desde el punto de vista experimental, esta configuración simplificada proporciona la ventaja de tener un control estricto de todas las condiciones relevantes en el proceso, asegurando de este modo que los resultados obtenidos son intrínsecos del combustible ensayado. En este trabajo se ha utilizado dos instalaciones de combustión de gotas, denominadas como *Droplet Combustion Facility* (DCF) y *Suspended Droplet Facility* (SDF). La primera instalación fue diseñada siguiendo el concepto de gotas en caída libre, mientras que la segunda ha sido desarrollada durante la presente tesis doctoral aplicando el método de la gota suspendida. El uso de estas dos instalaciones (complementarias en muchos aspectos, como se detallará más adelante) permite la caracterización detallada de un amplio rango de combustibles (compuestos puros, combustibles convencionales/alternativos, líquidos viscosos y/o cargados de partículas, etc.), así como de condiciones de operación (tamaño de gota, temperatura del ambiente, método utilizado para fijar las gotas, etc.).

Además de esta parte experimental, el otro pilar de la tesis consiste en el desarrollo y validación de modelos teóricos de evaporación de gotas adaptados al estudio de casos de relevancia práctica (en concreto, la simulación de combustibles multicomponentes y mezclas). De forma adicional, la presencia de fibras de suspensión para la gota o la existencia de un ambiente de alta temperatura (condiciones aplicadas en la SDF, así como en otras muchas instalaciones de la literatura) requiere el desarrollo de sub-modelos específicos que incluyan efectos adicionales, como la conducción de calor a través de las fibras o la absorción de radiación térmica. Estos modelos han sido validados de forma satisfactoria frente a resultados de la literatura, así como frente a datos experimentales generados en las instalaciones DCF y SDF.

Una vez validados, estos modelos constituyen una herramienta muy útil para la caracterización detallada de los comportamientos existentes en la evaporación de gotas. Sin embargo, se hace necesaria la cuantificación de las incertidumbres asociadas a sus predicciones, ya que el modelo

descrito basa su funcionamiento en varias simplificaciones e incertidumbres (p.ej., en cuanto a la estimación de las propiedades del combustible). En un trabajo específico se ha cuantificado el impacto de las incertidumbres existentes en las propiedades del combustible sobre la exactitud de las predicciones obtenidas con el modelo de evaporación. Este estudio se ha realizado mediante un detallado análisis de sensibilidad, que pretende ilustrar cómo se propagan las incertidumbres en las estimaciones de propiedades, generando a su vez incertidumbres en las características de evaporación predichas por el modelo. Una parte fundamental de este estudio consiste en la identificación de las propiedades con un mayor impacto en estas características de evaporación.

Uno de los principales objetivos en el contexto de esta tesis doctoral consiste en el empleo conjunto de las instalaciones experimentales y del modelo para cuantificar la desviación de los resultados experimentales con respecto al caso canónico unidimensional de referencia en el campo (es decir, la configuración simplificada donde la única transferencia de calor se produce mediante conducción a través de la entrefase gota-gas). Es bien sabido que las características de evaporación de gotas obtenidas en la mayoría de instalaciones están afectadas, en mayor o menor medida, por artefactos[1] experimentales. Estos artefactos se deben a la existencia de modos adicionales (y generalmente no deseados) de transferencia de calor entre la gota y el ambiente: conducción de calor a través de las fibras donde se sujeta la gota, absorción de radiación térmica emitida por llamas o por superficies sólidas a elevada temperatura, efectos convectivos externos al problema, etc. Estos modos adicionales de transferencia de calor aumentan el calor entrante a la gota, acelerando por tanto la evaporación y desviando los resultados experimentales respecto al caso canónico de referencia. Este estudio pretende cuantificar el efecto de estos artefactos en las características de evaporación para un amplio rango de condiciones experimentales. Para ello se han propuesto tres números adimensionales, obtenidos mediante un análisis teórico del problema, con el objetivo de parametrizar el impacto de cada artefacto experimental sobre la tasa de evaporación de la gota. Este novedoso enfoque ha sido validado mediante datos experimentales obtenidos en ambas instalaciones (SDF, DCF), así como mediante resultados publicados en la literatura. El amplio abanico de condiciones utilizadas en esta validación (en cuanto a tamaños de gota, material y tamaño de las fibras, tipo de combustible, temperatura del gas, etc.) demuestra la capacidad del método propuesto a la hora de capturar satisfactoriamente el impacto de estos artefactos experimentales bajo un amplio rango de condiciones.

Tras desarrollar y validar las herramientas experimentales y de modelaje descritas anteriormente, el siguiente paso en la presente tesis doctoral consiste en el desarrollo de metodologías que permitan emular los comportamientos de evaporación de gotas de combustibles líquidos convencionales (p.ej., queroseno o diésel). Sin embargo, existen dos principales dificultades para conseguir este objetivo. La primera de ellas es la gran complejidad química de estos combustibles, formados por cientos o incluso miles de compuestos, lo cual hace prácticamente imposible la simulación de estas mezclas en herramientas de modelaje multicomponentes. La

---

[1] Real Academia Española, 2023, definición 4: *en un estudio o en un experimento, factor que perturba la correcta interpretación del resultado*

segunda dificultad consiste en la falta de información detallada acerca de las propiedades físico-químicas de esta gran cantidad de compuestos. Una forma habitual de solventar estas dificultades consiste en la formulación de *surrogates*, es decir, de mezclas de un número limitado de compuestos puros bien caracterizados capaces de emular ciertos comportamientos del combustible objetivo. En este trabajo se propone un algoritmo novedoso capaz de formular este tipo de mezclas para cualquier combustible derivado del petróleo, utilizando para ello una combinación de resultados experimentales y del modelo de evaporación de gota. En este método se estiman las propiedades del combustible de acuerdo con una serie de compuestos hipotéticos (o pseudo-componentes), para los que están definidos todos los parámetros que pueden ser asignados a una molécula real (p.ej., peso molecular, temperatura y presión crítica, etc.). Este proceso se conoce como el método de descomposición en pseudo-componentes. El siguiente paso consiste en asignar el compuesto real más similar a cada pseudo-componente mediante la comparación de las propiedades más relevantes para la aplicación evaluada (evaporación a alta temperatura), obtenidas del análisis de sensibilidad descrito anteriormente. De esta forma se consigue una serie de compuestos puros capaces de emular el comportamiento evaporativo del combustible objetivo. La composición de cada uno de estos compuestos se determina utilizando una red neuronal artificial junto con un algoritmo de optimización multi-objetivo. Esta metodología sistemática ha sido validada mediante su aplicación a tres combustibles reales: diesel, Jet A y gasóleo de calefacción. En los tres casos, las características de evaporación de gotas para los *surrogates* desarrollados mediante esta metodología mostraron notables similitudes con los resultados experimentales de los combustibles objetivo.

Finalmente, se ha realizado un trabajo exploratorio con el objetivo de caracterizar el impacto de la adición de nanopartículas en las características de evaporación de gotas de un combustible diésel. Varios estudios en la literatura muestran que la adición de nanopartículas puede acelerar significativamente los procesos de evaporación y combustión de combustibles líquidos. Sin embargo, otros trabajos muestran comportamientos opuestos. En concreto, la aglomeración de estas partículas formando una cáscara cerca de la superficie de la gota suele mencionarse como un mecanismo que puede reducir significativamente la tasa de evaporación/combustión. En este estudio se ha caracterizado y cuantificado la influencia de algunas de las nanopartículas más comunes (óxido de cerio, alúmina y nanotubos de carbono) en los comportamientos evaporativos de gotas de diésel a elevadas temperaturas. Además, el método de formulación de *surrogates* descrito anteriormente se ha empleado para diseñar mezclas capaces de emular las características de evaporación de estos nanocombustibles, tratando por tanto de convertir la adición de nanopartículas en un cambio composicional en el *surrogate*.

Abstract

Spray combustion can be considered as a ubiquitous approach when it comes to liquid fuel combustion. The atomization of the fuel increases combustion efficiency, resulting in better mixing and higher energy release while also reducing the emissions of pollutants. Although spray combustion is a vital energy technology, it still entails significant environmental and health concerns. To address these, a comprehensive understanding of the fuel combustion/evaporation process is required. The study of isolated droplets is a common approach to simplify the complexities of spray combustion, providing a simplified, canonical configuration that, however, retains most of the relevant phenomena governing liquid fuel evaporation/combustion. This approach has been followed in the current thesis dissertation.

From the experimental point of view, this simplified configuration gives the advantage of having a strict control of all relevant conditions, ensuring that the results obtained are directly attributable to the tested fuel. Two types of isolated droplet setup are used in this study, namely the Droplet Combustion Facility (DCF) and the Suspended Droplet Facility (SDF). The former was designed according to the free-falling droplet approach. As for the later, it has been developed according to the tethered droplet concept during the course of this PhD study. Employing these two complementary facilities makes it possible to experiment with a wide range of fuels (e.g., pure compounds, conventional/alternative fuels, viscous and/or particle-laden fuels, etc.) and operating conditions (in terms of initial droplet size, ambient temperature, suspending medium, etc.).

Besides this experimental part, the other pillar of the thesis is the development and validation of theoretical models for droplet evaporation that are suitable for the study of cases of practical relevance (in particular, the simulation of multicomponent fuels and mixtures). In addition, regarding the evaporation of a fuel droplet suspended at fibers in the presence of a high-temperature environment (conditions applied at the SDF, as well as in many other test rigs in the literature), specific sub-models have been developed to consider the effects of heat conduction through the suspension fibers and the absorption of thermal radiation on the droplet evaporation process. These models could be successfully validated against data from the literature, as well as against the results obtained at DCF and SDF setups.

Once it is duly validated, a droplet evaporation model constitutes a valuable tool for the in-depth examination of the droplet evaporation behavior. However, it is imperative to rigorously assess the degree of uncertainty associated with model predictions. This is due to the fact that the model works on the basis of several assumptions and uncertainties, particularly when it comes to the estimation of fuel properties. As a result, it is essential to quantify the potential impact of uncertainties in fuel properties on the accuracy of model predictions. This task is accomplished through a comprehensive sensitivity analysis, which serves to elucidate how uncertainties in the estimation of each property contribute to uncertainties in the predicted droplet evaporation

characteristics, while also identifying the properties with a larger impact on the high-temperature vaporization behaviors.

A primary objective within the context of this doctoral thesis is to synergize both isolated droplet setups and the aforementioned model in order to quantify the deviation of the measured experimental results from the canonical, idealized 1-D case for droplet evaporation, where the only heat transfer mode is conduction through the gas-droplet interface. It is well known that the evaporation characteristics extracted at most isolated droplet facilities are influenced by experimental artifacts caused by some additional (and, typically, undesired) heat transfer modes. These include the conduction of heat through the support fibers, the absorption of thermal radiation stemming from hot surfaces/flames, and external convective effects. All these additional heat transfer modes enhance the heat input to the droplet, increasing therefore the droplet evaporation rate and deviating the experimental measurements from the canonical case usually sought in this kind of tests. Hence, the investigation here seeks to quantify the effects of these artifacts on enhancing the droplet evaporation rate at any set of experimental conditions. To this end, three non-dimensional numbers are proposed on the basis of a theoretical analysis to parametrize the significance of each experimental artifact and to evaluate their influence on the droplet evaporation rate. Employing experimental results obtained at the SDF and DCF, together with literature data, provided a comprehensive benchmark to validate this novel approach, which has proved a remarkable capability to capture the effect of these artifacts for a wide range of conditions (droplet size, fiber size and material, fuel type, gas temperature, etc.).

After developing and validating the required experimental and modeling tools used in this dissertation, the next step intends to establish methodologies to emulate the evaporation behaviors of conventional liquid fuels (e.g., kerosene or diesel fuel). However, there are two main difficulties which hinder achieving this goal. First, these fuels are multi-component in nature and composed of hundreds of different molecules, which makes it practically infeasible to consider all of them in any modeling process. Second, the detailed physicochemical properties of these real fuels (paramount requirements for modeling their behaviors, as proved in the previous uncertainty study) are usually lacking for such complex mixtures. A common approach to tackle these obstacles is the formulation of surrogates of the target fuel, consisting of a few well-characterized pure compounds. In this work, an innovative algorithm has been developed to formulate a surrogate blend for any petroleum-based fuel. This is achieved by combining experimental data and the droplet evaporation model. In the proposed method, the fuel properties are estimated according to a set of hypothetical components that have all of the state description parameters that can be assigned to a real molecule (e.g., molecular weight, critical temperature, critical pressure, etc.). This approach is also known as the pseudo-component break-down method. In the next step, the most similar real compound to each pseudo-component can be found by incorporating the set of most important properties, as evaluated by the previous sensitivity analysis. After defining in this unsupervised manner the surrogate palette, the composition of the surrogate mixture is determined by employing an Artificial Neural Network and a multi-objective optimization algorithm. This systematic methodology has been validated by applying it to three distinct real fuels of relevance: diesel, Jet A, and heating oil. In each case, the droplet evaporation characteristics based on the formulated surrogate blends exhibited a remarkable resemblance to the experimental results for the target fuels.

Finally, an exploratory work has been performed on the impact of nanoparticle (NP) additives on the evaporation characteristics of diesel droplets. The addition of nanoparticles has been reported in several studies to significantly enhance the vaporization and combustion behaviors of liquid fuels, whereas other works point to much less clear advantages. More specifically, the aggregation of the NPs into a shell-like structure close to the droplet surface has been commonly pointed out as a mechanism reducing the evaporation and combustion rates. Some of the most widely used nanoparticles, such as cerium oxide, alumina and carbon nanotubes have been used in this study to quantify the influence of these NPs on the diesel droplet evaporation characteristics at high-temperature, flame-like conditions. Furthermore, the surrogate formulation approach described previously has been also employed to formulate blends which can emulate the evaporation behaviors of these nanofuels, attempting to convert the addition of NPs into a shift in the surrogate composition.

Prologue

This document collects the works which have been accomplished as partial fulfillment of the requirements for the degree of Ph.D. at the University of Zaragoza. The work was carried out at LIFEn / Fluid Mechanics Group of the University of Zaragoza, under supervision of Prof. Javier Ballester and Dr. Álvaro Muelas.

The studies carried out focus on various aspects of the phenomenon of isolated droplet evaporation at flame-like conditions, which have been studied both at theoretical and at experimental level. The results obtained have been published in either scientific journals or international conferences. Some of these works constitute the main body of this dissertation, which are listed here below:

I. Asrardel, M., Muelas, Á., Ballester, J. (2019). Assessment of Uncertainties in Predicted Evaporation Rates of Diesel Droplets. Conference: 11th Mediterranean Combustion Symposium (MCS11), Tenerife, Spain.
II. Asrardel, M., Muelas, Á., Ballester, J. (2023). Pseudocomponent-Based Approach for the Formulation of Evaporation Surrogates of Practical Liquid Fuels. Combustion Science and Technology. 19:1-32.
III. Asrardel, M., Poonawala, T., Muelas, Á., Ballester, J. (2023). Assessment of Experimental Artifacts in Evaporation Tests on Isolated, Suspended Droplets. Conference: 11th European Combustion Meeting, Rouen, France.
IV. Asrardel, M., Poonawala, T., Muelas, Á., Ballester, J. Impact of Heat Transfer Due to Fiber Conduction, Radiation and Convection on The Interpretation of Experiments With Isolated Droplets, Combustion and Flame (Accepted).

Table of contents

Acknowledgment i

Resumen iii

Abstract vii

Prologue xi

Table of contents xiii

Nomenclature xv

1. Introduction 1
   1.1 Spray combustion and fuel vaporization 1
   1.2 The isolated droplet configuration 4
   1.3 Experimental setups and artifacts 7
   1.4 Evaporation modeling and related uncertainties 11
   1.5 Surrogate formulation 13
   1.6 Nanofuels 15
   1.7 Objectives and outline 17
2. Experimental methodology 19
   2.1 Droplet combustion facility 19
   2.2 Suspended droplet facility 23
   2.3 Droplet image processing 27
3. Droplet evaporation model 31
   3.1 Model description 31
      3.1.1 Conservation equations for gas and liquid phases 31
      3.1.2 Forced convection effects on isolated droplet evaporation 36
      3.1.3 Conduction of heat through the fiber and radiation absorption 37
      3.1.4 Solution procedure 40
   3.2 Model validation 41
      3.2.1 Validation of the model against literature data 41
      3.2.2 Validation of the model against DCF and SDF experiments 44
4. Influence of the fuel properties on droplet evaporation behaviors 49
   4.1. Motivation 49
   4.2. Case study and methodology 50
   4.3. Results: sensitivity analysis 53
   4.4. Results: uncertainty analysis 54

5. Impact of non-ideal conditions on isolated droplet experiments 59
  5.1. Experimental results 60
  5.2. Theoretical analysis of the artifacts 67
  5.3. Analysis and evaluation of the artifacts 69
    5.3.1 Analysis based on model predictions 69
    5.3.2 Analysis based on experimental data 73
6. Development of evaporation surrogates using a pseudo-component approach 79
  6.1 Composition and properties of the target fuels 79
  6.2 Multicomponent droplet evaporation model considering pyrolysis reactions 80
  6.3. Fuel properties and evaporation metrics 83
  6.4. Fuel surrogate modeling and optimization 84
  6.5. Results and discussion 89
    6.5.1 Diesel 89
    6.5.2 Jet A 93
    6.5.3 Heating Oil 96
7. Nanofuel droplet evaporation 99
  7.1 Nanofuel preparation 99
  7.2 Experimental results 100
  7.3 Surrogate formulation for nanofuel droplet evaporation 105
8. Conclusions 109
  8.1 Summary and concluding remarks 109
  8.2 Future work 112
9. Conclusiones 114
  9.1 Resumen y conclusiones 114
  9.2 Trabajos futuros 117
Appendices 120
  Appendix A: Radiation heat flux measurements for McKenna burner 120
  Appendix B: Gas temperature measurement at the SDF 122
  Appendix C: Methods for the estimation of thermophysical and transport properties 123
  Appendix D: Pseudo-component breakdown 127
  Appendix E: Pseudo-component properties 129
References 132

Nomenclature

a	Droplet radius, [μm]
B_t	Heat transfer number, [-]
CN	Convection number, [-]
C	Heat capacity, [J kg^{-1} K^{-1}]
c_k	Mass fraction of the kth component, [-]
d	Diameter, [μm]
D	Mass diffusivity, [m^2 s^{-1}]
$\bar{E}_a$	Radiation absorption efficiency factor, [-]
FN	Fiber number, [-]
f	Correction coefficient, [-]
g	Gravitational acceleration, [m s^{-2}]
h	Convective heat transfer coefficient, [W m^{-2} K^{-1}]
HHV	Higher heating value, [MJ kg^{-1}]
k	Thermal conductivity, [W m^{-1} K^{-1}]
K	Droplet evaporation rate, [mm^2 s^{-1}]
L_v	Latent heat of vaporization, [J kg^{-1}]
Le	Lewis number, [-]
m	Droplet mass, [kg]
$\dot{m}$	Evaporated fuel mass flow rate [kg s^{-1}]
$\overline{MW}$	Average molecular mass [kg mol^{-1}]
mtr_i^{exp}	ith evaporation metric extracted from experimental data, [-]
mtr_i^{mdl}	ith evaporation metric extracted from modelling results, [-]
n_f	Number of fibers, [-]
Nu	Nusselt number, [-]
O_i	ith cost function, [-]
P	Pressure, [Pa]
Pe	Péclet number, [-]
Pr	Prandtl number, [-]
q_{pyr}	Enthalpy of pyrolysis reaction, [MJ kg^{-1}]
$\dot{Q}$	Heat power, [W]
$\dot{Q}''$	Incident thermal heat flux, [W m^{-2}]
$\dot{q}$	Heat power absorbed per unit of volume, [W m^{-3}]
r	Radial coordinate, [m]
R_u	Universal gas constant, [J mol^{-1} K^{-1}]
Re	Reynolds number, [-]
RN	Radiation number, [-]
S_{ij}	Relative sensitivity of ith metric with respect to jth property, [-]
Sc	Schmidt number, [-]
Sh	Sherwood number, [-]
t	Time, [s]
t_c	Normalized heat-up time, [s mm^{-2}]

t_{20}	Normalized evaporation period from $d^2/d_0^2 = 0.6$ till $d^2/d_0^2 = 0.2$, [s mm^{-2}]
t_{60}	Normalized evaporation period from the ending of heat-up time till $d^2/d_0^2 = 0.6$, [s mm^{-2}]
t_t	Normalized total evaporation time, [s mm^{-2}]
T	Temperature, [K]
v	Velocity, [m s^{-1}]
w_i	Weight constant for ith evaporation metric, [-]
X	Mole fraction, [-]
$\mathcal{X}_j$	jth property of fuel, [-]
x	Spatial coordinate, [m]
Y	Mass fraction, [-]
$\mathcal{Y}_i$	ith metric extracted from the evaporation curve, [-]

Greek symbols

α	Thermal diffusivity, [-]
β	Volume expansion coefficient, [K^{-1}]
ε	Emissivity, [-]
μ	Viscosity, [Pa s]
ρ	Density, [kg m^{-3}]
Φ_{ij}	Similarity factor, [-]
ψ_i^{PC}	ith property for a given pseudo component, [-]
ψ_j^{Real}	jth property for a given real component, [-]
σ	Stefan-Boltzmann constant, [kg s^{-3} K^{-4}]
χ_M	Enhancement coefficient for liquid mass diffusion coefficient, [-]
χ_T	Enhancement coefficient for liquid thermal conductivity, [-]
Ω	Solid angle, [Steradian]
$\forall_{net}$	Net droplet volume, [m^3]

Subscripts and superscripts

0	Initial
b	Boiling
c	Critical
can	Canonical case
cn	Forced convection
d	Droplet
exp	Experimental value
eff	Effective
fc	Fiber conduction
f	Fiber
fu	Fuel
g	Gas phase
gc	Gas conduction
l	Liquid phase

mix	Average gas film properties
n	Nominal values
p	Constant pressure
qs	Quasi-steady
rd	Radiation
ref	Reference state
s	Droplet surface
sb	sensible heat
t	Total
thc	Thermo-couple
v	Vapor phase
$*$	Modified
$\cdot$	Time-derivative
∞	Far field

1. Introduction

1.1 Spray combustion and fuel vaporization

It is well known that the global energy model is changing and must continue to evolve until a new sustainable balance is reached. Although in recent years many energy sources have emerged and are growing unstoppably, the reality is that, currently, a vast majority of the energy consumed worldwide has an unsustainable origin. Despite the growing interest in renewable and sustainable energy sources like wind, solar, and biomass, unsustainable fuels remain the dominant energy source worldwide, accounting for 70% of the European Union's energy supply in 2022 (IEA, 2022). More specifically, the vast majority of these unsustainable resources are related to the use of fossil fuels. Among them, petroleum-based liquid fuels (e.g., diesel or kerosene) provide 35.1% of the total energy in Europe, followed by natural gas and coal at 23.1% and 9%, respectively. Notably, the transportation sector is among the primary consumers of petroleum in Europe, accounting for 60% of its usage (IEA, 2022). However, the consumption of liquid fuels is not just limited to transportation systems; they are extensively used in various industry sectors through spray combustion systems such as gas turbines, boilers, industrial burners, and furnaces. Because of liquid fuels' high volumetric energy density, ease of storage, handling and transportation, as well as the likelihood that they can be employed for a wide variety of purposes, liquid fuels have received significant attention in power generation and industry applications.

Figure 1.1 shows the worldwide demand for different fossil fuels since 1990 and the expectations for consumption up to 2050, as provided by (IEA, 2022). As shown, the demand for oil has had rising trends in recent years and is expected to peak in the middle of the 2030s before reaching its plateau state (IEA, 2022). However, the reliance on combustion processes poses problems such as source depletion and, at the same time, is associated with environmental sustainability concerns. For instance, carbon dioxide (CO_2), a prominent greenhouse gas, is released upon fossil fuel combustion, contributing to the phenomenon of global warming (Allen et al., 2009; Matthews et al., 2009; Meinshausen et al., 2009). Additionally, incomplete combustion can produce soot, a hazardous byproduct. The inhalation of these soot particles has been linked to severe health implications, such as cancer, respiratory diseases and cardiovascular dysfunctions (Niranjan & Thakur, 2017). These concerns have galvanized the scholarly community to seek solutions for improving the efficiency of spray combustion, reducing the emissions, or even replacing conventional fuels by more environmentally-friendly and sustainable alternatives which can meet health and environmental requirements.

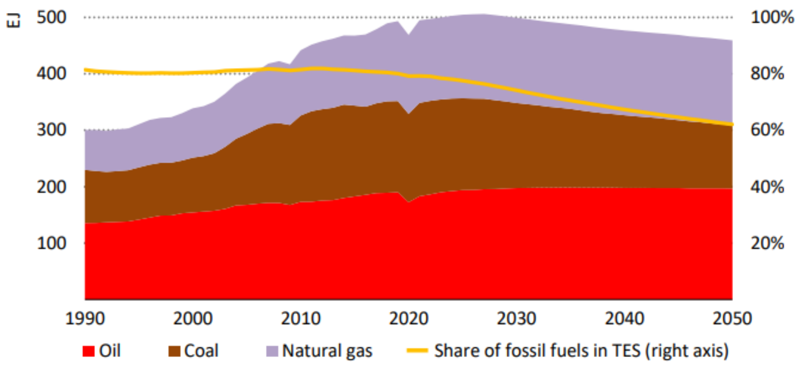

Figure 1.1, Fossil fuel demand since 1990 and projections towards the year 2050 (IEA, 2022)[2]

Since most combustion applications burn liquid fuels in the form of a spray, a successful implementation of these solutions requires a comprehensive knowledge of the spray burning process. Spray combustion is a remarkably complex process that can be broadly subdivided into four principal stages: atomization, evaporation of the fuel, the creation of a combustible mixture and the combustion of that mixture (Warnatz et al., 2006). Typically, the fuel spray is generated by the forceful injection of the liquid through a nozzle at high pressures into the combustion chamber, which is generally characterized by elevated temperatures. Upon exiting the nozzle, the liquid jet assumes a conical shape, forming a spray, as depicted in Figure 1.2.

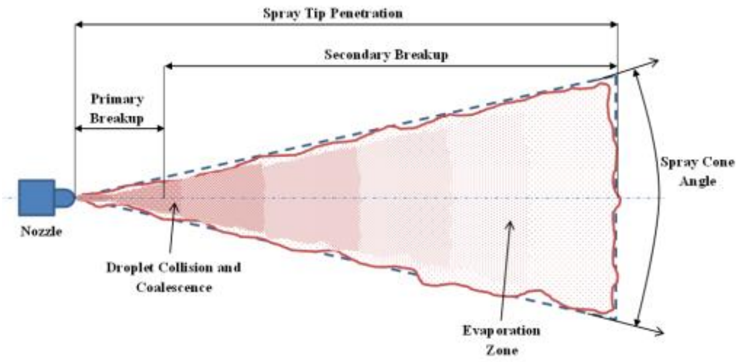

Figure 1.2, Spray formation and breakup. Reproduced from (Baumgarten, 2006).

In the context of applications involving spray combustion, it is imperative that the liquid fuel undergoes a series of pre-combustion processes before releasing its chemical energy. One pivotal phase in this sequence involves the conversion of the liquid fuel into vapor, which subsequently mixes with the oxidizer. This transformation necessitates the atomization of the liquid into tiny droplets to increase the liquid surface-to-mass ratio, leading to an increase in evaporation rates and eventually improving combustion efficiency (Bayvel, 2019). In contrast to the homogeneous gaseous mixtures in premixed combustion, spray combustion involves the presence of discrete

---

[2] Note: EJ = exajoule; TES = total energy supply.

liquid droplets, displaying variations in size and velocity. This inherent non-uniformity within the combustible mixture leads to irregularities in the propagation of the flame throughout the spray (Williams, 2013). Moreover, this also causes the onset of hot spots related to NO_X emission, while rich regions lead to soot/UHC emission. The atomization of the fuel into fine droplet size distributions and a well-mixed post-spray regime can contribute to the reduction of these emissions.

In the flame, the generated droplets within a spray stream undergo evaporation, often occurring in high-temperature and low-oxygen environments such as those prevailing in the group combustion/evaporation regime (Sánchez et al., 2015). The fuel vapors later react with the oxidizer in the surrounding ambient, releasing the energy to sustain the process. The intricate dynamics of this high-temperature droplet evaporation plays a pivotal role in influencing the general characteristics of the spray combustion systems (Sirignano, 1983). The droplet's heat balance is principally governed by conductive and convective heat transfer, although thermal radiation may also play a noteworthy role at high radiation heat flux conditions (Baek et al., 1999). Regarding mass transport, the convection and diffusion mechanisms facilitate the transfer of fuel vapor to the hot ambient gas. Factors influencing the magnitude of mass transfer include the thermo-physical and transport properties of both gas and fuel, volatility characteristics of the target fuel, droplet size, and the relative velocity between the droplet and combustion air (Bayvel, 2019).

On the one hand, the consequences of inadequate vaporization can be severe, potentially leading to unburnt fuel emissions and also to high-temperature regions that amplify nitrogen oxide (NO_X) formation, diminish combustion stability, and cause engine failure (Correa, 1993; Huang & Yang, 2009; Lefebvre & Ballal, 2010). As such, applications necessitating steady combustion, such as gas turbines, call for a meticulously uniform mixture of fuel vapor and air to minimize emissions (Lefebvre & Ballal, 2010). Thus, an equable temperature field devoid of localized high-temperature zones is imperative, given the exponential growth of NO_X formation rate with temperature (Correa, 1993). Homogeneous droplet vaporization and, consequently, reduced emissions can be attained through a monodisperse spray. However, real-world sprays often exhibit a relatively broad droplet size distribution (Babinsky & Sojka, 2002). Smaller droplets in heterogeneous sprays promote ignition, whereas larger droplets may lack adequate time for evaporation, culminating in localized increases in combustion temperature (Lefebvre & Ballal, 2010) and higher UHC emission (Ballester & Dopazo, 1994). Thus, the spray's size distribution must align with the specific requirements of the application, and the combustion system design has to comply with the requirements of droplet evaporation at high temperatures.

In summary, the relevance of the atomization and evaporation processes is manifest in all power units where spray combustion plays a role, such as internal combustion engines, gas turbines, liquid rocket engines and industrial furnaces. Besides these relevant combustion applications, droplet evaporation also finds application in fields such as spray drying, fire safety, and evaporative cooling, primarily concerning the evaporation of water or water-based solutions (Sirignano, 2010).

1.2 The isolated droplet configuration

As detailed before, liquid sprays encompass a wide range of droplet sizes, which exhibit different combustion histories depending on the specific conditions faced by each individual droplet. This presents a substantial challenge when attempting to ascertain the inherent behavior of a fuel through experimental investigations involving spray flames. For instance, the oxygen concentration seen by individual droplets significantly varies within the different spray regions. While certain droplets may undergo vaporization and combustion in oxygen-rich environments, the majority of the liquid is vaporized within the flame core, typically characterized by low or even negligible oxygen levels (see Figure 1.3). Therefore, the evaporation of droplets at high temperature and low oxygen environments presents an unquestionable scientific interest. Besides this change in oxygen levels across the combustion chamber, the marked multicomponent nature of most real fuels implies an equally challenging shift in fuel composition, with more volatile compounds prevailing close to the injection and the heaviest fractions being released further downstream.

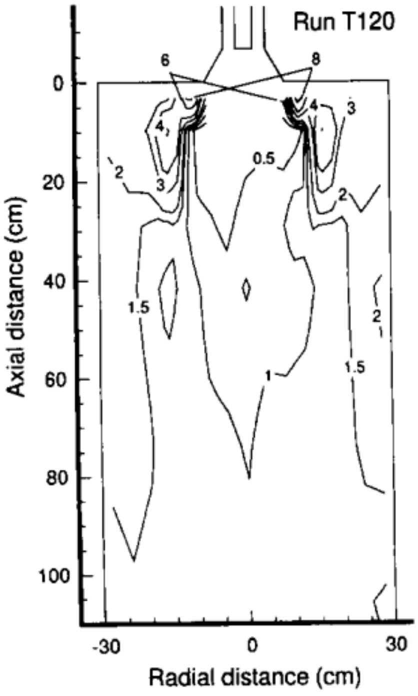

Figure 1.3, Experimental measurement for spatial distribution of O_2 (%vol.) for heavy fuel oil-water spray combustion (Ballester et al., 1996)

Given all these complexities, an elementary approach to study the spray combustion phenomena would involve viewing the fuel spray as a compilation of individual droplets. Although there are many different phenomena that accompany droplet evaporation/combustion at spray conditions (e.g., droplet-droplet interactions, turbulence, multiphase flow, etc.) (Annamalai & Ryan, 1992), investigations conducted on isolated droplets have proven to yield invaluable data under meticulously controlled conditions,. Furthermore, experiments with isolated droplets can provide opportunities to independently examine the impact of each parameter. In cases where the flow field is simple enough, the combustion/evaporation process of an isolated droplet could serve as the subject for comprehensive theoretical and experimental studies. Therefore, it can be beneficial to view single droplet combustion as a practical scenario to gain insight into the intricate phenomena governing liquid fuel combustion (Law, 1982).

The canonical configuration for a single, isolated droplet has been frequently adopted as benchmark for characterizing liquid fuel combustion and evaporation. In case the test conditions are simple enough, this problem becomes 1-D, significantly easing modeling efforts as well as results interpretation. Namely, if the droplet is mono-component, it vaporizes under a constant hot gas temperature, the only heat transfer mode is heat conduction through the gas-liquid interface and natural and forced convection effects are absent, then the problem becomes sphero-symmetric, with the droplet and the diffusion flame (for cases with oxygen in the gas atmosphere) maintaining perfectly spherical and concentric shapes, as depicted in Figure 1.4.a. Furthermore, in this scenario, the square of the droplet diameter (d_d^2) is found to decrease linearly with time, being its time-derivative referred to as the droplet evaporation rate ($K= -\mathrm{d}(d_d^2)/\mathrm{d}t$), constant throughout all the process. This behavior is called the d^2 law (Godsave, 1953; Spalding, 1950). In case the droplet immediately starts its quasi-steady evaporation process without need for initial heating (i.e., all heat input to the droplet is used to vaporize), the temporal evolution of the droplet size would be reduced to:

$$d_d^2 = d_0^2 - Kt \qquad (1.1)$$

Being d_0 the initial droplet size and t the time. This simplified configuration affords a significant ease in the interpretation of experimental results and also in the comparison with mathematical models (Avedisian, 2014). Due to this, most droplet vaporization and combustion models are typically developed for spherically symmetric conditions (Farouk & Dryer, 2011; Farouk & Dryer, 2012; Liu et al., 2013). Although this simplified configuration presents numerous advantages, its practical implementation poses challenges in the context of real-world testing setups, raising concerns about the feasibility of consistently maintaining experimental parameters to uphold this desired state. In other words, external factors (e.g., relative velocity between the droplet and the coflow, absorption of thermal radiation, etc.) during experiments can lead to significant deviations from this ideal, canonical configuration.

It is well known that the onset of forced/natural convection can distort the droplet evaporation profiles into a 2-D configuration (as shown in Figure 1.4.b). To accommodate for these convective effects, a series of experimental investigations have been undertaken to propose empirical correlations (e.g., see (Williams, 2013)) to estimate the enhancement effect of convection on droplet evaporation; one of the most widely adopted is the equation developed by Wise and Agoston (1958):

$$K = K_{\mathrm{can}}(1 + 0.24Re^{1/2}Pr^{1/3}) \tag{1.2}$$

Where Re and Pr are the Reynolds and Prandtl numbers of the flow around the droplet, and K_{can} is the evaporation rate defined for the canonical case, under the assumption of spherical symmetry. Regarding the effect of natural convection, Chauveau et al. (2008) studied n-heptane droplet evaporation under varying environmental conditions, encompassing scenarios both with and without the influence of natural convection. They proposed the following correlation to consider the effect of buoyancy on an evaporating droplet:

$$K = K_{\mathrm{can}}(1 + 0.25\mathrm{Gr}^{1/4}Pr^{1/3}) \tag{1.3}$$

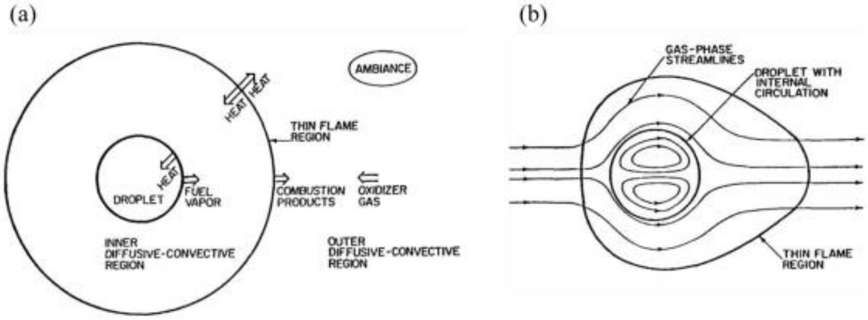

Figure 1.4, Schematic flow configuration of: a) spherically symmetric droplet combustion and b) convective droplet combustion (Sirignano, 2010)

To remove the effect of natural and forced convection (so that the canonical, spherico-symmetrical configuration is attained), Re and Gr numbers should therefore be zero or very small:

$$Re = U_g d_d / \nu \tag{1.4}$$

$$Gr = g\beta(T_s - T_g) d_d{}^3 / \nu^2 \tag{1.5}$$

From Equation (1.4), it can be inferred that using small droplets or reducing the relative motion of the droplet with respect to its surrounding medium can result in a significant reduction in the Re and, eventually, in the impact of forced convection.

Regarding natural convection, Equation (1.5) offers several approaches to achieve a small *Gr*, such as reducing gravity and using small droplets. As for the former approach, gravity reduction has been frequently adopted to provide operation conditions close to a strictly 1-D configuration. Microgravity conditions can be achieved either by dropping the experimental setup in a drop tower (Liu et al., 2013), conducting tests in a parabolic flight (Chauveau et al., 2011) or even by performing experiments aboard the International Space Station (Dietrich et al., 2015; Dietrich et al., 2014). However, such experiments are limited due to their high costs. Reducing droplet initial size is an effective and affordable solution to reduce the effects of natural convection. For instance, in a recent study, employing a droplet size below 400 µm was reported to diminish the buoyancy-induced effects on the droplet evaporation curve to a point where they become negligible (Wang et al., 2021). Therefore, ground-based isolated droplet facilities are deemed viable candidates for emulating the canonical state if specific criteria are considered. In the following section, further discussion will be presented regarding different isolated droplet facilities and their key features.

1.3 Experimental setups and artifacts

In the framework of ground-based droplet evaporation setups, these facilities can be categorized into three main experimental techniques: suspended droplet, free falling droplet and levitating droplet test rigs (see Figure 1.5). In the following, a brief comparison of these methods, including their mechanisms, advantages, and limitations, will be provided.

The tethered droplet approach is probably the most utilized technique in the literature. Droplets are suspended in a support medium (see Figure 1.5.a), typically quartz fibers (Ghassemi et al., 2006; Ma et al., 2015), ceramic fibers (Wu & Yang, 2016; Yang & Wu, 2017), or thermocouple junctions (Wang et al., 2019; Wang et al., 2018; Zhang et al., 2018; Zhang et al., 2017), in order to study their evaporation/burning. This method offers the advantage of easing the droplet generation process and, since the droplet remains completely static, facilitating the measurement of droplet parameters. Furthermore, optical apparatuses can be conveniently set up to record the whole temporal history of a given droplet, which is very advantageous for the study of stochastic behaviors such as the expelling of child droplets during microexplosion and puffing events. However, the method does have its drawbacks, such as the potential influence of the suspension fiber. The support fiber has been reported in some works (Chauveau et al., 2019; Wang et al., 2020; Yang & Wong, 2001, 2002) to introduce thermal conduction into the droplet, significantly enhancing its evaporation rate (as it will be discussed in detail further on). Additionally, the fiber can also serve as a heterogeneous nucleation site, leading to internal boiling and potentially inducing micro-explosions (Lasheras et al., 1980). In addition, this kind of setups usually deploy quite large droplet sizes (sometimes even larger than 1 mm), which can behave differently from smaller droplets due to the different relative importance of the various physical phenomena such as natural convection (Verwey & Birouk, 2018). Tests with large droplets also potentially result in the formation of ellipsoidal-shaped droplets, introducing uncertainty in defining the droplet diameter and, therefore, in the quantification of the droplet size-related metrics (e.g., Kumagai et al. (1971) noted that the value of the burning rate constant was highly sensitive to how the droplet diameter was defined).

The free-falling droplet method (Lai & Pan, 2023; Law, 1982; Á. Muelas et al., 2019; Shaddix & Hardesty, 1999) allows droplets to fall freely within an enclosure. In this technique, no suspension medium is involved, avoiding the disturbance of the droplet's shape or the introduction of extra heat flux through fiber conduction. Since piezoelectric devices are typically used for droplet generation, smaller droplet sizes are usually tested, reducing the impact of natural convection effects. However, when it comes to measuring the temperature evolution for an evaporating droplet, this facility presents challenges due to its requirements for advanced equipment such as rainbow refractometry or Laser Induced Fluorescence (LIF) (Laurent et al., 2006; Rosebrock et al., 2016; Wu et al., 2019). Furthermore, another limitation of this approach is that it is typically not possible to capture the full history of a given droplet, limiting the study of fast and stochastic phenomena such as puffing and micro-explosion (Jüngst et al., 2022). Moreover, the varying relative velocity between the droplet and the surrounding gas during the falling motion may create a convective environment that modifies the evaporation behavior of the isolated droplet.

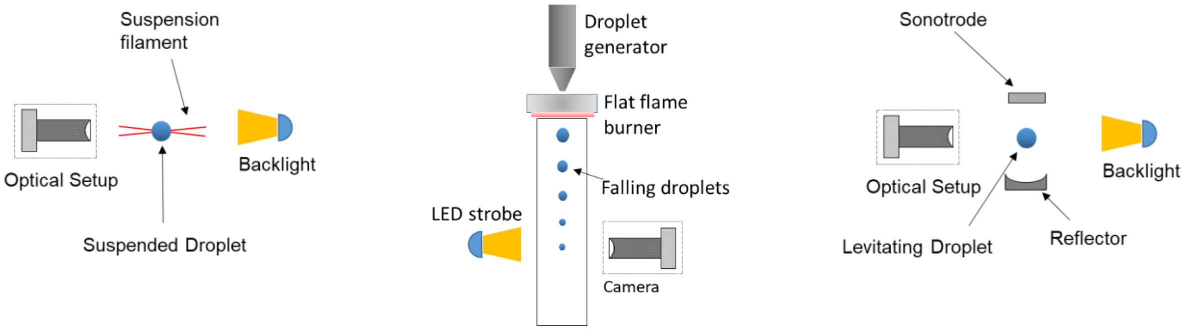

a) suspended droplet *b) free-falling droplet* *c) levitating droplet*

Figure 1.5, Different isolated droplet facilities

Finally, in the levitation technique (Grosshans et al., 2016; Marzo et al., 2017; Potts et al., 2001), the gravitational force acting on a droplet is balanced by mechanisms such as magnetic fields (for ferromagnetic droplets (Potts et al., 2001)) or acoustic waves (Marzo et al., 2017), that keep the fuel droplet levitating at a fixed location. For instance, using the acoustic levitation method makes it possible to suspend small objects (with a diameter smaller than 5 mm (Marzo et al., 2017)) with densities as high as tungsten (Brandt, 2001). This method ensures that the droplet can freely stay at a desired location for a long time without the participation of a suspension medium, which makes it suitable for studies related to droplet evaporation (Grosshans et al., 2016). However, there are also relevant limitations in this method, such as the considerable time required for placing the levitating droplet at a proper location, which can cause droplet evaporation while the test conditions are under preparation. Furthermore, there is a limitation in the environment temperature, which restricts this approach to low-temperature evaporation. It is also pertinent to note that the levitation of fuel droplets caused by either acoustic or magnetic fields may influence the droplet shape, which eventually increases the droplet evaporation rate due to higher aspect ratio and surface area (Yang et al., 2023).

Regardless of the kind of facility, many researchers have focused on isolated droplet studies as a controlled framework to delve into different aspects of fuel droplet evaporation. For many applications, it is essential that the experimental apparatus mirrors the canonical setting typically sought in such tests (i.e., a 1-D problem where the only heat transfer mode is conduction through the gas-liquid interface). As discussed before, this significantly simplifies interpretation of results and comparisons with theoretical models (Avedisian, 2014)). Nevertheless, at real-life isolated droplet facilities, some undesired effects (*experimental artifacts*) can be present in the experiments, introducing some departure from this ideal scenario. Namely, heat conduction through the supporting fibers, external convection or absorption of thermal radiation may affect heat transfer and, hence, evaporation behaviors. Given that most experimental setups exhibit one or more of these 'experimental artifacts', understanding their role and assessing their magnitude is crucial for an accurate interpretation of the results, whether for model validation or for fuel behavior characterization.

As introduced before, the suspension of droplets on fibers is a common approach for the experimental characterization of droplet behaviors. However, the conduction of heat through the fibers can induce significant deviations from the assumed configuration. The magnitude of this conduction artifact depends on factors such as the fiber diameter and the material used. The literature offers a wide diversity when it comes to these suspension materials, although the more common ones are quartz (Chauveau et al., 2019), silicon carbide (Farouk & Dryer, 2011), or thermocouple wires (Han et al., 2016). Some studies have found that this fiber conduction artifact can lead to overestimating the evaporation rate, even doubling its true value (Chauveau et al., 2019), or artificially causing internal droplet bubbling or micro-explosions, which do not actually occur for unsuspended droplets (Setyawan et al., 2015; Wang et al., 2020).

Chauveau et al. (2019) investigated fiber heat conduction on n-heptane droplet evaporation under various conditions, suggesting a crossed configuration of 14 μm silicon carbide fibers to mitigate this effect. They observed a linear relationship between the measured droplet's evaporation rate and the square of the fiber diameter. Wang et al. (2020) studied single droplet evaporation using suspension fibers made of different materials. They concluded that a suspension fiber with $d_f <$ 100 μm and $k_f <$ 80 W/m/K has a negligible impact on the droplet evaporation rate. Yang and Wong (2002) studied the same effect on n-heptane and n-hexadecane droplets using different suspension fiber diameters, ambient temperatures and initial droplet sizes. They found an inverse correlation between the d_0/d_f ratio and the droplet evaporation rate (K), recommending the use of a single quartz fiber with d_f = 50 μm to minimize fiber conduction effects. Han et al. (2016) found that using a thermocouple as suspension medium can significantly increase the droplet evaporation rate. Setyawan et al. (2015; 2016) investigated the combustion of pure glycerol suspended on a 142 μm SiC fiber, noting unexpected fluctuations in the evaporation curve. Since pure glycerol should evaporate smoothly without any puffing, the observed bubbling suggests heterogeneous nucleation at the hot fiber surface (Jackson & Avedisian, 1998). Farouk and Dryer (2011) recommended d_0/d_f >38 as a safe criterion to minimize the fiber conduction effect for d_f =45μm SiC rod arrangements in n-heptane combustion. In the same line, Avedisian and Jackson (2000) recommended d_0/d_f >13 to mitigate the impact of a suspending quartz fiber on the burning rate of n-heptane, recovering the burning rate of a fiber-free droplet. As it can be noticed from this literature survey, the recommended criteria proposed in previous works to avoid the fiber conduction artifact are quite diverse and, in some cases, even contradictory. Whereas some studies only consider the effect of the fiber size, others propose the d_0/d_f ratio as the key parameter. Others suggest dimensional thresholds based on fiber size and, sometimes, thermal conductivity. These works provide valuable analysis, but they are focused on particular conditions and are difficult to generalize to other situations.

Droplet evaporation rate can also be increased by the presence of radiating objects near the droplet (typically, hot solids or flames). Several studies have shown that the effect of thermal radiation absorption by the droplet can become considerable at high temperatures, significantly decreasing the droplet's lifetime (Fang et al., 2019). Long et al. (2015), through a modeling approach, found that there is a critical droplet diameter below which the impact of radiation absorption can be assumed as negligible. Gan and Qiao (2012) quantified the evaporation rates of ethanol droplets exposed to different levels of radiation heat flux at room temperature, observing an increase of 12.4% in evaporation rate for ethanol when the radiation intensity was raised from 75 to 175 W. These studies confirm that radiation effects should be accounted for to correctly interpret experimental results on droplet evaporation. However, and similarly to the previously discussed effect of the fiber, most works are devoted to partial aspects of this experimental effect, with difficult generalization to other set of conditions.

Finally, gas-droplet heat exchange, and hence evaporation rate, can also be enhanced due to forced or natural convection. Hence, depending on the experimental conditions (e.g., droplet size, gas temperature, etc.), buoyancy-induced flows can noticeably enhance the evaporation rate compared to the canonical problem (Chauveau et al., 2019). This is quite common since, as detailed before, most literature data on droplet evaporation relies on tests performed under normal gravity. If the droplet is not in a stagnant ambient, forced convection may also enhance the evaporation rate, as it can be readily estimated through several models which include this effect through the inclusion of the Nusselt and Sherwood numbers to the gas-phase equations (e.g., see (Abramzon & Sirignano, 1989)).

Given the great relevance of experimental results from single-droplet setups for the generation of reference data on droplet evaporation and combustion, all these potential sources of bias and uncertainty need to be duly addressed from a more general perspective.

1.4 Evaporation modeling and related uncertainties

Real fuels are chemically complex and typically consist of hundreds of compounds with diverse physico-chemical properties. Conventional fuels (e.g., diesel or Jet A), in particular, exhibit a wide range of relative volatility in their compositions. Highly volatile components, such as low-carbon number alkanes (e.g., heptane), tend to evaporate rapidly at the liquid-vapor interface in comparison with low-volatile compounds. This results in gradient mass fractions for different compounds inside the droplet, leading to a faster depletion of the lighter components. This complexity makes the evaporation of multi-component droplets a challenging process. Comprehensive modeling of multi-component fuel evaporation necessitates the consideration of the different processes involved and, at the same time, heavily relies on a precise knowledge of thermo-physical properties. In this section, the current knowledge related to the droplet evaporation model is briefly reviewed and some uncertainties related to an imprecise knowledge of liquid properties are identified.

As a pioneering work on droplet evaporation modeling, one of the earliest models was proposed by Maxwell (1890). The model could predict the droplet evaporation behavior during the steady state where the droplet evaporation rate is primarily controlled by molecular diffusion. Although the simplicity of the model made it a proper candidate for being embedded in computational fluid dynamic (CFD) codes, this model suffered from a major limitation in neglecting Stefan flow, which is the convective flow of vapor stemming from the droplet surface, especially relevant at high temperature conditions (Sazhin, 2014).

A significant advancement in the modeling of droplet evaporation was achieved with the introduction of the d^2-law for mono-component fuel droplets by Spalding (1950) and Godsave (1953). The d^2-law characterizes the steady evaporation of a droplet after an initial transient heat-up period, where the square of droplet diameter, and consequently droplet surface area, decreases linearly with time (as detailed in section 1.2). This model, rooted in analytical considerations, initially neglected temperature gradients within the droplet, but the gas-phase equations it presented served as the foundation for subsequent models. The main assumptions (Godsave, 1953), which were taken into consideration in this model, are the following:

- Isolated droplet (no droplet-droplet interaction).
- No chemical reactions.
- Single component fuel.
- Quasi-steady gas phase due to its shorter response time in comparison with the liquid.

- Spherical symmetry condition due to the absence of convective forces
- Constant gas phase properties, which are evaluated at a reference temperature and composition.
- Constant vapor phase pressure (i.e., fixed temperature of the liquid).
- Ideal vapor-liquid behavior.
- Rapid mixing in the droplet (i.e., no temperature gradients inside the liquid).

Several authors made further refinements to these classical models. Abramzon and Sirignano (1989) investigated the inclusion of convective transport due to droplet-gas relative velocity using the concept of film theory. The film theory assumes that the resistance to heat and mass transfer which occurs between the droplet surface and the surroundings can be modeled by employing the idea of a gas film that surrounds the evaporating droplet (Abramzon & Sirignano, 1989). This film is composed of a layer of hot gas mixture near the droplet surface in which the fuel vapor mass concentration is considerable. The presence of this film layer can hinder the mass and heat diffusion rates. Furthermore, their model (A-S model) considers temperature gradients within the droplet, with the liquid phase being modelled as 1-D (in contrast to previous models considering rapid mixing inside the droplet). The effect of internal circulation resulting from droplet movement was accounted by employing the concept of an enhanced, effective thermal conductivity. Although this model shows remarkable performance in emulating the droplet evaporation rate, the computational demands of its application for every droplet in a spray remain considerably elevated.

In the realm of computational fluid dynamic codes, liquid fuels are typically represented by a single component. Yet, these mono-component fuel models fall short when attempting to emulate the intricate behaviors of multi-component fuels such as gasoline and diesel (Lippert, 1999), which require the incorporation of additional components (Ra & Reitz, 2009). In other words, the evolution of the vapor release from distinct constituents of real fuel depends on the relative volatilities of different compounds present within a multicomponent droplet. As a result, the composition of the vapors for an evaporating multicomponent droplet is subject to continual changes. This relevant characteristic, inherent in the majority of real fuels due to their multicomponent nature, remains beyond the scope of simulation using mono-component models.

Sazhin et al. (2010) adopted a binary-component mixture to characterize fuel droplet composition and expanded upon the Abramzon and Sirignano ‘Effective Conductivity Model’ (Abramzon & Sirignano, 1989) to also account for species mass diffusion within an evaporating droplet subjected to internal circulation (i.e., convective effects) with the so-called ‘Effective Diffusivity Model’ (Sirignano, 2010). Their findings on the temporal evolution of droplet temperature aligned notably with experimental data for ethanol - acetone mixtures, proving the accuracy of the proposed model.

As it has been briefly reviewed, many phenomena have to be considered in the framework of droplet evaporation modeling, such as species transport, heat and mass convection and diffusion, etc. In order to accurately model such phenomena, it is required to properly estimate the target fluid properties both in the liquid and gas phases. In many cases, the complexity and limitation of these property-estimation models can be associated with different magnitudes of error, when they are used to predict the fuel properties at real spray conditions. This encompasses various aspects, such as the methods utilized to estimate averaged gas phase properties around a droplet, a comprehensive analysis of which was initially conducted by Hubbard et al. (1975) and further explored in the work of Shashank et al. (2011). On the other hand, the accuracy of predictions highly hinges upon a precise understanding of the physical properties of the fuel constituent. This aspect was also partially investigated in the study conducted by Shashank et al. (2011), where the significant influence of the reference values chosen for certain physical properties was underscored. Many models consider constant properties for the film layer around the droplet, which necessitates to establish a reference temperature for evaluating these properties. Among the various film-averaging approaches, the 1/3 rule (Sparrow & Gregg, 1958) stands out as one of the most prevalent and widely adopted methodologies in the literature.

Consequently, emulating the evaporation characteristics of droplets can present significant uncertainties caused by uncertainties in the estimation of properties, which are translated into the final predicted results (e.g., droplet evaporation rate or total evaporation time). Therefore, it becomes imperative to understand how uncertainties in the input parameters can influence the model's output. Evaluating this uncertainty propagation is vital not only to assess the model's robustness but also to identify which parameters are most vulnerable to changes. To the author’s knowledge, the body of literature focusing on uncertainty analysis pertaining to droplet evaporation remains notably limited, with only few studies exploring the propagation of these uncertainties in parameters such as droplet size and velocities at spray combustion (e.g., see (Errante et al., 2018)), although a comprehensive general perspective is still clearly required.

1.5 Surrogate formulation

As discussed before, the complex nature of most practical liquid fuels (e.g., gasoline or diesel, consisting of a large number of hydrocarbon molecules) makes impractical or even infeasible their simulation by means of modelling tools (Kim & Violi, 2018). Hence, reducing the number of fuel components is essential for an effective modeling. Some studies have simplified real fuels like diesel by treating them as single-component fuels to reduce computational costs (e.g., (Yao et al., 2017)). However, this simplification does not account for the intrinsic evaporation characteristics of real multicomponent liquid fuels, where lighter compounds evaporate in a preferential manner (Kim & Violi, 2018).

To address this issue, researchers have explored the use of representative mixtures (also known as surrogates), which aim to mimic certain behaviors of the target fuel with a small number of well-characterized compounds (Mueller et al., 2012). These surrogate mixtures, composed of a few pure compounds, substantially simplify modeling efforts and provide well-defined mixtures suitable for experimental studies (Mueller et al., 2012). Surrogate design can target various thermo-physical properties and behaviors, such as bulk density, dynamic viscosity, distillation curve (Szymkowicz & Benajes, 2018), or evaporation characteristics (Muelas et al., 2019; Su & Chen, 2015), which are referred to as "physical surrogates". Alternatively, surrogates can also be developed to match gas-phase combustion characteristics like flame burning velocity, soot propensity, and ignition delay, known as "chemical surrogates" (Chen et al., 2016; Mao et al., 2021).

The evaporation characteristics of surrogates play a crucial role in replicating spray combustion features such as engine cold start, where fuel droplets have to completely vaporize before reaching the combustion chamber (Sarathy et al., 2018). The vaporization process influences combustion quality by affecting droplet break-up, collision, and dispersion (Abdelghaffar et al., 2010) and, hence, strongly determines fuel-air mixing patterns in the flame. Various methods have been employed to design evaporation surrogates for specific target fuels. For example, Elwardany et al. (2016) studied different mixtures to emulate the physical characteristics of gasoline and used a multi-objective optimization approach to determine optimal blend compositions. Su and Chen (2015) proposed a six-component blend for gasoline, validated against experimental data, to predict droplet evaporation. Chen et al. (2016) employed an inversed batch distillation methodology to develop a four-component mixture to emulate the ignition delay and evaporation of Jet fuel using a unified surrogate approach. Adopting the same approach, Poulton et al. (2020) developed a surrogate for kerosene based on a Discrete Component Model, validated against experimental results for different gas temperatures in the range 673-1073 K. Pinheiro et al. (2021) designed surrogates to match the heating and evaporation behaviors of a Jet A sample. Kim et al. (2014) also developed surrogates for Jet fuel, targeting spray characteristics and gas-phase kinetics. Luo and Liu (2021) used the batch distillation approach to formulate surrogates for Chinese aviation fuel RP-3. The design palette was composed of 24 components, which could acceptably be validated against the distillation data functional group in gas and liquid phases. Muelas et al. (2019) proposed different surrogates for a commercial heating oil through binary mixtures of icosane and 1-methylnaphtlene, which are supposed to replicate the evaporation characteristics, physicochemical properties, and sooting behavior.

Through the previous research studies, the surrogate mixture is often predetermined in terms of the type and number of components, being sometimes the gas chromatography data used to define the type of constituent (Kryukov et al., 2004). Furthermore, a common approach is to select components from different hydrocarbon families to incorporate diverse characteristics into the blend (Chen et al., 2016; Kim & Violi, 2021). For instance, aromatics are usually chosen to mimic soot characteristics of the target fuel, while light-end paraffins (like n-heptane and iso-octane) shape ignition delay properties. Pitz et al. (2007) conducted a thorough examination of the formulation of surrogate mixtures designed to replicate key combustion characteristics of gasoline. They identified potential constituent species and put forth suggestions regarding the initial compositions that could be integrated into near-term gasoline surrogates. Along a similar research line, Farrell et al. (2007) proposed a comprehensive approach consisting of four primary stages for creating surrogates that mimic the intricate chemical properties of diesel. These stages encompass 1) the selection of components, 2) the collection of essential property data, 3) the development of models, and 4) the reduction of complex mechanisms. Based on this literature review, it is found that most surrogate design methods rely on expert choice for the selection of the constituent compounds, with a lack of a predefined, systematic methodology that would allow an unsupervised selection of the surrogate palette.

1.6 Nanofuels

The incorporation of nanoparticles into liquids to augment heat transfer properties constitutes a new domain within the realm of thermal-fluid sciences, catching scholarly attention. This emergent category of fluid, termed as nanofluid, is typically characterized by the dispersion of nanoparticles within fluids, ranging from 1 to 100 nanometers in size, and its inception traces back to the 1980s. Noteworthy among the pioneering endeavors in this field is the work conducted by Choi and Eastman (1995), who introduced the concept of nanofluids. Their early contribution posited the feasibility of engineering a novel classification of fluids by suspending metallic nanoparticles within traditional heat transfer fluids, thus conferring augmented thermal conductivity. Multiple theoretical frameworks have been proposed to elucidate the enhanced heat conductivity exhibited by nanofluids. One postulation contends that this phenomenon can be ascribed to nano-convection, arising from the Brownian motion of nanoparticles within the bulk liquid medium (Jang & Choi, 2004; Prasher et al., 2005). An alternative hypothesis posits that the layered structure acts as a bridge for thermal exchange between solid nanoparticles and the surrounding liquid bulk (Yu & Choi, 2004). In the same line, a theoretical model was developed by Xuan et al. (2003) on the basis of the theory of Brownian motion and diffusion-limited aggregation to predict the thermal conductivity of nanofluids. The study underscores the significant role of nanoparticles' motion and aggregation in influencing the thermal conductivity of nanofluids.

The nanoparticles vary in size and characteristics, ranging from metals like aluminum, copper, titanium, zinc, cerium, iron, thallium, or silver nanoparticles to carbon-based materials like carbon nanotubes, graphite, graphene oxide, as well as biosynthesized nanoparticles. These nanoparticles exhibit diverse utilization across various sectors, notably in medical applications, agriculture, coating industry, purification processes, environmental conservation, fuel production and chemical reactions, composite manufacturing, among others.

The manipulation of fossil fuels through the addition of nanoparticles, characterized by diameters usually smaller than 50 nanometers and maintained at low concentrations (typically below 1%), may represent a straightforward approach for the enhancement of fuel properties. These nanoparticles have been proposed to exert significant influence on diverse physical attributes of the fuel, such as surface tension, thermal conductivity, evaporation rate, viscosity, and the mitigation of undesirable pollutants. Previous research shows that adding nanoparticles has a subtle impact on surface tension, particularly when nanoparticle concentrations are minimal, exhibiting both an augmentation (in the case of metal nanoparticles) and a reduction (for multi-wall carbon nanotubes) in surface tension (Tanvir & Qiao, 2012). Notably, both metal and carbon-based nanoparticles serve to enhance the thermal conductivity of the fuel suspension, thereby causing improvements in heat transfer (Agarwal et al., 2016; Choi & Eastman, 1995). For instance, the enhancement of ethanol's thermal conductivity and radiation absorption through the incorporation of 5 wt.% aluminum nanoparticles (of 80 nm) results in an impressive 140% increase in the combustion rate (Tanvir & Qiao, 2015). Another noteworthy advantage of nanoparticles is attributed to their substantially high specific surface area, particularly for nanoparticles with dimensions less than 5 nanometers, which improves their reactivity and catalytic characteristics, thereby augmenting combustion efficiency and reducing hydrocarbon emissions (Fayaz et al., 2021; Gad et al., 2021).

Furthermore, nanoparticle additives can contribute in accelerating the droplet evaporation process, specially at high temperature environments, through puffing and micro-explosion mechanisms (Dai et al., 2019; Javed et al., 2013a; Javed et al., 2013b). While the introduction of nanoparticle additives tends to enhance the evaporation rate of droplets at elevated temperatures, it is noteworthy that at lower temperatures, nanoparticles have been observed to inhibit the droplet evaporation process. This phenomenon is speculated to be associated with the formation of a solid shell during the evaporation process. In this context, research conducted by Javed et al. (2013a; 2014) has indicated that, under low to moderate temperature conditions ($T < 400$ °C), nanoparticles tend to aggregate and create a dense shell surrounding the heptane droplet, resulting in a reduction in diffusion and evaporation rates, with a maximum decrease of up to 15% observed in the studied scenario.

Despite the considerable body of research focused on examining the impact of nanoparticle additives on the dynamics of droplet evaporation, there remains a conspicuous gap in the literature pertaining to comprehensive investigations addressing in a global manner the potential effects stemming from diverse factors (variations in nanoparticle types, their concentrations, base fuel, etc.). This gap in research is particularly evident when dealing with conventional fuels vaporizing at high temperatures. Hence, performing a comprehensive study with a broad range of conditions would help to identify the most efficient and effective nanofuel formulations for the real combustion applications. On the other hand, the development of models that capture the complex evaporation behaviors of nanofuel droplets remains a crucial step for these studies, deriving the key parameters that govern the evaporation behavior of these novel fuels. Hence, addressing these research needs would contribute to step toward uncovering the potential of nanofuel technology.

1.7 Objectives and outline

This thesis dissertation is divided into seven chapters, each one addressing different aspects related to the characterization of isolated droplets' evaporation and combustion processes. In the following, the contents covered by each chapter are summarized.

Chapter 1 reviews the current state of research in the field, outlining the topics explored in the subsequent chapters, both from modeling and experimental aspects.

Chapter 2 introduces a novel experimental facility developed during this thesis to study isolated droplet evaporation and combustion processes. Namely, the suspended droplet facility (SDF) can maintain flexible operation conditions close to real applications, both in terms of gas temperature, velocity, and composition. Besides a complete description of this SDF, another isolated droplet facility, known as a droplet combustion facility (DCF), is also portrayed in this chapter. In this case, this facility was previously developed according to the free-falling droplet concept. The use of both facilities allows to characterize the droplet evaporation and combustion behaviors in an exceptionally broad range of operation conditions.

Chapter 3 details the developed droplet evaporation model, focusing on the estimation of isolated droplet evaporation characteristics. In order to accurately predict the droplet evaporation behaviors at the aforementioned two experimental facilities, the sub-models required to include additional phenomena, such as conduction of heat through the suspension fiber and the absorption of thermal radiation by the liquid, are also developed and presented. The validation of the resulting modeling tool with experimental data (obtained at both SDF and DCF) also serves to understand the droplet evaporation characteristics at elevated temperature environments.

In Chapter 4, a local sensitivity analysis is employed in order to estimate the impact of uncertainties in different physicochemical properties on model predictions of the main droplet evaporation characteristics (e.g., evaporation rate or total evaporation time). The final objective here is to estimate the level of uncertainty in the predictions as well as to identify the main sources of error. The collected knowledge in this chapter is later used to establish the foundation to identify the target properties assigned in Chapter 6.

Chapter 5 integrates the modeling tool, as well as experimental results obtained at SDF/DCF and literature data published by other scholars to assess the influence of experimental artifacts on droplet evaporation measurement and their deviation from the canonical case. Even if some previous works provide valuable analyses and hints in this regard, they are focused on particular conditions and are difficult to generalize to other situations. This chapter aims to quantify and parameterize the aforementioned experimental artifacts in a global manner. A dimensionless analysis is proposed in order to determine the relevant parameters and magnitudes of the different experimental artifacts. This analysis, combined with droplet evaporation modeling, is applied to experimental data from different sources, proving its usefulness to capture deviations in evaporation rate due to these artifacts for a wide range of conditions.

Chapter 6 addresses the development of a systematic methodology to formulate physical surrogates for liquid fuels. The proposed novel algorithm presented in this chapter has been conceived as an efficient tool for matching the evaporation behaviors of real fuels (such as diesel, kerosene or heating oil) at elevated temperatures. It introduces a systematic method for reducing the composition of these complex petroleum-based fuels into a limited number of components capable of replicating the vaporization characteristics of the desired fuel. An innovative aspect of this approach is that the selection of these constituent compounds does not rely on an expert point of view, but it rather follows a predefined procedure. This methodology makes use of the sensitivity analysis presented in Chapter 4, being successfully validated against experimental results obtained at the droplet combustion facility (DCF) for different complex target fuels.

In Chapter 7, the research delves into an exploratory examination of the impact of incorporating cerium oxide, alumina and carbon nanotubes as additives into diesel fuel droplets. This chapter also combines experimentation and modeling efforts, with a focus on emulating the nanofuel droplet evaporation at high temperature conditions by employing surrogate modeling techniques.

The thesis is supplemented with five appendices that provide additional details on some specific aspects of interest.

2. Experimental methodology

In order to experimentally characterize the droplet combustion behaviors and to obtain benchmark data for further studies, two different isolated droplet facilities are utilized in this work, namely: the *droplet combustion facility* (DCF) and the *suspended droplet facility* (SDF). A detailed description of these setups is provided in the following.

2.1 Droplet combustion facility

The DCF was developed according to the free-falling droplet concept (Muelas et al., 2019). This setup makes it possible to extract droplet evaporation/burning characteristics in an environment of known composition and temperatures in the range ∼1300-1700 K (Muelas et al., 2020), which are considered as representative of flame conditions. As shown in Figure 2.1, the DCF features a vertical quartz tube as the combustion chamber. Positioned at its upper end, a flat-flame burner provides the high-temperature environment required for the evaporation/burning of the fuel droplets. This burner has a central orifice for the injection of liquid droplets along the axial centerline. The fuel droplets (with adjustable initial size, ranging from 60 μm to 180 μm) are generated by a piezoelectric capillary tube, driven by a periodic electrical signal. Consequently, a continuous train of monosized droplets (with a diameter contingent on the size of the capillary orifice and the electrical signal) is injected through the orifice. Such a diameter range is chosen as it offers a balance between the precision of experimental observations and relevance to practical scenarios found in combustion spray applications. For instance, as reported by Ballester and Dopazo (1994; 1996), droplets at spray combustion show an average diameter on the order of several tens of micrometers. However, the coarser end of the spray distribution can extend to approximately 100-200 micrometers.

Throughout the experimentation, the droplets maintained a consistent initial droplet diameter, d_0, with variations being negligible. Ensuring this consistency in d_0 is paramount to preserving the accuracy of the experimental outcomes. Consequently, meticulous verifications are conducted for each experimental iteration, with root mean square deviations in d_0 remaining always below 0.5 μm. The droplet generation is adjusted to a frequency of 25 Hz, ensuring that there is sufficient spacing between successive droplets and preventing any potential droplet-droplet interaction. Taking into consideration the typical velocities of both the droplets and the gas, it is ascertained that the spacing between droplets (over 100 times d_0) is sufficient to preclude any droplet from coming into contact with combustion products from its preceding counterpart.

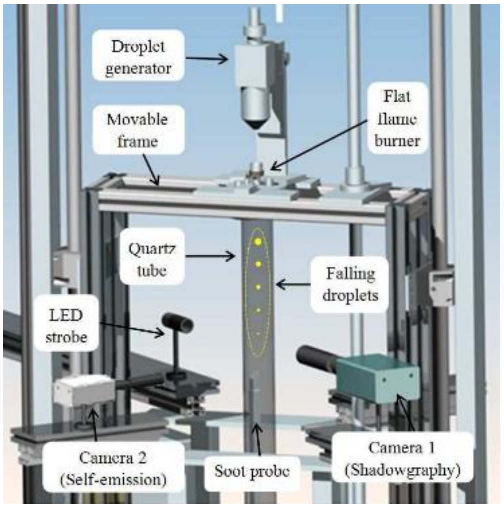

Figure 2.1, Schematic view of the droplet combustion facility (DCF)(Muelas et al., 2019)

The monodisperse droplets fall through the burner orifice and are introduced into the combustion chamber, which is filled by combustion products generated by a premixed, flat-flame McKenna burner. This burner is capable of working with a broad range of methane/air mixtures. The air stream can be doped with N_2 and O_2, providing atmospheres with different temperatures and oxygen concentrations (0% - 10%) in which the droplets evaporate/burn. The coflow gas composition is monitored using a real-time paramagnetic analyzer (Testo 350-S). Since the feed flow consists of methane, air, N_2 and O_2, the flue gas composition predominantly comprised N_2, H_2O, CO_2 and, in some cases, unreacted O_2.

Temperature measurements of the gas coflow were conducted using a 50 µm bare, fine-wire thermocouple (type S), to describe both radial and axial temperature profiles. Figure 2.2 displays the axial profiles for the four most common conditions used in the tests. A comprehensive delineation of these temperature assessments can be found in Addendum A3.1 in (Muelas, 2021).

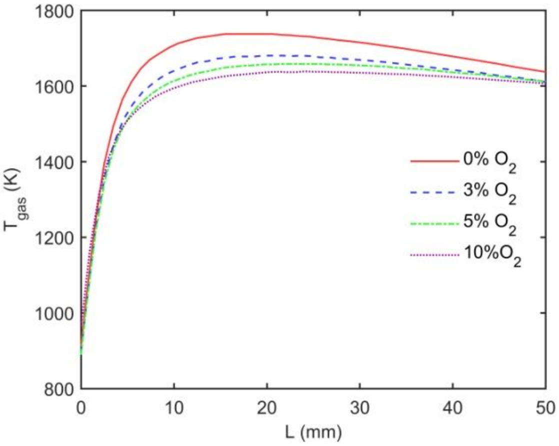

Figure 2.2, Axial temperature profiles measured for the four prevailing gas coflow scenarios, characterized by the combustion of methane in various air and oxygen compositions (combustion products at oxygen concentrations of 0%, 3%, 5% and 10%, (Muelas, 2021)).

The design of this facility allows for independent movement between the camera systems and the combustion chamber, affording observation of the droplets at different heights (i.e., at different residence times). This positioning system is facilitated by a mobile framework that permits the axial repositioning of the combustion chamber. As depicted in Figure 2.1, the experimental rig comprises three cameras. Camera 1 (QImaging Retiga SRV) is used in combination with a long-distance microscope to measure both the size and velocity of the droplets. To facilitate an accurate image capture, a strobe LED light is positioned in front of the camera to enable clear imaging of the shadows cast by the droplets. The synchronization between the optical components and the LED is performed through an Arduino board. The backlight LED strobe produced extremely short light pulses (< 1 µs) at intervals of Δt=500 µs. By optimally adjusting the camera's exposure time, multiple images of a single traversing droplet can be captured within a single frame, as depicted in Figure 2.3.a. For instance, utilizing an exposure duration of 1200 µs enabled the capture of two consecutive images of the same droplet. Since the spatial resolution of the images (in terms of pixel/µm) is known, the distance between the centers of two droplets (Δs) can be measured, estimating in this manner the droplet velocity at a specific location as $v_d = \Delta s/\Delta t$. Besides the droplet velocities, the coflow gas velocities also need to be quantified. This velocity was measured utilizing the Particle Image Velocimetry (PIV) methodology, using a Nd:YAG laser together with Al_2O_3 particle tracers. An introduction to these PIV assessments and the consequent gas velocity profiles is documented in Addendum A3.2 in (Muelas, 2021). The experimental conditions aimed to minimize the relative velocities between the droplet and coflow. Hence, the experiment parameters were adjusted in a way that the Reynolds number (Re), due to the presence of slip velocities between droplet and coflow, consistently remained below 0.5 (typically, <0.2 during the quasi-steady evaporation phase).

A second camera, identified as Camera 2 in Figure 2.1 (Hamamatsu C11440-36U) and equipped with a telemicroscope, is utilized for recording images of the diffusion flame around the fuel droplet (see Figure 2.3.b). This instrumentation facilitates the capture of the spontaneous emission originating from both the envelope flame and the incandescent soot particles surrounding the droplet.

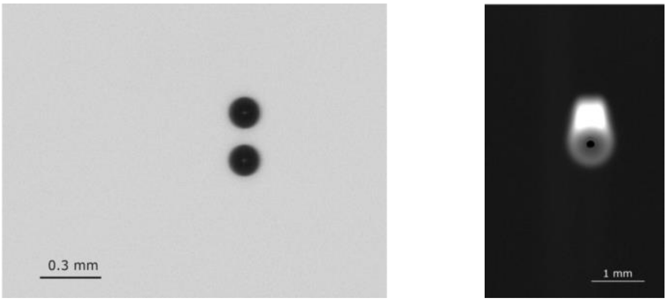

a) b)

Figure 2.3, Two different images acquired at the DCF: a) Double-exposure shadow image of a biodiesel droplet captured by Camera 1; b) Droplet shadow and soot emission recorded by Camera 2 for a heating oil droplet. (Muelas, 2021).

An alternative set of images can be acquired utilizing a third camera (Teledyne DALSA Genie Nano C4060) equipped with a DSLR lens. This color camera is employed to capture the macroscopic flame streaks generated during the descent of the droplets along the combustion chamber. With extended exposure durations, the individual droplets merge into a continuous trace, thereby yielding an integrated luminosity representing the cumulative emission from consecutive droplets. Figure 2.4 is an example of the flame traces resulting from the combustion of various fuels under the 10% O_2 condition.

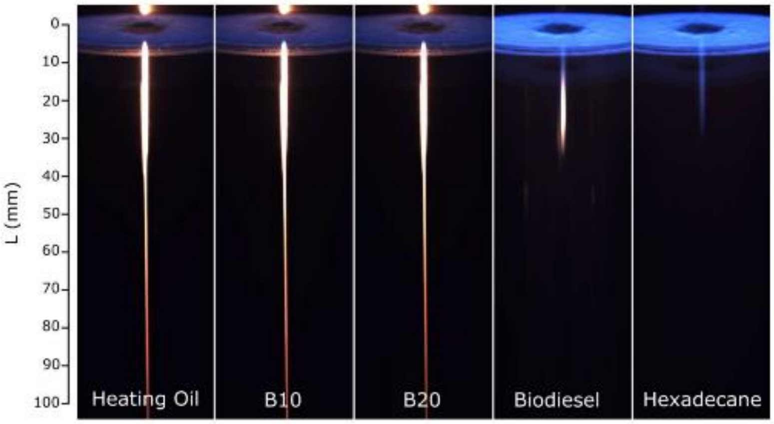

Figure 2.4, Image of flame profiles for a range of fuels: heating oil, biodiesel, two mixtures of these fuels comprising 10% and 20% biodiesel by volume, and hexadecane. The images depicting heating oil and its composite blends were acquired using a 500 ms exposure time. For biodiesel and hexadecane, an exposure time of 2 seconds was required, allowing for the observation of 50 injected droplets (Muelas, 2021).

The radiative heat flux inside the cylindrical combustion chamber was measured with an ellipsoidal radiometer probe, yielding values in the interval 29.4 - 20.6 kW/m^2 at axial distances from the burner surface of 30 and 90 mm, respectively. More information regarding these radiative heat flux measurements can be found in Appendix A.

Despite the capabilities offered by the DCF for studying the isolated droplet evaporation/burning, such as high-temperature environment, low convective effects and small droplet size, the application of this setup remains limited when it comes to explore certain fuel types and characterizing distinct phenomena (e.g., droplet puffing or microexplosions). On the one hand, the droplet generation method does not allow a complete study of very viscous or particle-laden fuels (e.g., heavy fuel oil). On the other hand, capturing very fast and/or stochastic phenomena such as droplet puffing or micro-explosion remains the main limitation of this setup, since these phenomena necessitate capturing the complete history of an individual droplet, which cannot be accomplished at the DCF. The need to address these missing features has motivated the development of the suspended droplet facility (SDF) within the context of this doctoral dissertation. The different aspects of this apparatus will be introduced in the subsequent section.

2.2 Suspended droplet facility

As a counterpart to the DCF, a new isolated droplet facility was entirely designed and developed within the framework of this thesis. This setup relies on the suspended droplet approach, and therefore it offers the possibility of studying fuels with a broad range of viscosity and/or containing solid particles. Furthermore, it allows the monitoring of the evaporation/burning characteristics of a given droplet during its whole lifetime. Figure 2.5 depicts a schematic representation of this setup, which is named as *suspended droplet facility* (SDF). At this apparatus, static fuel droplets undergo evaporation or combustion in a high-temperature gas coflow consisting of a stream of combustion products generated by a McKenna flat flame burner operating with premixed CH_4/Air/O_2. The feed flows for the burner are adjusted from slightly rich conditions for the pure evaporation case (i.e., 0% O_2 in the coflow) to lean conditions which allow for excess oxygen in the flue gas (up to 21% by volume).

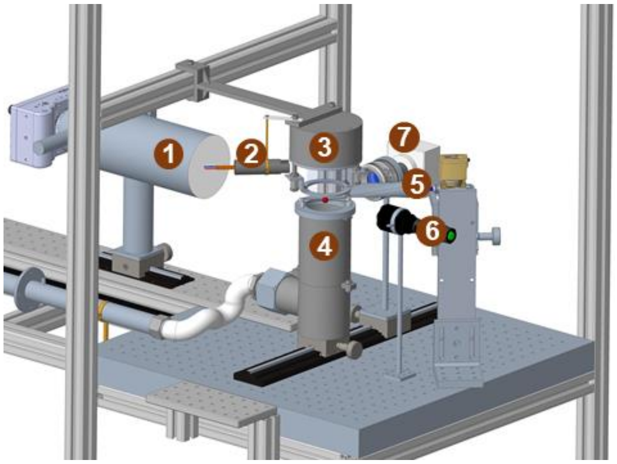

a)

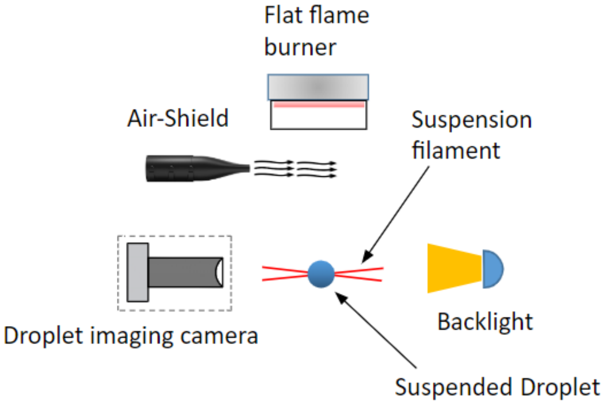

b)

Figure 2.5, Schematic of the suspended droplet facility. a) 3-D view: 1. high-speed camera assembly, 2. flame monitoring device, 3. McKenna burner, 4. droplet holder assembly, 5. Air-shield, 6. Backlight, 7. High-sensitivity camera. b) 2-D, simplified side view.

Gas composition measurements are conducted utilizing a Testo 350 paramagnetic flue gas analyzer, verifying the oxygen concentration in the flue gas. The flow of combustion products is constrained by a quartz tube positioned at the base of the McKenna burner. This tube is vertically oriented, with the flow descending. At its outlet, a flat nozzle releases a horizontal jet of cold air to shield the droplet from the hot gases until the experiment commences.

The fuel droplet is generated by a 0.5 µl micro-liter syringe (Hamilton™) and deployed on a suspension medium. Various materials are utilized to suspend the droplets, including Nicalon™ silicon carbide (with an average diameter of 15 µm), Nextel® 312 Al/Si/B (11 µm), quartz fibers (100 µm), and two different platinum (Pt) wires (25 µm and 50 µm). Different configurations of these fibers are used in this setup. For silicon carbide and Al/Si/B, a cross-fiber arrangement is employed, which comprises either two individual fibers (referred to as 2×1) or two bundles, each containing 3 or 6 fibers (referred to as 2×3 and 2×6, respectively). In the case of Pt25, Pt50, and quartz, a single filament is employed to suspend the fuel droplet, with the Pt wires adopting a U-shaped configuration. The suspension medium is situated on the droplet holder assembly, which is designed to keep the droplet location at a fixed distance (nominally, 65 mm) from the flat flame burner surface.

This droplet holder assembly is mounted on a manual rack-pinion traverse system, enabling precise positioning beneath the quartz tube during experimentation. An extraction system located at the bottom removes the descending hot gas flow. The extraction flow rate is regulated using an orifice meter to maintain flow laminarity and temperature uniformity. The resulting gas velocity at the droplet location is estimated as 0.1 m/s, yielding a Reynolds number of approximately 0.5 for a 500 µm droplet. In accordance with this low Reynolds number, the envelope diffusion flames observed during n-pentanol combustion with 10% O_2 exhibits good sphericity (as seen in Figure 2.6.a), indicating minimal effects from both natural and forced convection in these tests. Figure 2.6.b shows the backlit image of a fuel droplet suspended at a 2×1 SiC arrangement. This image is post-processed in order to extract the droplet diameter evolution and to estimate relevant metrics describing the evaporation characteristics.

In this experimental arrangement, two optical setups are employed to capture the complete temporal evolution of the isolated, suspended droplet while avoiding interferences between them. The primary optical setup comprises a long-distance microscopic lens, the Questar QM1, affixed to a high-speed Chronos 2.1-HD camera, capable of recording up to 24,000 frames per second (fps) at reduced resolution. In most cases, a resolution of 1024×768 pixels was employed at 2500 fps, primarily for droplet imaging. To enhance droplet contour sharpness, strongly backlighted images were used, with an intense LED equipped with a 515 nm long-pass filter that prevents interference with the faint bluish chemiluminescent flames recorded by the second camera. The spatial resolution of this optical setup is 3.43 ± 0.05 µm per pixel. An illustrative image captured by this setup is displayed in Figure 2.6.b.

A second optical setup, perpendicularly placed to the first one, is employed to simultaneously capture images of the diffusion flame surrounding the droplet. This setup utilizes a high-sensitivity monochrome camera (Hamamatsu Orca C11440-36U), coupled with a Nikkor 50 mm f/1.4 lens and a CH^* narrow bandpass filter (430 ± 5 nm) to capture the flame reaction zone. For this optical setup, a resolution of 800×960 pixels and 66 fps were utilized. This configuration allows for the capture of weak chemiluminescent envelope flames with a relatively high signal-to-noise ratio, as demonstrated by the sample image in Figure 2.6.a. The optical setup is calibrated to achieve a spatial resolution of 12.46 ± 0.06 µm per pixel. It is worth noting that both optical setups possess a sufficiently wide field of view to encompass the complete dynamics of droplets with sizes up to 1.2 mm in diameter.

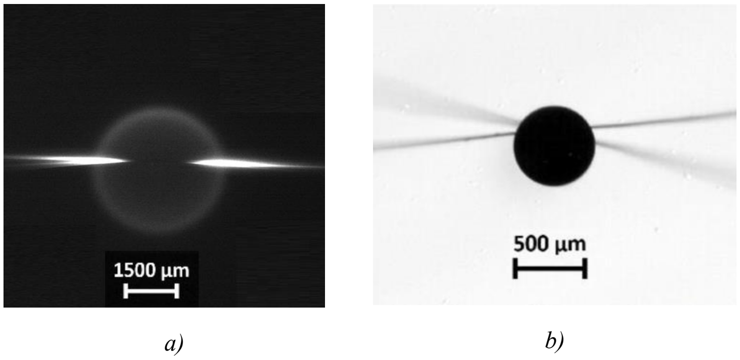

Figure 2.6, Image acquisition at SDF. a) Sample image of the envelope flame at 10% O_2 condition captured for a pentanol droplet by the high-sensitivity Hamamatsu camera; b) Backlit image of a pentanol droplet captured by the high-speed Chronos camera.

Each experimental sequence entails the synchronization of four key events, facilitated by an Arduino Mega 2560 interfaced with MATLAB®. The sequence of events unfolds as follows: firstly, the cold air jet shield is activated to shield the droplet location from the combustion products emanating from the McKenna burner. Secondly, the fibers are prepared, the droplet is generated by micro-syringe and positioned at their intersection, with attention paid to preventing air entrapment within the droplet. Subsequently, the droplet is traversed to its final position while the operating air shield maintains the ambient temperature at approximately 325 ± 1 K. Finally, as soon as the droplet reaches its designated position, a timing event is triggered, initiating the image acquisition by both cameras, followed by the closure of the air shield's solenoid valve 90 ms apart. Figure 2.7 shows the different timing sequences which are synchronized in the experiment.

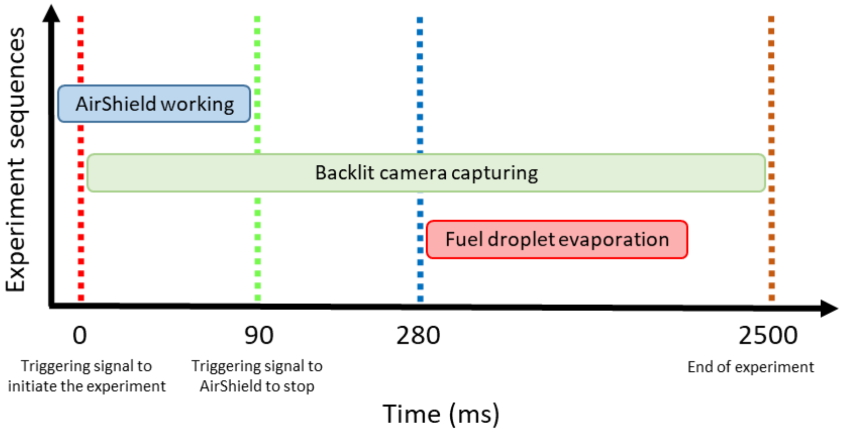

Figure 2.7, Schematic diagram of different timing sequences for a droplet combustion experiment.

Cutting the airshield leads to a rapid increase in temperature at the droplet location (see Figure 2.8), quantified through repeated measurements using a 70 µm S-type thermocouple (see Appendix B). The start of the experiment (i.e., t_0 in all the temporal evolutions presented in this thesis) is defined as the instant when 90% of the temperature increase displayed in Figure 2.8 is reached. That is, 280 ms after the first triggering signal is released. Considering a droplet evaporation time span of 1 s, this droplet would evaporate within an ambient temperature range of 1336 ± 50 K. Additional local measurements conducted within a ±5 mm spatial domain from the droplet location (~$10d_0$) indicate a uniform temperature field within ±10 K. These measurements provide a detailed description of the conditions under which the droplet undergoes evaporation. The radiative heat flux at the SDF is measured with an ellipsoidal radiometer, yielding a value of 23.5 kW/m^2 at the droplet location (see Appendix A for further details regarding these measurements).

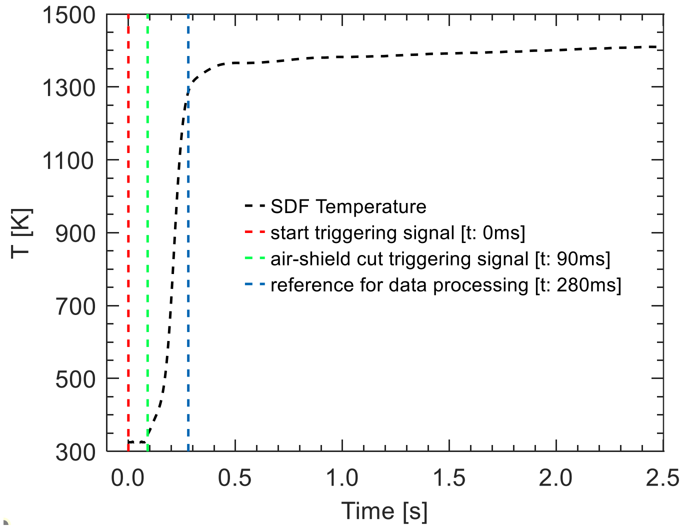

Figure 2.8, Temporal evolution of gas temperature at the droplet location in the SDF

In summary, at the SDF (Suspended Droplet Facility), it is feasible to capture the evaporation and combustion characteristics (with $0 \leq \%O_2 \leq 21$) of reasonably-sized (350 – 1200 μm) isolated droplets at high temperatures (1336 ± 50 K), in a suspended droplet configuration where forced convection and buoyant effects are minimized. Even if they were not finally used in the tests reported in this dissertation, it is worth to note that two additional quartz tubes of different lengths were prepared for this facility, allowing to reach temperatures of ~1000 K and ~700 K at the droplet location, extending the capabilities of the SDF setup for a remarkably wide range of gas temperatures.

2.3 Droplet image processing

The processing of the images acquired with both optical setups assumed paramount importance in facilitating a comprehensive analysis of the droplet evaporation and combustion processes. In this study, image processing for droplet diameter extraction is systematically performed via coding in MATLAB® software. The process begins with choosing a region of interest (ROI) for the raw image, cropping the specific region in which the droplet is present. This allows for a significant speed up of the image-processing algorithm. Hereafter, the conversion of the cropped RGB image (Figure 2.9.a) into grayscale is performed, as illustrated in Figure 2.9.b. Grayscale conversion simplifies the image by representing it in a single channel of colors, enabling subsequent segmentation. Segmentation, a crucial step in image analysis, involves partitioning the image into distinct regions or objects relevant to a specific application. This work employs a region-based segmentation technique known as thresholding, where pixels in the grayscale image are categorized as "foreground" or "background" based on intensity values (Figure 2.9.c).

The Otsu algorithm (Otsu, 1979) with a fixed threshold value is employed for segmenting the droplet image. Furthermore, to reduce noise interference without compromising important image features, morphological operations are introduced. These operations encompass diverse techniques, including erosion and dilation, aimed at enhancing image structure. In this context, image erosion is employed to eliminate unwanted regions corresponding to suspension fibers (Figure 2.9.d). Subsequently, hole-filling operations are applied to address gaps resulting from variations in light intensity across the image (Figure 2.9.e).

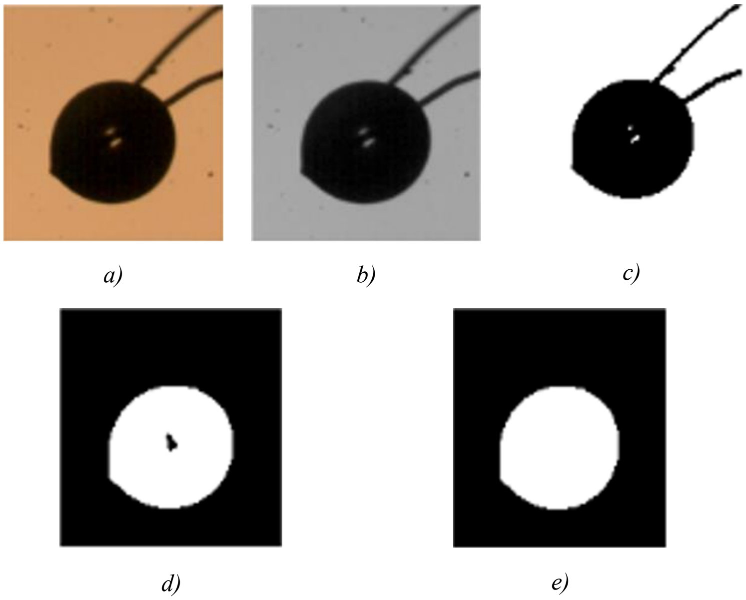

a) b) c)

d) e)

Figure 2.9, Sequence of image processing to isolate the droplet from its surroundings; a) RGB, cropped image; b) grayscale image; c) binarized image; d) eroding image to remove suspending fiber; e) Filling image regions and holes.

The combined application of these image processing techniques contributes to an accurate droplet diameter evaluation. Once the image is transformed as shown in Figure 2.9.e, it is possible to estimate the droplet diameter by counting the number of pixels composing the droplet region and calculating the equivalent circle diameter in pixels. Hereafter, by knowing the spatial resolution of this optical setup (3.43 ± 0.05 µm per pixel), the droplet diameter can be calculated in µm.

This image processing algorithm is used to process all the images captured in an individual test and to extract the droplet diameter at each time instance. This allows for the extraction of the droplet size evolution curve. Following common practice in the field, the data is plotted in terms of the droplet diameter squared (d^2) versus residence time (t), both normalized with the initial droplet diameter squared (d_0^2), as depicted in Figure 2.10. The linearity predicted by the d^2-law (described in Chapter 1.2) is apparent in these experimental results, as expected for a pure fuel such as butanol vaporizing at quite constant gas temperatures. Apart from other metrics, which shall be discussed further on, the quasi-steady droplet evaporation rate ($K = -\,\mathrm{d}(d^2)/\mathrm{d}t$) is intensively used throughout the following chapters. This evaporation rate can be readily obtained from the evaporation curve depicted in Figure 2.10, by calculating the slope of the linear fit on the experimental data in the interval of d^2/d_0^2: 0.6 – 0.2, where the initial transient due to the droplet heat-up can be considered as finished.

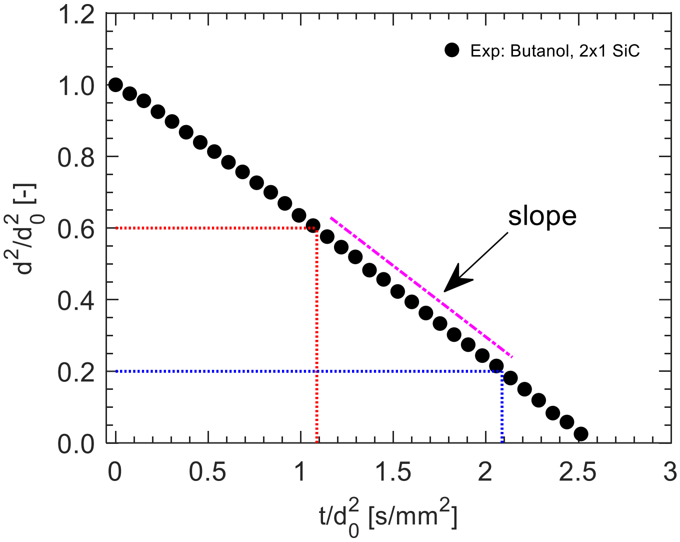

Figure 2.10, Droplet evaporation curve and the quasi-steady evaporation rate.

3. Droplet evaporation model

Understanding the mechanisms governing the transport phenomena occurring during the evaporation and combustion of individual liquid fuel droplets holds significant relevance across various applications characterized by the utilization of spray vaporization and burning. Hence, the development and validation of droplet evaporation models has been motivated significant research efforts (Abramzon & Sirignano, 1989; Sazhin, 2006; Yang & Wong, 2001).

As previously pointed, the second foundational element of this doctoral dissertation is droplet evaporation modeling. While the experimental findings acquired within the context of the SDF/DCF encompass results related to droplet evaporation for a wide range of operation conditions, the computational aspect of this thesis predominantly concentrates on emulating the droplet evaporation characteristics at those conditions. Consequently, the conceptual framework articulated herein corresponds to a model specifically designed for capturing the evaporation dynamics of multicomponent fuel droplets under realistic, high-temperature conditions.

3.1 Model description

3.1.1 Conservation equations for gas and liquid phases

The underpinning scenario presented in this section presupposes an isolated, spherically configured droplet of radius a. This droplet undergoes vaporization while immersed within an infinite and quiescent environment characterized by a far-field temperature denoted as T_g and fuel mass fraction $Y_{fu,\infty}$. In consideration of the absence of both forced convection and buoyancy effects, heat and mass transfer processes can be considered 1-D, as illustrated in Figure 3.1.

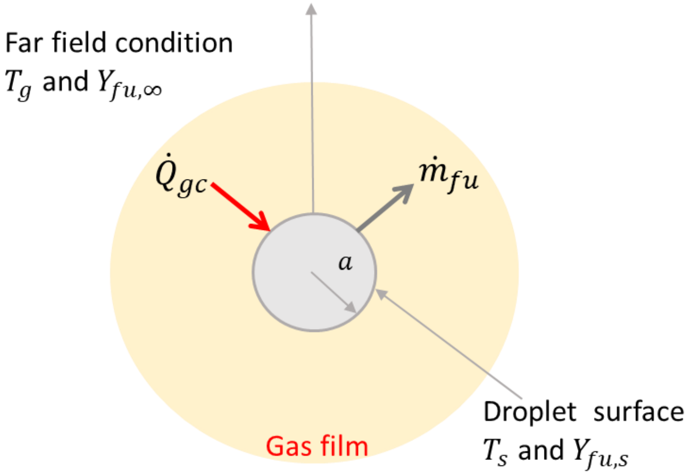

Figure 3.1, Schematic of the canonical 1–D droplet evaporation problem where the only heat input to the droplet is conduction through the gas-liquid interface ($\dot{Q}_{gc}$).

The three fundamental equations governing the gas phase in this problem are: conservation of total mass, conservation of individual species and conservation of energy. These governing equations can be written in spherical coordinates as:

$$\frac{\partial \rho}{\partial t}+\frac{1}{r^2}\frac{\partial}{\partial r}(r^2\rho v)=0 \tag{3.1}$$

$$\rho\frac{\partial Y_{fu}}{\partial t}+\rho v\frac{\partial Y_{fu}}{\partial r}-\frac{1}{r^2}\frac{\partial}{\partial r}\left(r^2\rho D_{fu}\frac{\partial Y_{fu}}{\partial r}\right)=0 \tag{3.2}$$

$$\rho c_p\frac{\partial T}{\partial t}+\rho v c_p\frac{\partial T}{\partial r}-\frac{1}{r^2}\frac{\partial}{\partial r}\left(r^2 k\frac{\partial T}{\partial r}\right)=0 \tag{3.3}$$

In the context of low-pressure applications for which the model is primarily developed, the small value of $\frac{\rho}{\rho_l}$ (approximately 10^{-3}) justifies the quasi-steady assumption in the gas phase analysis. This is attributed to the rapid response time of the gas phase in comparison to the liquid, as elaborated by (Liñán, 1985). Consequently, temporal derivatives present in Equations (3.1) to (3.3) can be assumed to be zero, thereby making the analytical process considerably simpler. Omitting the temporal derivatives in Equation (3.1) implies that the mass flow rate of fuel vapor at any radial location remains constant and equal to the evaporated mass flow rate ($\dot{m}_{fu}$):

$$\dot{m}_{fu}=4\pi r^2\rho v=cte \tag{3.4}$$

The mass flow rate (as highlighted in Figure 3.1), remains the primary unknown variable within the context of this model. Consequently, it is advisable to rearrange Equations (3.2) and (3.3) to express them in terms of $\dot{m}_{fu}$.

$$\frac{\dot{m}_{fu}}{4\pi r^2}\frac{dY_{fu}}{dr}-\frac{1}{r^2}\frac{d}{dr}\left(r^2\rho D_{fu}\frac{\partial Y_{fu}}{\partial r}\right)=0 \tag{3.5}$$

$$\frac{\dot{m}_{fu}}{4\pi r^2}c_p\frac{\partial T}{\partial t}-\frac{1}{r^2}\frac{d}{dr}\left(r^2 k\frac{\partial T}{\partial r}\right)=0 \tag{3.6}$$

Therefore, in the context of gas phase dynamics, the problem can be succinctly delineated as the resolution of these two differential equations, subject to the boundary conditions illustrated in Figure 3.1:

$$T(r=a)=T_s \tag{3.7}$$

$$T(r\to\infty)=T_g \tag{3.8}$$

$$Y_{fu}(r=a)=Y_{fu,s} \tag{3.9}$$

$$Y_{fu}(r\to\infty)=Y_{fu,\infty} \tag{3.10}$$

For the droplet size range investigated in this study, it is plausible to assume a thermodynamic equilibrium between the liquid and gas phases at the interface. This assertion is supported by the observation that deviations from equilibrium become only noticeable for droplets with diameters less than 25 μm (Miller et al., 1998). Consequently, the interrelationship between the surface temperature and the vapor mass fraction of the fuel can be expressed using the Clausius-Clapeyron equation:

$$Y_{fu,s} = \frac{MW_{fu}}{MW} e^{\left(\frac{Lv MW_{fu}}{R_u T_b}\right)\left(1-\frac{T_b}{T_s}\right)} \tag{3.11}$$

In the context of mathematical formulations, Equations (3.5) and (3.6) can be integrated through either numerical or analytical methods. Analytical solutions can be readily obtained under the assumption of spatially constant gas phase properties. However, since temperature and composition vary along the radial coordinate, it is necessary to select suitable reference conditions to calculate gas properties that adequately match experimental observations. Several reference conditions have been suggested to this end. A comprehensive analysis of three distinct reference values for temperature and composition was undertaken by (Hubbard et al., 1975). Notably, they discerned that the '1/3 rule' postulated by (Sparrow & Gregg, 1958) emerged as the most fitted reference state for the assessment of gas properties. According to this approach, gas properties should be calculated at average film conditions given by:

$$T_{ref} = T_s + \frac{1}{3}\left(T_g - T_s\right) \tag{3.12}$$

$$Y_{fu,ref} = Y_{fu,s} + \frac{1}{3}\left(Y_{fu,\infty} - Y_{fu,s}\right) \tag{3.13}$$

By assuming gas-phase properties to be constant, it becomes feasible to analytically integrate Equations (3.5) and (3.6). Given the boundary conditions defined in Equations (3.7)-(3.10), the result of this integration can be expressed as follows:

$$\dot{m}_{fu} = 4\pi a \rho D_{fu} ln\left(1 + \frac{Y_{fu,s} - Y_{fu,\infty}}{1 - Y_{fu,s}}\right) \tag{3.14}$$

$$\dot{m}_{fu} = 4\pi a \frac{k}{c_p} ln\left(1 + \frac{c_p\left(T_g - T_s\right)}{Lv + \dot{Q}_{sb}/\dot{m}_{fu}}\right) \tag{3.15}$$

These analytical formulations allow determining the main unknowns of the problem: the vaporization flow rate ($\dot{m}_{fu}$) and the sensible heat transferred to the liquid phase ($\dot{Q}_{sb} = \dot{Q}_{gc} - \dot{m}_{fu}\, Lv$). The results derived by employing the constant property simplification and referencing the '1/3 rule' were previously assessed against a meticulous numerical integration of Equations (3.5) and (3.6), which took into account the variable properties of the gas phase (Muelas, 2021). The negligible differences observed between the two scenarios underscore the validity of employing the constant property simplification for the gas phase analysis.

To provide a comprehensive solution, it is crucial to also examine the liquid phase. For monocomponent fuels, the primary differential equation characterizing the liquid phase corresponds to the heat diffusion equation:

$$\rho_l c_l \frac{dT_l}{dt} = \frac{1}{r^2}\frac{d}{dr}\left(k_l r^2 \frac{dT_l}{dr}\right) \tag{3.16}$$

With the following boundary conditions:

$$\frac{dT_l}{dt}|_{r=a} = \frac{\dot{Q}_{sb}}{4\pi a^2 k_l} \tag{3.17}$$

$$\frac{dT_l}{dt}|_{r=0} = 0 \tag{3.18}$$

For a multi-component droplet, the constituents present in the liquid phase do not necessarily vaporize in a sequential manner, where the progression is from the most volatile component to the least volatile one. This phenomenon arises due to distinct differences in the rates of mass diffusion/transfer within the liquid droplet, as outlined by (Renksizbulut et al., 1992). The process of vaporization is not only influenced by the individual volatility of each constituent, but it is also intricately tied to factors such as the species diffusion inside the liquid bulk, droplet surface regression rate, and the dynamics of fluid motion inherent within the droplet's domain.

In extending this research to encompass multicomponent fuels, the incorporation of the mass diffusion equation for the liquid phase is required. This integration is necessary to adequately represent the depletion rate of the various constituents present in the liquid droplet. Drawing upon the foundational studies conducted by Sazhin et al. (2010; 2014) and Sirignano (2010), the following equations allow to predict the mass fraction distributions of the liquid species within a spherically symmetric droplet:

$$\frac{dY_{li}}{dt} = D_l\left(\frac{d^2Y_{li}}{dr^2} + \frac{2}{r}\frac{dY_{li}}{dr}\right) \tag{3.19}$$

$$\frac{|\dot{m}_{fu}|}{4\pi\rho_l a^2}(\varepsilon_i - Y_{lis}) = -D_l\frac{dY_{li}}{dr}|_{r=a} \tag{3.20}$$

$$\frac{dY_{li}}{dr}|_{r=0} = 0 \tag{3.21}$$

where, Y_{lis} represents the mass fraction of i^{th} fuel component at the surface (liquid phase), while ε_i is the relative volatility, formulated as $\varepsilon_i = \frac{Y_{vis}}{\sum_i Y_{vis}}$, with Y_{vis} indicating the mass fraction of the fuel component i at the droplet surface (vapor phase). When extending the model to address multicomponent scenarios, the gas phase equations remain unaffected. This is in line with the approach proposed by (Sazhin, 2014; Sazhin et al., 2010) and (Sirignano, 2010), where the multicomponent fuel vapors are postulated to emulate the behavior of a monocomponent gas. An analogy would be considering a blend of N_2, O_2, Ar and CO_2 as air. Such an assumption infers that every component of the fuel vapor diffuses uniformly, maintaining a consistent spatial composition.

The described model yielded accurate results for single component fuels, provided that the temporal time step remained adequately small. Conversely, during the simulation of liquid mixtures, the mass diffusion equation consistently exhibited numerical discrepancies, regardless of the chosen time step. This inconsistency was particularly pronounced in simulations under elevated gas temperature scenarios, similar to those observed at the SDF/DCF experiments. Such anomalies were predominantly attributed to the direct employment of Equations (3.19)-(3.21). These equations are applicable under the presumption of a constant droplet dimension throughout the given time step. It is postulated that the very small values of liquid mass diffusion coefficients resulted in the species migration velocity approximating the droplet surface's receding speed. To tackle this difficulty, a coordinate transformation delineated by Sirignano (Sirignano, 2010) was employed. This transformation effectively converted the partial differential equation with a dynamic boundary into one with a static boundary by employing the following dimensionless variables:

$$\xi = r/a \tag{3.22}$$

$$\tau = \frac{\alpha_l t}{a_0^2} \tag{3.23}$$

$$\hat{a}(\tau) = a/a_0 \tag{3.24}$$

$$\beta = \frac{1}{2}\frac{d(\hat{a}^2)}{d\tau} \tag{3.25}$$

The mass diffusion equation based on these dimensionless variables becomes:

$$\frac{\alpha_l}{D_l}\left(\hat{a}^2\frac{dY_{li}}{d\tau} - \beta\xi\frac{dY_{li}}{d\xi}\right) = \frac{1}{\xi^2}\frac{d}{d\xi}\left(\xi^2\frac{dY_{li}}{d\xi}\right) \tag{3.26}$$

With the following boundary conditions:

$$\frac{dY_{li}}{d\xi}|_{\xi=1} = \frac{\rho}{\rho_l}\frac{D}{D_l}ln\left(1+\frac{Y_{fu,s}-Y_{fu,\infty}}{1-Y_{fu,s}}\right)(Y_{lis}-\varepsilon_i) \tag{3.27}$$

$$\frac{dY_{li}}{d\xi}|_{\xi=0} = 0 \tag{3.28}$$

Resolving the mass diffusion equation by adopting Equations (3.26)-(3.28) instead of (3.19)-(3.21) successfully avoids the previously noted numerical complications. It is noteworthy that such a transformation of the partial differential equation to a fixed boundary problem was not required for the heat equation. This distinction arises from the considerably higher thermal diffusion coefficient relative to that of liquid mass diffusion. Specifically, the liquid Lewis number, represented as $Le_l = \frac{\alpha_l}{D_l}$, for prevalent liquid mixtures typically is of an order of magnitude of 100, as reported in (Rapp, 2022).

Finally, in order to numerically solve the PDEs governing the heat and mass diffusion inside the liquid bulk, the equations must be discretized along the radial direction. The spatial domain inside the droplet is divided into 50 nodal points, where the distance between two consecutive points (*Δr*) varies inversely with the square of the radial coordinate (r^2). This discretization approach is performed to yield a mesh configuration wherein a substantial concentration of nodal points occurs in proximity to the surface of the droplet, where the gradients are more pronounced.

3.1.2 Forced convection effects on isolated droplet evaporation

The model described in the previous section operates under the assumption of a perfectly spherically symmetric evaporation mechanism. This assumption inherently excludes the presence of both natural and forced convection phenomena. Since relative velocities between the fuel droplets and the co-flow gas can introduce discernible deviations in terms of droplet evaporation behaviors from the one-dimensional canonical problem, the model is modified to incorporate forced convection influences. Drawing from (Abramzon & Sirignano, 1989), the gas-phase analysis is updated, resulting in alterations to Equations (3.14) and (3.15) as follows:

$$\dot{m}_{fu} = 2\pi a \rho D_{fu} Sh^* ln\left(1 + \frac{Y_{fu,s} - Y_{fu,\infty}}{1 - Y_{fu,s}}\right) \tag{3.29}$$

$$\dot{m}_{fu} = 2\pi a \frac{k}{c_p} Nu^* ln\left(1 + \frac{c_p\left(T_g - T_s\right)}{Lv + \dot{Q}_{sb}/\dot{m}}\right) \tag{3.30}$$

Here *Sh** and *Nu** represent the modified Sherwood and Nusselt numbers, respectively, defined as the following:

$$Sh^* = 2 + \frac{Sh - 2}{F_m} \tag{3.31}$$

$$Nu^* = 2 + \frac{Nu - 2}{F_t} \tag{3.32}$$

In Equations (3.31) and (3.32), the Sherwood (*Sh*) and Nusselt (*Nu*) numbers are derived based on the correlations proposed by (Clift et al., 2005) relevant to a sphere immersed within a fluid medium. The factors F_m and F_t are extrapolated from the correlations suggested by (Abramzon & Sirignano, 1989) aiming to encapsulate the variations in film thickness resultant from the Stefan flow. It is noteworthy that, when the slip velocity is zero (*Re*=0), the resultant *Sh* and *Nu* values converge to 2, recovering the analytical solutions delineated in Equations (3.14) and (3.15) for the canonical 1-D scenario.

In the context of the liquid phase, the presence of a slip velocity between the droplet and its gaseous surroundings creates an internal convective motion within the liquid. Particularly in scenarios characterized by high Péclet numbers ($Pe_l = \frac{2v_s r}{\alpha_l}$), the internal convective transport within the droplet is faster than thermal diffusion, leading to the formation of vortex structures.

These structures disrupt the 1-D symmetry inherent to the previous liquid phase analysis. A recourse to address this challenge is the adoption of the 'effective conductivity' paradigm proposed by (Abramzon & Sirignano, 1989). This model treats the heat transfer within the droplet as being solely a consequence of thermal conduction, albeit with an effective liquid thermal conductivity ($k_{l,eff}$). This modification compensates for the enhanced transport resulting from internal circulation. Empirical evidence underscores the model's efficacy in accurately forecasting surface temperature and evaporation rates. Nonetheless, it is important to acknowledge its inherent limitation in precisely mapping the temperature distribution within the droplet. Abramzon and Sirignano (1989) showed that convection-induced effects within the liquid phase can be therefore integrated into the model by simply substituting k_l by $k_{l,eff}$ in Equations (3.16) and (3.17):

$$k_{l,eff} = k_l \chi_T \tag{3.33}$$

$$\chi_T = 1.86 + 0.86\, tanh\left(2.245 \times \log_{10}\left(\frac{Pe_l}{30}\right)\right) \tag{3.34}$$

In a related study, Sirignano (2010) validated a methodology that considers the impact of internal convection on the liquid mass diffusion process in an analogous manner. Termed the 'effective diffusivity' model, this approach entails the replacement of D_l with $D_{l,eff}$ in Equations (3.19) and (3.20):

$$D_{l,eff} = D_l \chi_M \tag{3.35}$$

$$\chi_M = 1.86 + 0.86\, tanh\left(2.245 \times \log_{10}\left(\frac{Re_l Sc_l}{30}\right)\right) \tag{3.36}$$

3.1.3 Conduction of heat through the fiber and radiation absorption

As discussed in Chapter 1.3, in many experimental setups the fuel droplet is suspended on fibers, being exposed to high temperatures. Also, in some cases, the droplet is surrounded by hot surfaces that would emit a significant thermal radiation heat flux. Therefore, when simulating the process of droplet vaporization, it is critical to consider the effect of the potential additional heat transfer mechanisms (i.e., absorption of thermal radiation and fiber heat conduction). This section describes the modifications introduced to account for these effects in the model. Namely, the energy equation governing the liquid phase, Equation (3.16), has been modified to include these two additional heat transfer mechanisms, conduction of heat through the fiber ($\dot{q}_{fc}$) and radiation ($\dot{q}_{rd}$), following the approaches proposed in (Abramzon & Sazhin, 2005; Yang & Wong, 2001). Equation (3.37) is the final form of the liquid energy equation, incorporating these two additional heat source terms, which are presumed to be uniformly distributed within the volume of the droplet:

$$\rho_l c_l \frac{\partial T_l}{\partial t} = \frac{1}{r^2}\frac{\partial}{\partial r}\left(k_{l,eff} r^2 \frac{\partial T_l}{\partial r}\right) + \dot{q}_{fc} + \dot{q}_{rd} \tag{3.37}$$

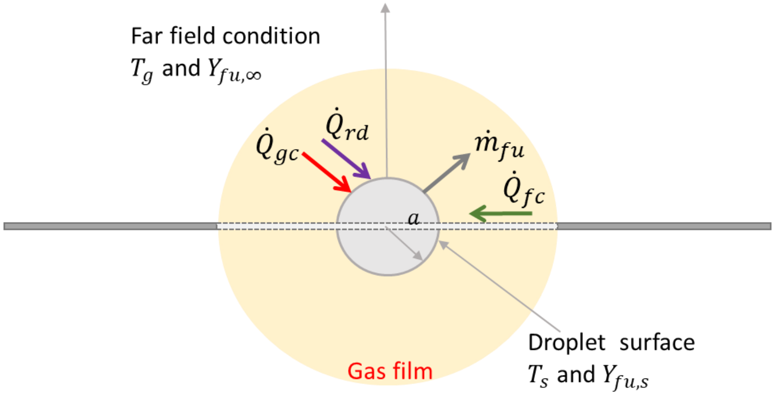

Figure 3.2, Schematic of the droplet evaporation problem with additional heat transfer modes: absorption of thermal radiation ($\dot{Q}_{rd}$) and fiber conduction ($\dot{Q}_{fc}$).

To calculate the conduction input through the fiber ($\dot{q}_{fc}$), a transient model is used to describe this phenomenon. Since the fiber is thin, characterized by Biot number of O(10^{-2}), the temperature distribution in the fiber can be assumed as one dimensional. Hence, the the 1-D heat balance along the fiber can be readily solved through Equation (3.38) (Yang & Wong, 2001):

$$\begin{aligned} x > a \qquad & \rho_f c_f \frac{\partial T_f}{\partial t} = k_f \frac{\partial^2 T_f}{\partial x^2} + \frac{4 h_g}{d_f}\left(T_g - T_f\right) - \frac{4\varepsilon_f}{d_f}\left(\sigma T_f^4 - \frac{\Omega}{4\,\pi}\dot{Q}''_{rd}\right) \\ x < a \qquad & \rho_f c_f \frac{\partial T_f}{\partial t} = k_f \frac{\partial^2 T_f}{\partial x^2} + \frac{4 h_l}{d_f}\left(T_l - T_f\right) \end{aligned} \tag{3.38}$$

h_g and h_l are the heat convection coefficients in the parts of the fiber in contact with gas and liquid, respectively, estimated as $h_g = Nu_g k_g / d_f$ and, $h_l = Nu_l k_l / d_f$. The Nusselt number is calculated with the correlations for cylinders recommended in (Churchill & Bernstein, 1977; Churchill & Chu, 1975), whereas T_f and d_f are the fiber temperature and diameter, respectively.

The fiber is assumed to act as a grey body, with an emissivity ε_f adopted from (Linstrom, 1997), and receiving a radiative heat flux $\dot{Q}''_{rd}$ over a solid angle *Ω*. The rest of physical properties of SiC, Al/Si/B, Pt, and quartz are adopted from (Binkele, 1986; Haynes, 2016; Johnson, 1981; Yang & Wong, 2001).

The temperature distribution along the fiber can be obtained by numerically solving the equation set (3.38) together with the following boundary/initial conditions:

$$T_f(0, x) = T_0 \tag{3.39}$$

$$\frac{\partial T_f}{\partial x}|_{x\to\infty} = 0 \tag{3.40}$$

$$\frac{\partial T_f}{\partial x}|_{x=0} = 0 \tag{3.41}$$

In order to solve the fiber PDE, the spatial domain is discretized using a grid where:

- $x < a$ (fiber immersed in liquid): Δr is inversely proportional to r^2. This mesh strategy was already used to solve the PDEs of liquid heating and species diffusion, so that nodes for liquid and fiber are coincident.
- $x > a$ (fiber immersed in gas): Δr is directly proportional to r^2.

This provides a mesh where most nodal points are concentrated close to the droplet surface, where gradients are larger. Hence, the following fiber discretization is applied in simulations: 50 nodes in the liquid, 50 nodes in the gas. This discretization is found to provide accurate results while keeping a moderate computational cost.

Once the temperature distribution along the fiber is obtained, the heat conducted from the fiber to the droplet is estimated as:

$$\dot{q}_{fc} = \left(\int_{x=-r}^{x=+r} h_l(x)\left(T_l(x) - T_f(x)\right)\pi d_f n_f dx\right)/\forall_{net} \tag{3.42}$$

where n_f is the number of fibers and $\forall_{net}$ is the net volume of the liquid fuel (fiber volume excluded):

$$\forall_d = \frac{4\pi a^3}{3} - n_f\frac{\pi d_f^2}{4}2a \tag{3.43}$$

As for the inclusion of the absorption of thermal radiation to the model (see Figure 3.2), Abramzon and Sazhin (2005) formulated a comprehensive approach to estimate the radiation heat flux absorbed ($\dot{q}_{rd}$) by a fuel droplet in terms of the following equation:

$$\dot{q}_{rd} = \pi {d_d}^2 \frac{\Omega_d}{4\pi}\int_{\lambda_1}^{\lambda_2} E_a B_\lambda(T_g) d\lambda \Big/ \forall_{net} \tag{3.44}$$

where Ω_d, E_a, B_λ, T_g, λ and $\forall_{net}$ are droplet solid angle, radiation absorption efficiency factor, Planck's function, gas temperature, wavelength and net volume of the droplet. The Planck's function and radiation absorption efficiency factor are expressed as:

$$B_\lambda(T_g) = \frac{C_1}{\pi\lambda^5\left[exp\left(\frac{C_2}{\lambda\, T_g}\right) - 1\right]} \tag{3.45}$$

$$E_a = \frac{4n_\lambda}{(n_\lambda + 1)^2}\left[1 - exp(-4\pi\kappa_\lambda d_d/\lambda)\right] \tag{3.46}$$

where C_1=3.742×10^8 Wμm^4/m^2 and C_2=1.439×10^4 μmK. The optical constants n_λ and κ_λ are the refraction and absorption indices, respectively. The fuel-specific optical constants can be obtained using the subtractive Kramers-Krönig analysis on the experimentally measured transmittance curves (Dombrovsky & Sazhin, 2003). The dataset of infrared spectra for different fuels is extracted from (Linstrom, 1997) to obtain n_λ, κ_λ (and hence E_a) as a function of λ. The solid angle, Ω_d, is defined as proportional to the portion of the droplet surface which is exposed to the radiative heat flux emitted from the radiating source. As for the case of SDF and DCF setups, $\Omega_d = 2\pi$, since only the upper half of the droplet (top hemisphere) is exposed to radiation from the McKenna burner.

The Planck's function B_λ in Equation (3.45) can be used to estimate the heat flux as a function of the wavelength and temperature of the radiation source. For the experimental setups used in this thesis, the actual value of the total incident thermal radiation heat flux ($\dot{Q}_{rd}^{''}$) was measured with an ellipsoidal radiometer (Chedaille & Braud, 1972), as detailed in the Appendix A.

In case $\dot{Q}_{rd}^{''}$ is known, Equation (3.44) can be rearranged and simplified for single-component liquids as:

$$\dot{q}_{rd} = \pi {d_d}^2 \frac{\Omega_d}{4\pi} \bar{E}_a \, \dot{Q}_{rd}^{''} / \forall_{net} \tag{3.47}$$

where, $\bar{E}_a$ is the average radiation absorption efficiency through specific wavelength intervals, calculated as:

$$\bar{E}_a = \frac{1}{(\lambda_2 - \lambda_1)} \int_{\lambda_1}^{\lambda_2} E_a d\lambda \tag{3.48}$$

Following the approach detailed in (Zhang et al., 2021), in order to calculate the radiation flux absorbed by a fuel droplet, the optical properties of the fuel were estimated in the infrared spectrum, with wavelengths in the 0.5μm ~ 6.0μm range, covering therefore the near- and mid-infrared, and some parts of far-infrared.

3.1.4 Solution procedure

The previous sections describe a comprehensive model accounting for both gas and liquid phases. This model was implemented using MATLAB®, supplemented by a comprehensive property database. This database facilitated the estimation of various thermo-physical properties for both single-component fuels and their mixtures, with all properties exhibiting temperature and composition dependencies in accordance with the mixture rules detailed in Appendix C. Numerical solutions were sought for the equations previously discussed, operating under the assumption of a constant droplet size within an infinitesimally short integration time step (Δt). The time step in each iteration is calculated according to an adaptive approach, leading to a constant decrease in droplet radius between iterations. Starting from the initial conditions, the fuel's vapor mass fraction at the surface, $Y_{fu,s}$, can be determined as articulated in Equation (3.11). This, in turn, facilitated the derivation of the evaporation mass flow rate, denoted by $\dot{m}_{fu}$, via Equation (3.29). Knowing the $\dot{m}_{fu}$ permitted the extraction of the sensible heat, $\dot{Q}_{sb}$, exchanged by the droplet as elucidated in Equation (3.30). This heat was incorporated as the boundary condition (Equation (3.17)) for the heat diffusion differential equation. That is, Equation (3.16) for cases where the only heat transfer mechanism is $\dot{Q}_{gc}$, and Equation (3.37) for simulations that also included the additional heat inputs due to radiation and fiber conduction. Analogously, the understanding of $\dot{m}_{fu}$ and the distribution of the fuel's mass fraction in both phases enabled the computation of the boundary conditions, as set out in Equations (3.27) and (3.28), for the rearranged mass diffusion equation provided by Equation (3.26). The numerical solving of the various differential equations made use of a 1-D PDE solver in MATLAB®, referencing the methodologies of Skeel and Berzins (1990). The resulting temperature and composition distributions within the liquid droplet over the time step Δt formulated the basis for subsequent iterations, with the droplet mass being adjusted by the product $\dot{m}_{fu}\Delta t$.

3.2 Model validation

This section intends to evaluate the ability of the developed modeling tool to emulate the droplet evaporation process under a wide range of conditions by using different empirical data. This evaluation unfolds in two distinct steps. Firstly, the model's predictive performance is validated against literature data. This validation uses the well-known Nomura experiments (Nomura et al., 1996), as well as the modeling results by Yang and Wong (Yang & Wong, 2001). In a second step, the model is further validated against experimental data obtained in this thesis at the SDF and DCF setups, providing in this way a comprehensive assessment of its capabilities for a broad range of conditions.

3.2.1 Validation of the model against literature data

After defining various aspects of the evaporation model, it becomes essential to assess its efficacy vis-à-vis empirical findings documented in prior scholarly works. This validation process is performed in two steps. Initially, the model's predictive proficiency is evaluated from a general perspective by employing the experimental dataset presented by Nomura (1996). Subsequently, the modeling outcomes elucidated by Yang and Wong (2001) are employed to conduct a comparative analysis, specifically examining the competencies of the fiber conduction and radiation sub-models.

The experiment of Nomura (1996), was performed in a closed chamber at micro-gravity conditions and along with different environmental temperatures. The heating chamber was filled with pure nitrogen to allow a single heptane droplet to evaporate at the tip of a quartz fiber (k_f = 1.37 W/m/K (Yang & Wong, 2001)). Since the experiments were performed in a closed chamber where the elevated temperature was maintained by an electric furnace, the effect of thermal radiation emitted from the hot walls is inevitable (as mentioned by others, e.g., (Ghassemi et al., 2006)). The droplet was suspended at the tip of a rather thick fiber, d_f = 150 µm, which can introduce a significant conduction of heat toward the droplet (Chauveau et al., 2008). Since the presence of these two artifacts has become evident in the experimental data of Nomura (Nomura et al., 1996; Yang & Wong, 2001), they can be used for evaluating the model performance for cases where those experimental artifacts are present. In order to estimate the radiative heat flux absorbed by the droplet, the effective absorption coefficient is set as 0.93, as suggested by (Yang & Wong, 2001). The fiber conduction is also calculated via the 1-D model introduced in section 3.1.3. As shown in Figure 3.3, the evaporation model could efficiently predict the heptane droplet evaporation behaviors at the three different environment temperatures tested by Nomura. The prediction errors for the quasi-steady droplet evaporation rate are calculated as 3.0%, 10.8% and 2.6%, for ambient temperatures of 471 K, 555 K, and 741 K, respectively.

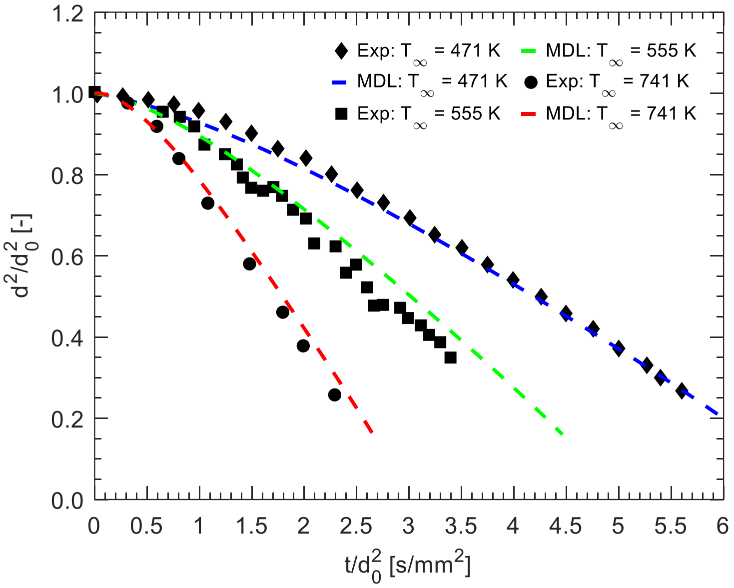

Figure 3.3, Comparison of model predictions with experimental measurements of Nomura (1996) for n-heptane droplet at different temperatures.

Although the modeling tool shows a remarkable ability to match the general behaviors of fuel droplet evaporation at the Nomura experimental conditions, the individual effects of fiber conduction and radiation heat are still unclear. Hence, the modeling tool is employed once again to emulate the individual impact of these two experimental artifacts (radiation and fiber conduction) on the droplet evaporation characteristics. In order to perform this evaluation, the modeling results of Yang and Wong (2001) are employed, since they performed an exhaustive modeling study based on the droplet evaporation behaviors from the Nomura experiments. Three distinct cases were considered: case 1 neglects both radiation and fiber conduction effects, case 2 considers only radiation absorption, and case 3 incorporates both fiber conduction and radiation effects. (i.e., replicating the complete Nomura experiment). Those three modeling cases were duly validated in (Yang & Wong, 2001), and are also employed here to assess the individual performance of the sub-models embedded in the current evaporation tool. The results of this validation are presented in Figures 3.4 and 3.5.

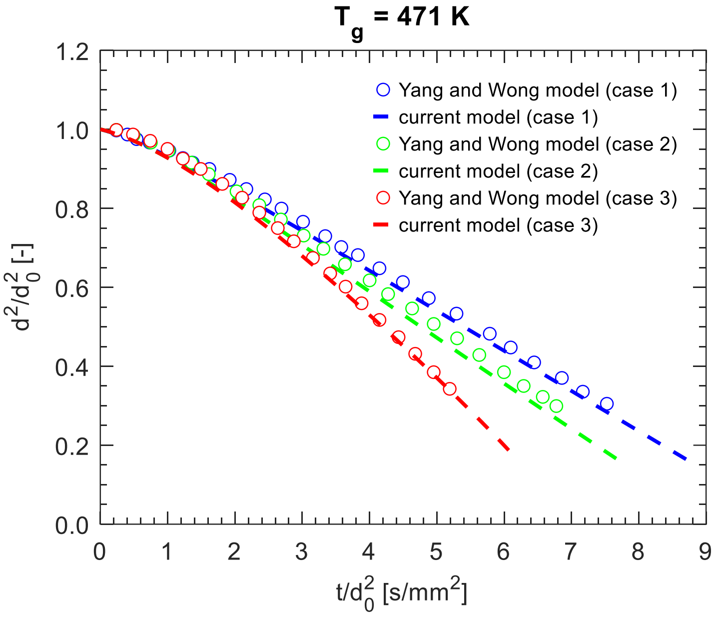

Figure 3.4, Validation of the current model by comparison with the modeling results of Yang and Wong (2001) for T_g =471K. Case 1: ignoring both fiber conduction and radiative absorption (i.e., canonical scenario); Case 2: including radiative absorption; Case 3: including both fiber conduction and radiative absorption (i.e., full experiment by Nomura et al. (1996)).

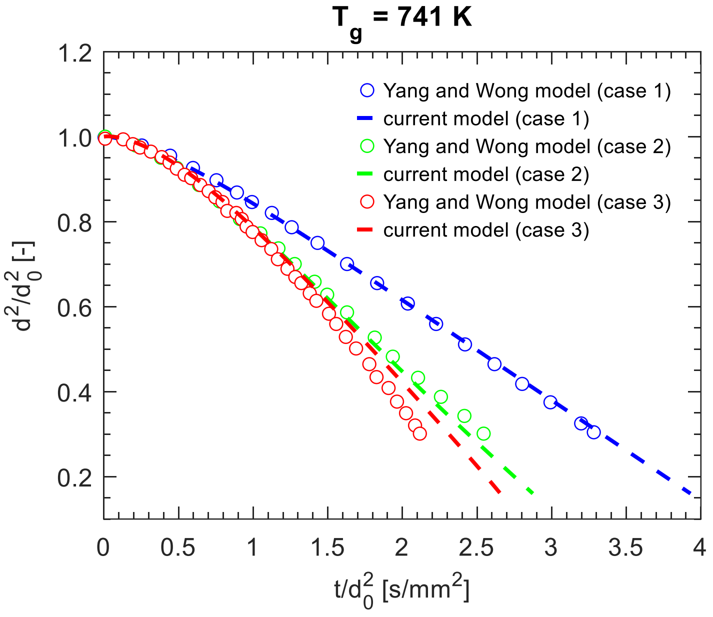

Figure 3.5, Validation of the current model by comparison with the modeling results of Yang and Wong (2001) for T_g =741K. Case 1: ignoring both fiber conduction and radiative absorption (i.e., canonical scenario); Case 2: including radiative absorption; Case 3: including both fiber conduction and radiative absorption (i.e., full experiment by Nomura et al. (1996)).

The current model is able to reproduce quite accurately the behaviors shown by the Yang and Wong simulations. Namely, at the low-temperature condition (471 K), the effect of the fiber outweighs that of radiative heating. However, at 741 K the radiation effect becomes significantly more relevant than that of fiber conduction. The good match obtained for all the cases explored here is thought to prove the reliability of the current model in predicting the evaporation behaviors of isolated, suspended droplets under moderately high temperature conditions, as well as to evaluate the deviations from canonical conditions due to fiber conduction and radiation absorption.

3.2.2 Validation of the model against DCF and SDF experiments

This section intends to validate the developed evaporation model by comparing it with experimental results obtained at the two facilities described in Chapter 2, specifically the Suspended Droplet Facility (SDF) and the Droplet Combustion Facility (DCF). It is worth to note that the environmental temperatures in these two facilities, ranging from 1400 K to 1700 K, cover a range relevant for spray flames and significantly exceed the temperatures documented in most of the existing literature (typically below 1000 K). Moreover, these two facilities present a wide array of experimental conditions, including suspension fiber arrangements (DCF: no fibers, SDF: various fiber configurations), environmental temperatures (DCF: $T_g \sim 1700$ K, SDF: $T_g \sim 1400$ K), and droplet sizes (DCF: $d_0 \sim 150$ µm, SDF: $d_0 \sim 300$ - 1200 µm). This diversity in experimental conditions offers a unique opportunity for a comprehensive validation of computational models, ensuring their reliability and applicability across a broad spectrum of conditions representative of those occurring in real flames.

In the case of validating the model against the experimental database obtained at the DCF, three different alcohols (butanol, ethanol, and glycerol) are chosen, with the unsupported fuel droplets evaporating in a high temperature and oxygen-free environment. Comparing the temporal evolution of the droplet size predicted by the model with the experimental data (as shown in Figure 3.6), a remarkable agreement for the vaporization of alcohols is found, with relative prediction errors for the quasi-steady evaporation rate below 5% in all cases. These results are discussed in detail in (Muelas et al., 2020).

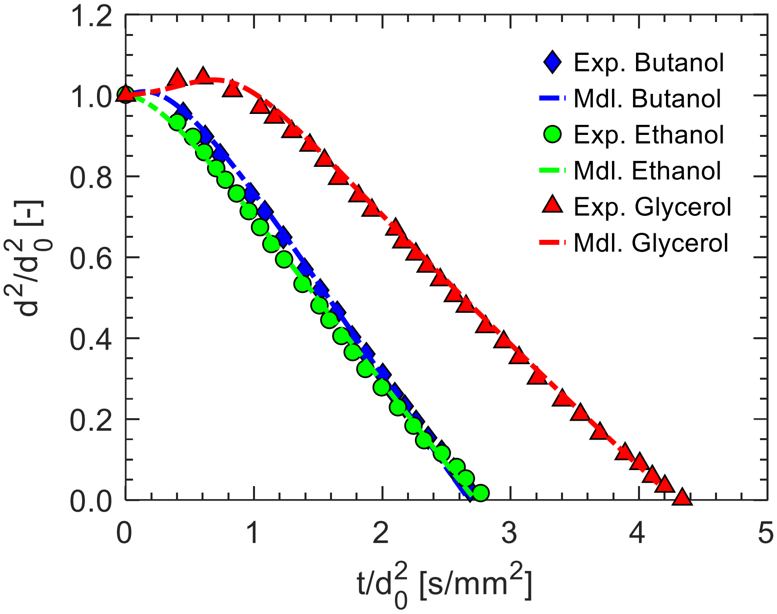

Figure 3.6, Comparison among the modeling results and experimental measurements obtained at DCF for different alcohols (ethanol, butanol, and glycerol).

Besides validating the model against the DCF conditions (i.e., small, unsupported droplets vaporizing at quite high temperatures), it is important to subject the droplet evaporation model to a rigorous examination within experimental settings where the droplet evaporation process can be more influenced by additional heat transfer modes such as fiber conduction and radiative heating. Hence, a detailed comparison among the experimental droplet evaporation data obtained at the SDF for two alcohols (butanol and glycerol) and their corresponding modeling results is presented in the following.

As outlined in Chapter 2.2, the experimental measurements conducted at the SDF involved the utilization of various fiber configurations, encompassing variations in fiber size, material and number. Among the observed results, certain instances were characterized by the evaporation of suspended droplets accompanied by puffing or bubbling phenomena (i.e., internal boiling). For instance, evaporation of butanol droplets suspended on platinum wires of 25 and 50 µm (Pt25 and Pt50, respectively). This behavior is attributed to the strong conduction of heat through these thick and highly conductive filaments. As a result, the fiber temperature increased above the liquid boiling temperature, creating hotspots where vapor nucleation occurred. Given that the existing evaporation model does not account for the formation of vapor bubbles within the droplet, the validation set is chosen among the experimental results where the fuel droplets undergo smooth evaporation without displaying any puffing or bubbling behaviors. Consequently, for the examination of butanol droplets, the 2×1 SiC, 2×3 SiC, and 2×6 SiC fiber configurations are selected, while for the analysis of glycerol droplets, the 2×1 SiC and Pt25 wire fiber arrangements have been chosen as benchmark for model evaluation. The initial droplet sizes considered for each of these fiber arrangements closely approximates 450 µm. The considerable diversity in fiber configurations and the presence of two distinct fuel types with notably different boiling points ($T_b^{glycerol}$ = 563 K, $T_b^{butanol}$ = 390 K) allow for a comprehensive assessment of the previously introduced sub-models.

As depicted in Figure 3.7, the model demonstrates a remarkable performance for accurately predicting the evaporation characteristics of butanol droplets for all the fiber configurations tested. It can be noticed that employing a high number of fibers for the suspension of the droplet yields a significant enhancement in the droplet's evaporation rate. Moreover, as the number of suspending fibers increases from a 2×1 to a 2×6 arrangement, a subtle nonlinear behavior manifests towards the end of the droplet evaporation process (where the receding droplet dimensions eventually become comparable to those of the suspension fibers), significantly accelerating the droplet vaporization. In this sequence, the droplet's evaporation curve deviates notably from the anticipated linear trend dictated by the d^2-law. Considering the modeling performance, the evaporation model could predict the butanol quasi-steady evaporation rate (K) with relative errors of 2.5%, 3.8%, and 8.5% for 2×1 SiC, 2×3 SiC and 2×6 SiC fiber arrangements, respectively.

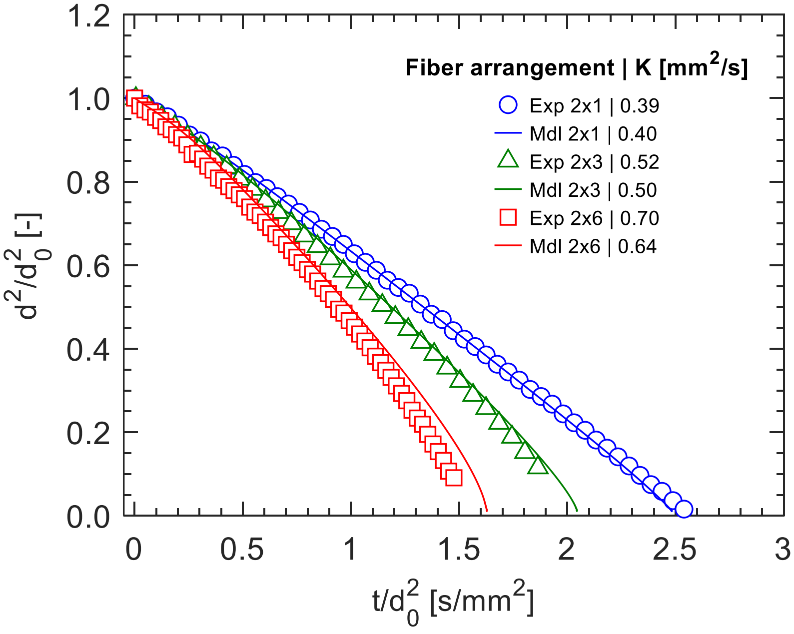

Figure 3.7, Comparison among the modeling results and experimental measurements at SDF for butanol droplets suspended at different fiber arrangements.

Figure 3.8 shows the experimental data and modeling results for the case of glycerol droplets suspended at 2×1 SiC and Pt25 arrangements. The model predictions demonstrate good agreement with the experimental measurements. Similarly to the case of butanol, fiber conduction significantly influences the droplet evaporation characteristics, with a much faster evaporation for the Pt25 arrangement. Again, this is ascribed to the use of a relatively thick wire in combination with the high thermal conductivity of Platinum. Furthermore, the evaporation curve for glycerol suspended at Pt25 shows a clear non-linear behavior at the very end of the evaporation sequence, where the droplet evaporation does not follow the d^2-law anymore. Based on these results, it is discerned that the evaporation model adequately emulates the glycerol droplet's quasi-steady evaporation rate with a margin of error amounting to 3.8% and 12.8% for the configurations characterized by 2×1 SiC and Pt25, respectively.

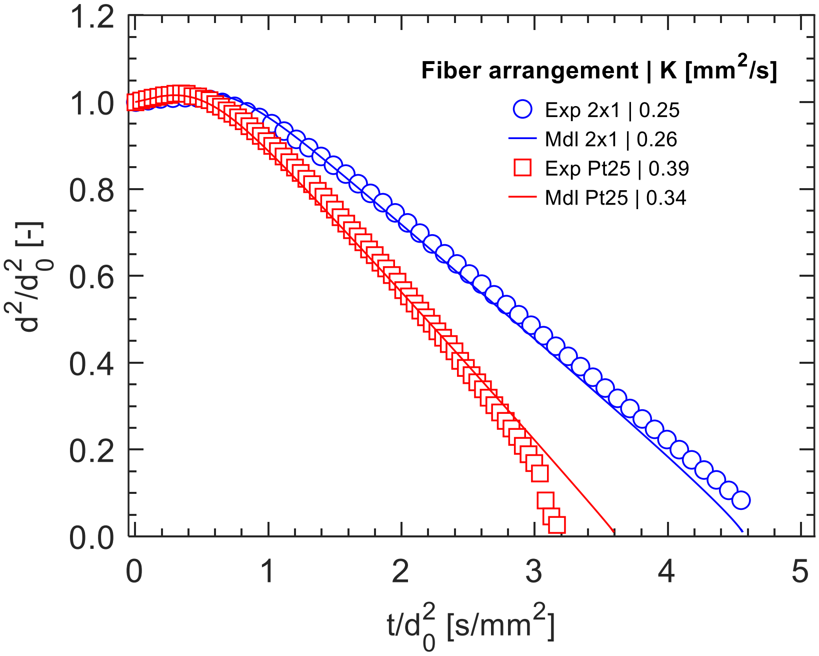

Figure 3.8, Comparison among the modeling results and experimental measurements at SDF for glycerol droplets suspended at different fiber arrangements.

In summary, the modeling tool demonstrated a remarkable accuracy in emulating the intrinsic characteristics associated with the evaporation of isolated droplets in a broad range of operating conditions obtained both from the literature and at SDF/DCF conditions. This outcome underscores the thoroughness of the model's validation process, lending credibility to its predictive capabilities. Hence, this model can be used for further assessment of different evaporation behaviors of isolated droplets, which will be explored in the following chapters.

4. Influence of the fuel properties on droplet evaporation behaviors

4.1. Motivation

As it was previously mentioned, the accurate prediction of droplet evaporation constitutes a key step in the analysis of spray flames due to its determinant role in essential aspects like droplet penetration and dispersion or the spatial and temporal distribution of the released fuel vapor. Evaporation models are relatively simple (e.g., the evaporation model developed in this study), compared to other phenomena like turbulence or chemistry and have been developed and refined since the 1950s. However, the accurate modeling of heat and mass transfer processes during the evaporation of practical fuels remains a challenge, requiring further research (Fiorina et al., 2016; Noh et al., 2018). Several aspects affect the accuracy of the predictions of evaporation rates and, in general, of droplet evolution. On the one hand, the approaches and assumptions related to the various physical phenomena involved were thoroughly reviewed by (Sazhin, 2006). On the other hand, the reliability of predictions heavily relies on an accurate knowledge of the physical properties of the substances involved. This also was in part addressed in (Shashank et al., 2011), where, besides the film averaging (e.g., 1/3 law), the strong impact of the reference values selected for some physical properties was clearly demonstrated. The ability of evaporation models to correctly describe the highly multi-component nature of practical fuels (diesel, kerosene) is frequently pointed out as the main difficulty. However, and although rarely noted in the literature, the uncertainties in the fuel's physical properties can also constitute an important error source in the prediction of the droplet evaporation/burning characteristics at spray condition. Even if there are many physicochemical properties involved in shaping the evaporation characteristics of an isolated fuel droplet, not all of them have the same influence; therefore, it is crucial to identify the most influential set of properties for emulating the droplet evaporation behavior. This information is also beneficial for the formulation of surrogates, as it will be detailed in Chapter 6. In summary, the objective of this Chapter is to find answers to questions like '*How are property-related uncertainties translated to errors in the droplet evaporation predictions?*' or '*Which are the properties with the highest impact?*' which seem most relevant issues but they have not been duly addressed in the literature.

4.2. Case study and methodology

This section intends to consider the situation normally found when conducting numerical simulations of spray flames with real fuels like diesel or kerosene. Depending on the case, some fuel properties can be known, but (apart from exceptional cases) the detailed chemical composition and, especially, the whole set of properties for the liquid and vapor phases are not available. In fact, the properties required for the simulation are usually extracted from different sources, which may include some *ad hoc* fuel analysis, values taken from the literature for similar fuels or assimilating the real fuel to pure compounds, for which many properties can be known. Given that the analysis pursued here does not admit general solutions, the evaporation of diesel droplets was selected as a representative case study. From a literature survey, it was concluded that the most common approach in the numerical modeling of diesel evaporation and/or combustion consists in adopting the properties of pure hydrocarbons, which differ among authors, including heptane (Curran et al., 2001), decane (Raza et al., 2018), dodecane (Kryukov et al., 2004) and tetradecane (Bertoli & Na Migliaccio, 1999). Their main properties are listed in Table 4.1 for the pure fuels (vapor and liquid) and for the gas-vapor mixture in the film around the droplet (following the 1/3 rule) and were determined following the methods described in (Poling et al., 2001): polynomial equations for vapor and liquid properties, Fuller's method for mass diffusivity and Wilke's rule for thermal conductivity and viscosity of gas-vapor mixtures in the film (for further details, the reader is referred to Appendix C). For temperature-dependent properties, an average value is calculated over intervals covering the range of variation during evaporation: between 300 K and the boiling temperature for the liquid and 600-900 K for gases and fuel vapors mixture.

Table 4.1, Selected properties for alkanes normally used to represent diesel fuels. The standard deviation, $\sigma_{\mathcal{X}j}$, and associated uncertainty range, $U_{\mathcal{X}_j}$, are also given.

$\mathcal{X}_j$	Heptane C_7H_{16}	Decane $C_{10}H_{22}$	Dodecane[1] $C_{12}H_{26}$	Tetradecane $C_{14}H_{30}$	$\sigma_{\mathcal{X}_j}$	$\frac{U_{\mathcal{X}_j}}{\mathcal{X}_{j,n}} = \left(\frac{2\sigma_{\mathcal{X}_j}}{\mathcal{X}_{j,n}}\right)$
T_b	371	447	489	523	65.51	0.26
k_l	0.113	0.122	0.126	0.129	0.007	0.14
Cp_l	2395	2508	2573	2593	89.21	0.02
Lv	341.7	319.6	311.3	308.5	15.04	0.01
ρ_l	647.8	666.9	673.1	676.1	12.70	0.11
D_{film}	3.7e-05	3.0e-05	2.7e-05	2.5e-05	5.2e-06	0.28
k_{film}	0.063	0.060	0.058	0.056	0.002	0.07
Cp_v	3272	3238	3225	3218	23.97	0.01
ρ_{film}	0.767	0.849	0.888	0.921	0.066	0.17

(1) Nominal case, from which $\mathcal{X}_{j,n}$ are taken.

This range of four compounds illustrates the significant amplitude of the intervals in which the properties assumed in the calculations can vary among different works; as a reference, the standard deviation, $\sigma_{\mathcal{X}j}$, calculated from the four values is given. The purpose of this section is to evaluate, for this case study, the consequences of the uncertainty range on evaporation predictions as well as to determine the most critical properties in this respect.

The sensitivity of selected parameters extracted from calculated evaporation curves, $\mathcal{Y}_i$, with respect to each of the properties, $\mathcal{X}_j$, can be analyzed in the vicinity of a nominal point, represented by nominal values $\mathcal{Y}_{i,n}$ and $\mathcal{X}_{j,n}$ (data for dodecane).This can be easily accomplished through the error propagation formula, normally used to determine the impact of small variations in the independent input data on the output variables (Saltelli et al., 2008):

$$U_{\mathcal{Y}_i} = \sqrt{\sum_{j=1}^{n}\left(\frac{\partial(\mathcal{Y}_i)}{\partial(\mathcal{X}_j)}U_{X_j}\right)^2} = \sqrt{\sum_{j=1}^{n}\left(J_{ij}U_{X_j}\right)^2} \tag{4.1}$$

U represents the uncertainty interval for a given variable and J_{ij} is the Jacobian, expressing the sensitivity of the outputs with respect to input variables. The results are better expressed in relative terms by normalizing $\mathcal{Y}_i$ and $\mathcal{X}_j$ with respect to their nominal values:

$$\left(\frac{U_{\mathcal{Y}_i}}{U_{\mathcal{Y}_{i,n}}}\right) = \sqrt{\sum_{j=1}^{n}\left(\frac{\partial(\mathcal{Y}_i/\mathcal{Y}_{i,n})}{\partial(\mathcal{X}_j/\mathcal{X}_{j,n})}\frac{U_{x_j}}{\mathcal{X}_{j,n}}\right)^2} = \sqrt{\sum_{j=1}^{n}\left(S_{ij}\frac{U_{x_j}}{\mathcal{X}_{j,n}}\right)^2} \tag{4.2}$$

The relative sensitivity matrix, S_{ij}, is the non-dimensional form of the Jacobian. The output variables, $\mathcal{Y}_i$, are intended to represent different aspects of the evaporative behavior of the droplets. In particular, the three metrics represented in Figure 4.1 have been selected. Following common practice, this curve depicts the evolution of the droplet diameter squared as a function of time, both normalized by the initial droplet diameter squared, d_0^2. The three metrics selected to parametrize this curve are:

- $t'_t = t_t / d_0^2$, where t_t is the total evaporation time.
- Quasi-steady state evaporation rate, *K*, calculated as the slope of the curve between $(d/d_0)^2$ =0.6 and 0.2. It should be noted that 1/*K* is the hypothetical (normalized) time required to completely evaporate a droplet under ideal quasi-steady state conditions.
- $t'_{us} = t'_t - 1/K$ expresses the duration of the unsteady part of the evaporation curve, related to the gradual heating of the liquid until quasi-steady conditions

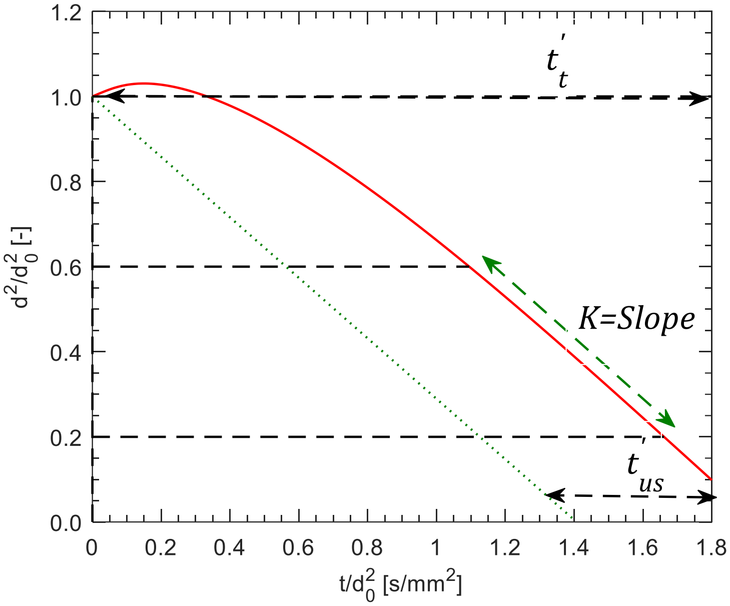

Figure 4.1, Calculated evaporation curve and associated metrics (nominal case: 150 µm dodecane droplet vaporizing at 1400°C). $t'_{t,n}=1.878$ *s/mm²,* $t'_{us,n}= 0.468$ *s/mm²,* $K_n=0.709$ *mm²/s.*

Input variables $\mathcal{X}_j$ are the properties listed in Table 4.1 and their associated uncertainties will be estimated as twice the standard deviation, as usual for estimating uncertainty at 95% confidence. These normalized uncertainties are given in the last column of Table 4.1. Nevertheless, it is important to note that the validity of this procedure is not restricted at all to the values assumed for $U_{\mathcal{X}_j}$, which strongly depend on the particular problem. Equation (4.2) offers a very effective yet simple method to split the two ingredients in the propagation of uncertainties: the sensitivity with respect to each input and the magnitude of the input uncertainties, as quantified respectively by S_{ij} and $U_{\mathcal{X}_j}$. Therefore, the results reported can be easily extrapolated to any other $U_{\mathcal{X}_j}$ scenario.

The nominal case, for which $\mathcal{Y}_{i,n}$ and $\mathcal{X}_{j,n}$ were calculated, corresponds to the evaporation of dodecane droplets in a quiescent ambient consisting of combustion products of a stoichiometric methane-air flame at 1 bar and 1400°C. Dodecane was selected as the nominal case because it is the option most commonly adopted in the literature to represent the properties of diesel fuel. The evaporation metrics, $\mathcal{Y}_{i,n}$, and the normalized sensitivity matrix, S_{ij}, were calculated by means of the droplet evaporation model described in Chapter 3.1. In the modeling process, the effects of fiber heat conduction and radiation heat absorption are neglected, and the convective forces are considered to be absent (i.e., canonical, 1-D droplet evaporation scenario).

The results for this nominal case (dodecane) and its associated metrics, designated as $\mathcal{Y}_{i,n}$ in Equation (4.2), are given in Figure 4.1. The partial derivatives in the Jacobian, S_{ij}, were estimated from finite differences calculated for variations around the nominal point, between $0.95\mathcal{X}_{j,n}$ and $1.05\mathcal{X}_{j,n}$. This interval is narrow enough to provide a reliable estimate of S_{ij} and, at the same time, sufficiently broad to obtain meaningful variations in the calculated metrics, $\mathcal{Y}_i$. Hence, linearity is assumed because the objective is not to evaluate large variations but to estimate uncertainties in the vicinity of the nominal point. The analysis was conducted for two droplet sizes, 20 and 150 µm, so as to fully cover the relevant range for spray flames. The results were practically identical in relative terms (sensitivities, relative uncertainties) for both droplet diameters and, for brevity, only the data for d_0=150 µm will be presented.

4.3. Results: sensitivity analysis

As discussed before, not all the physicochemical properties contribute equally to the high-temperature droplet evaporation behavior. Therefore, a first task within this study is to ascertain the impact of each property on the droplet evaporation curve (and related metrics) presented in Figure 4.1. Figure 4.2 shows an example of the calculations performed to determine the components of the aforementioned Jacobian. In particular, the evaporation curves obtained for the nominal value of the specific heat (Cp_v= 3225 J/kg/K) and the cases in which it is varied by ±20% (increased interval in order to better visualize the changes), with all the rest of the properties maintained at its nominal values, $\mathcal{X}_{j,0}$, as indicated in Table 4.1 for dodecane. A clear change is observed in the droplet evaporation curves, with a significantly slower evolution when the value of the Cp_v is increased, modifying therefore the three evaporation metrics presented in Figure 4.1.

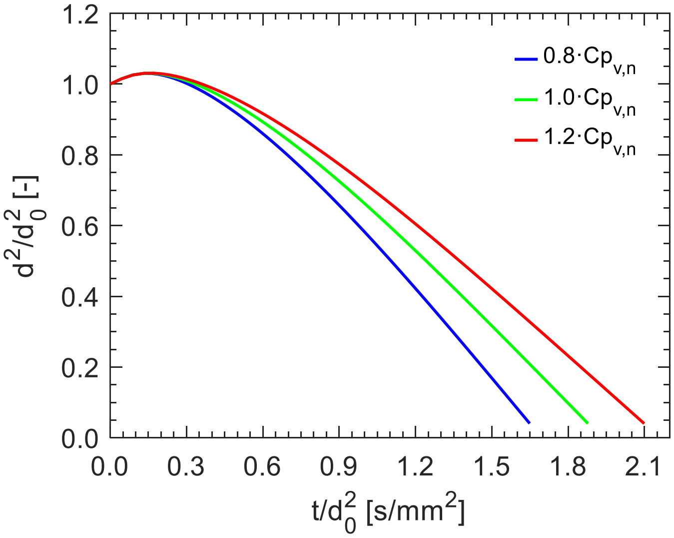

Figure 4.2, Evaporation curves for the nominal case and for ±20% variations in Cp_v around the nominal value.

As discussed before, the partial derivatives in the Jacobian are to be calculated with a ±5% interval around the nominal point. The three selected metrics (t'_t, t'_{us}, K) are extracted applying this interval and the partial derivatives are estimated by dividing the increments in metrics by the corresponding increments in the considered input variable (±5% in Cp_v, in this case). As a result, the relative sensitivities of the three metrics with respect to the specific heat are 0.59, 0.33 and -0.68 for t'_t, t'_{us} and K, respectively, as indicated in the third column of Table 4.2. This means that a 10% increase (or error) in Cp_v would roughly lead to 5.98%, 3.36% and -6.87% variations (or errors) in t'_t, t'_{us} and K, respectively. The same procedure was followed for all input properties, with the results listed in Table 4.2.

Table 4.2, Relative sensitivities, S_{ij}*, of the evaporation metrics,* $\mathcal{Y}_i$*, with respect to the input properties,* $\mathcal{X}_j$

$\mathcal{X}_j \rightarrow$ $\mathcal{Y}_i \downarrow$	$\frac{\partial\left(\frac{\mathcal{Y}_i}{\mathcal{Y}_n}\right)}{\partial\left(\frac{T_b}{T_{b,n}}\right)}$	$\frac{\partial\left(\frac{\mathcal{Y}_i}{\mathcal{Y}_n}\right)}{\partial\left(\frac{\rho_{film}}{\rho_{film,n}}\right)}$	$\frac{\partial\left(\frac{\mathcal{Y}_i}{\mathcal{Y}_n}\right)}{\partial\left(\frac{Cp_v}{Cp_{v,n}}\right)}$	$\frac{\partial\left(\frac{\mathcal{Y}_i}{\mathcal{Y}_n}\right)}{\partial\left(\frac{k_{film}}{k_{film,n}}\right)}$	$\frac{\partial\left(\frac{\mathcal{Y}_i}{\mathcal{Y}_n}\right)}{\partial\left(\frac{D_{film}}{D_{film,n}}\right)}$	$\frac{\partial\left(\frac{\mathcal{Y}_i}{\mathcal{Y}_n}\right)}{\partial\left(\frac{\rho_l}{\rho_{l,n}}\right)}$	$\frac{\partial\left(\frac{\mathcal{Y}_i}{\mathcal{Y}_n}\right)}{\partial\left(\frac{Cp_l}{Cp_{l,n}}\right)}$	$\frac{\partial\left(\frac{\mathcal{Y}_i}{\mathcal{Y}_n}\right)}{\partial\left(\frac{k_l}{k_{l,n}}\right)}$	$\frac{\partial\left(\frac{\mathcal{Y}_i}{\mathcal{Y}_n}\right)}{\partial\left(\frac{Lv}{Lv_n}\right)}$
t'_{us}	3.330	0.181	0.336	-1.002	-0.181	0.927	0.479	0.185	0.003
t'_t	-0.054	0.029	0.598	-1.032	0.029	0.288	0.178	0.001	0.251
K	1.189	0.100	-0.687	1.039	-0.100	-0.077	-0.077	0.061	-0.335

The data shown in Table 4.2 reveal important differences among the expected impacts of various fuel properties. The factors with the greatest influence on the total evaporation time are the thermal properties of the gas (k_{film}, Cp_v), followed by the liquid density, the latent heat and the specific heat of the liquid. These results are consistent with the evaporation process being largely controlled by heat transfer and, hence, becomes faster when the specific heat of both liquid and vaporized fuel and the latent heat decrease or as the thermal conductivity of the gas increases. Also, a higher liquid density reduces the specific surface area, which explains the longer evaporation time obtained. The parameter t'_{us}, expressing the duration of the transient heating, also displays high sensitivity to those parameters, with the strongest sensitivity towards the boiling temperature, the liquid density, and the thermal conductivity of the gas near the droplet. These first and last properties also display the highest influence on K, followed (with opposite trends) by the specific heat of the gas and the latent heat. Other properties, like gas density or mass diffusivity, display very weak influences in all cases. In summary, this sensitivity analysis allows to quantify the impact of each physicochemical property on the droplet evaporation behavior under realistic spray-flame conditions. These results will serve as a valuable base knowledge when it comes to formulate representative blends (i.e., surrogate mixtures) targeting the evaporation behaviors of conventional fuels in Chapter 6.

4.4. Results: uncertainty analysis

The previous section identified the properties with the highest impact on the droplet evaporation behaviors, with Table 4.2 reporting the specific sensitivities due to the various input parameters $\mathcal{X}_j$. However, in order to estimate the error bars for the different metrics, the associated uncertainties, $U_{\mathcal{X}_j}$, must also be taken into account. This is clearly expressed by Equations (4.1)-

(4.2), where the individual contributions are calculated as the product of both terms. As it is detailed above, for this order-of-magnitude analysis, it is assumed that $U_{\mathcal{X}_j} \approx 2\sigma_{\mathcal{X}_j}$, where $\sigma_{\mathcal{X}_j}$ is the standard deviation calculated over the $\mathcal{X}_j$ values for the four alkanes considered (see Table 4.1). The intervals are very different among the various properties: whereas the specific heat is about the same for the four compounds, notable differences are observed for the mass diffusivity or the boiling temperature.

Figure 4.3 shows the individual contributions due to each $\mathcal{X}_j$ as well as the estimated global uncertainty, U_{rms}, for the three metrics. There are significant differences between the estimated impact of some properties in Table 4.2 and Figure 4.3. The case of Cp_v is a good example: whereas the relative sensitivity, as expressed by S_{ij}, was noted to be relatively high, its contribution becomes very small (<1%) when the estimated uncertainty in Cp_v is also considered due to the small differences of this property among alkanes. Much more important are the terms due to the thermal conductivity, the liquid density, and, especially, the boiling temperature.

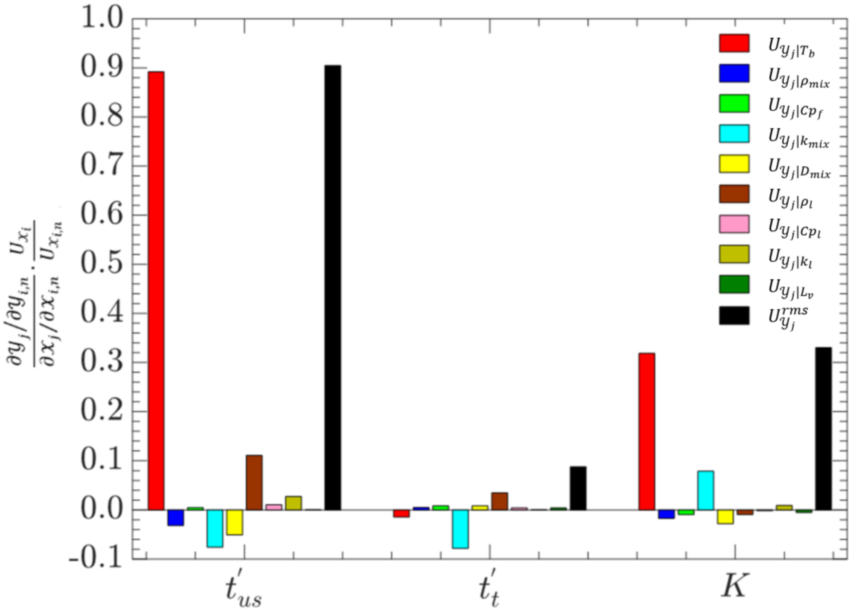

Figure 4.3, Estimated individual contributions and global uncertainties of evaporation metrics due to fuel properties.

The very strong influence of boiling temperature on the duration of the heating period, t'_{us}, clearly stands out. For the uncertainty interval considered, it would result in an uncertainty of 89% in t'_{us}. The effect on K is also significant, with an associated relative uncertainty of 31%, whereas both effects practically compensate to each other and the uncertainty in t'_t is almost negligible. At this point, some comments with regard to the impact of the uncertainty in T_b seem appropriate. First, the value U_{T_b} might appear somewhat overestimated for some situations (especially when dealing with pure compounds); in that case, the uncertainty obtained for the metrics can be easily recalculated and estimated as proportional to the actual error bar in T_b.

Second, even though the uncertainty in total evaporation time is practically negligible, the very high value obtained for $U_{t'_{us}}$ should not be neglected, as ignition and flame stability can be in some cases, largely determined by the initial delay until sufficient amount of fuel vapor is produced. Thus, these results clearly reveal the importance of an accurate description of the distillation curve of multi-component fuels.

The thermal conductivity of the gas, the latent heat and the liquid density also contribute significantly to the uncertainties in the evaporation metrics. Therefore, for the scenario considered, these four properties deserve special attention in order to maintain the accuracy of the predictions within acceptable limits. Overall, the estimated global uncertainties for the metrics considered (black bars in Figure 4.3) are 90% for t'_{us}, 8.7% for t'_t and 33% for K. The actual relevance of these inaccuracies will depend on the particular case and the required reliability of the predictions but, in any case, it is clear that they are at least comparable to other sources of error involved in evaporation calculations. Therefore, the impact of the uncertainties in fuel properties need to be duly considered, either to minimize them (especially those with the biggest influence) or, at least, to be aware of these issues for evaluating the accuracy of the results or even for determining if the effort of implementing highly sophisticated models is worthwhile in cases with a limited knowledge of fuel properties.

Finally, the role of the boiling temperature deserves further analysis. Figure 4.4 displays the evaporation curves predicted for the nominal case ($T_{b,n}$=489 K) along with those for ±20% variations in T_b (391.2 K and 586.8 K). The variation in T_b causes significant changes in the length of the transient heating period and in the quasi-steady evaporation rate, whereas the final time is about the same. This coincides with Tables 4.2 and 4.3, showing that an increase in boiling temperature tends to increment both t'_{us} and K but has a negligible effect on t'_t. Whereas the extension of the transient period seems a logical result, simple heat-transfer reasoning would suggest the opposite effect for K: as T_b increases, the difference between gas and droplet temperatures is reduced and so should be the rate of heat transferred to the droplet, which is the driving mechanism in evaporation.

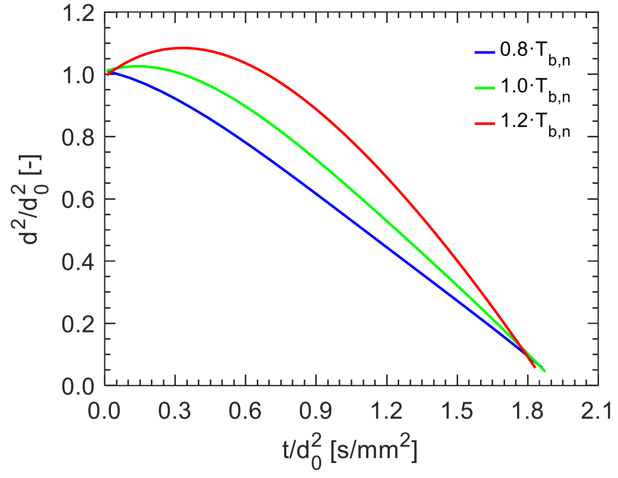

Figure 4.4, Evaporation curves for the nominal condition $T_{b,n}$=489 K, and for 391.2 K and 586.8 K, keeping unaltered all other properties.

The explanation for this apparently contradictory behavior was found in the variation of some physical properties with the temperature, which increases both for the liquid and for the gas near the droplet as T_b becomes higher. Mathematically, it should be noted that Equation (4.1) is only strictly valid for statistically independent inputs $\mathcal{X}_j$, but this is not the case between T_b and several of the properties. If the temperature dependence of some properties is duly considered, the variation in an output variable, $\delta\mathcal{Y}_i$, due to a given increment in boiling temperature, δT_b, can be expressed as:

$$\begin{aligned}\left(\frac{\delta \mathcal{Y}_i}{\mathcal{Y}_{i,n}}\right) = \Bigg[&\frac{\partial(\mathcal{Y}_i/\mathcal{Y}_{i,n})}{\partial(T_b/T_{b,n})} + \frac{\partial(\mathcal{Y}_i/\mathcal{Y}_{i,n})}{\partial\left(Cp_{\mathcal{Y}_i}/Cp_{\mathcal{Y}_{i,n}}\right)}\frac{\partial\left(Cp_{\mathcal{Y}_i}/Cp_{\mathcal{Y}_{i,n}}\right)}{\partial(T_b/T_{b,n})} + \frac{\partial(\mathcal{Y}_i/\mathcal{Y}_{i,n})}{\partial\left(k_{\mathcal{Y}_i}/k_{\mathcal{Y}_{i,n}}\right)}\frac{\partial\left(k_{\mathcal{Y}_i}/k_{\mathcal{Y}_{i,n}}\right)}{\partial(T_b/T_{b,n})}\\ &+ \frac{\partial(\mathcal{Y}_i/\mathcal{Y}_{i,n})}{\partial\left(D_{\mathcal{Y}_i}/D_{\mathcal{Y}_{i,n}}\right)}\frac{\partial\left(D_{\mathcal{Y}_i}/D_{\mathcal{Y}_{i,n}}\right)}{\partial(T_b/T_{b,n})} + \frac{\partial(\mathcal{Y}_i/\mathcal{Y}_{i,n})}{\partial\left(\rho_{l,\mathcal{Y}_i}/\rho_{l,\mathcal{Y}_{i,n}}\right)}\frac{\partial\left(\rho_{l,\mathcal{Y}_i}/\rho_{l,\mathcal{Y}_{i,n}}\right)}{\partial(T_b/T_{b,n})}\\ &+ \frac{\partial(\mathcal{Y}_i/\mathcal{Y}_{i,n})}{\partial\left(L_{v\mathcal{Y}_i}/L_{v\mathcal{Y}_{i,n}}\right)}\frac{\partial\left(L_{v\mathcal{Y}_i}/L_{v\mathcal{Y}_{i,n}}\right)}{\partial(T_b/T_{b,n})}\Bigg]\left(\frac{\delta T_b}{T_{b,n}}\right)\end{aligned} \tag{4.3}$$

The direct effect of T_b on the metrics should be evaluated only from the partial derivative of the first term in the brackets. However, the method applied to obtain the results in Tables 4.2 and Figure 4.3 actually included all the terms, accounting also for indirect effects of T_b due to variations in some properties, as expressed by the rest of the terms in the brackets. In particular, when the gas or liquid temperature increases, the latent heat and liquid density are reduced whereas the thermal conductivity and the specific heat augment; all those variations tend to enhance the evaporation rate and constitute an indirect consequence of increments in boiling temperature, also included in the evaporation simulations used to calculate S_{ij}. Apparently, those side effects overcome the expected reduction in heat transfer, finally resulting in a positive variation in K.

In order to analyze the isolated effect of T_b, the analysis was repeated by eliminating the temperature dependence of the properties, so that all the partial derivatives in Equation (4.3) except the first one are cancelled. The result was a relative sensitivity of K with respect to T_b, $\partial(\mathcal{Y}_i/\mathcal{Y}_{i,n})/\partial(T_b/T_{b,n}) = -0.2$, which is negative and consistent with the physical interpretation based on the smaller temperature difference mentioned above. The same analysis applied to t'_{us} and t'_t yielded relative sensitivities of 3.8 and 0.69 (instead of 3.3 and -0.05, see Table 4.2), respectively. Therefore, the conclusions on the strong impact of T_b on the initial transient heating are also valid (and even slightly increase) if temperature dependences are neglected and, as a result, the total evaporation time would appreciably increase with T_b if constant properties are assumed. Therefore, this analysis confirms the behavior expected from simple heat transfer considerations: smaller K due to a lower difference between liquid and gas temperatures as T_b increases. However, although it might appear somewhat surprising, the real effect is that a higher T_b leads to larger K and about the same total evaporation time due to the temperature dependencies of thermal properties.

In summary, the investigation carried out in this section confirms the potentially high impact of inaccuracies in fuel properties on the reliability of droplet evaporation predictions. The propagation of uncertainties from input data towards evaporation parameters yields multiplication factors of the order of 1 (i.e., relative uncertainties in the outputs similar to those in the inputs) for a number of properties, including specific heat, thermal conductivity or liquid density, and increased up to 3 for the boiling temperature. For the scenario considered (evaporation of diesel droplets at high temperatures), differences up to ~90% in the predictions of some evaporation metrics should be expected depending on the particular assumptions applied, among those normally considered in published works. Therefore, a correct evaluation of the properties for a given fuel appears as a key issue to achieve accurate predictions of droplet evaporation and, hence, of spray flames.

5. Impact of non-ideal conditions on isolated droplet experiments

As detailed in Chapter 2, a new single-droplet facility has been designed and developed over the course of this PhD thesis. This so-called suspended droplet facility (SDF), allows a close control of the conditions and variables involved in experiments on isolated droplet evaporation/burning at high temperature. Independently of the purpose of using such isolated droplet facility, either model validation or phenomenological study, an indispensable condition (for SDF or any other isolated droplet setup) is that the obtained experimental results reproduce the canonical configuration normally sought for isolated droplet studies. As detailed in the Introduction, the results obtained at these facilities can be affected by several experimental artifacts, causing deviations from the ideal 1-D case where the only heat transfer mode is conduction through the gas-liquid interface. Firstly, the conduction of heat through supporting fibers can have significant effects (Chauveau et al., 2019; Yang & Wong, 2002), potentially resulting in overestimated evaporation rates or even causing unexpected phenomena such as puffing or micro-explosions. Secondly, the presence of thermal radiation sources in the proximity of the droplet can cause radiative heating (Fang et al., 2019), also enhancing the evaporation rate. Finally, gas-droplet heat exchange can also be influenced by forced or natural convection, increasing evaporation rates above those obtained in convection-free conditions, while also disturbing the original spherical symmetry of the problem. These experimental artifacts need to be rigorously assessed to ensure the correct interpretation and application of the obtained results, both when it comes to the study of droplet behaviors and for model validations.

Considering the inevitable onset of these undesired effects in most real-world experiments, this section intends to discuss the impact of each artifact on experimental results for isolated droplet evaporation rate and to evaluate the resultant deviations from canonical conditions. The two isolated droplet facilities described in Chapter 2 (DCF and SDF) are employed for this study, providing a broad range of experimental conditions (e.g. fiber arrangements, droplet size, ambient temperature) for two pure compounds with widely different evaporation behaviors, namely butanol and glycerol. Besides the analysis of these experimental data, the modeling tool presented in Chapter 3 is also employed to conduct comprehensive parametric studies. Finally, a dimensionless analysis is proposed to quantify and parameterize these experimental artifacts from a global prospective in which the dependencies with respect to relevant parameters can be simultaneously included (e.g., d_0, d_f, T_g, k_f, etc.). This approach has been thoroughly validated with experimental and modeling results, constituting a novel, valid framework that can help to correctly interpret experimental data and to select conditions that minimize the impact of the aforementioned artifacts.

5.1. Experimental results

As it will be justified further on, the SDF tests are expected to provide a larger impact of experimental artifacts than DCF experiments. In order to build a comprehensive database, 249 tests have been performed at this facility for two liquids fuels with widely different boiling points: butanol and glycerol. Fuel droplets with a broad range of initial size (350-1200 μm) were suspended on different fiber arrangements: cross-fiber configurations 2×1 (2 fibers, SiC and AlSiB), 2×3 (6 fibers, SiC), and 2×6 (12 fibers, SiC), as well as single filaments of quartz and platinum (more details on these fibers can be found in Chapter 2). Figure 5.1 displays the experimental evaporation curves for butanol and glycerol droplets with an initial diameter d_0=500 μm suspended on these arrangements. The slope of this curve in its linear region (d^2/d_0^2 = 0.2 - 0.6) is denoted as the average, quasi-steady evaporation rate (K=-d(d^2)/dt [mm^2/s]), indicated in the legend captions. In theory, if the fibers had no significant effects, all the curves and K values should be about the same. However, Figure 5.1 reveals large differences among curves, clearly demonstrating a great influence of the suspension medium on the evaporation behavior, with noticeably higher evaporation rates and shorter droplet consumption times for thicker fiber arrangements. The curves for platinum wires show some erratic behaviors that will be discussed later on.

The dashed curves in Figure 5.1 are model predictions for unsuspended droplets. As detailed in Chapter 3, the model used for these predictions has been thoroughly validated with data from the DCF (deviations <3% in K for both butanol and glycerol (Muelas et al., 2020)), and, therefore, is expected to provide a good estimate of the size evolution for the canonical case, i.e., without any experimental artifact. The fact that these predictions are closer to the cases with thinner fibers (2×1, both SiC and AlSiB) is fully consistent with heat conduction through the supporting filaments artificially accelerating the evaporation process.

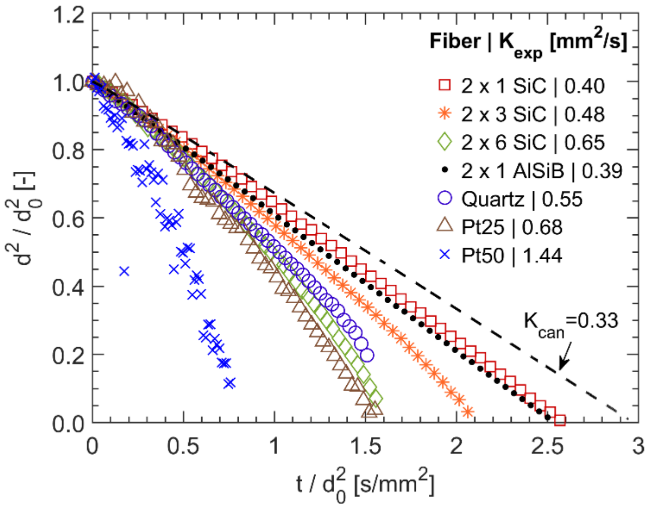

a)

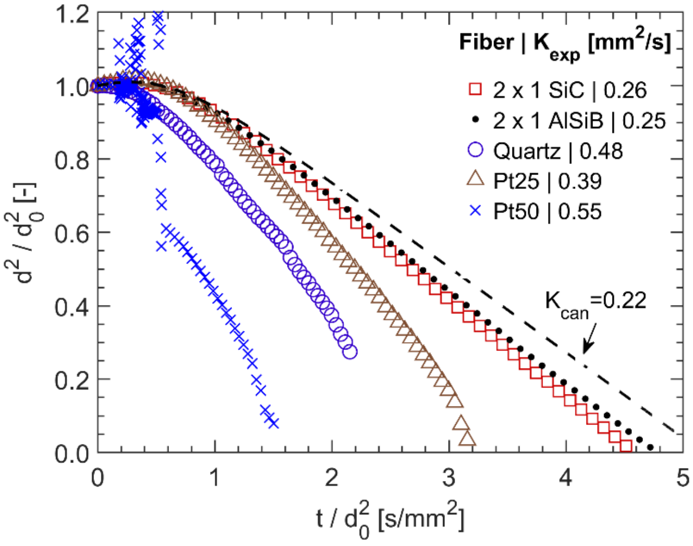

b)

Figure 5.1, SDF experimental evaporation curves for fuel droplets (d_0=500 μm) suspended at different fiber arrangements. a) butanol, b) glycerol. The dashed line represents model predictions for the canonical case.

The evaporation curves of pure compounds like butanol or glycerol should comply with the d^2-law once the initial heating transient has been completed. However, Figure 5.1 clearly proves that this compliance is only fulfilled for the 2×1 fiber configurations (SiC and AlSiB). As the number of fibers increases or thicker/more conductive fibers are employed (Pt, quartz), the evaporation curves lose linearity, with a gradually decreasing slope (particularly for the final part, where droplets are close to depletion). To better ascertain this behavior, the time-derivative of the evaporation curves in Figure 5.1.a and 5.1.b have been calculated, yielding the instantaneous evaporation rates (*K*) plotted in Figure 5.2 and Figure 5.3, respectively.

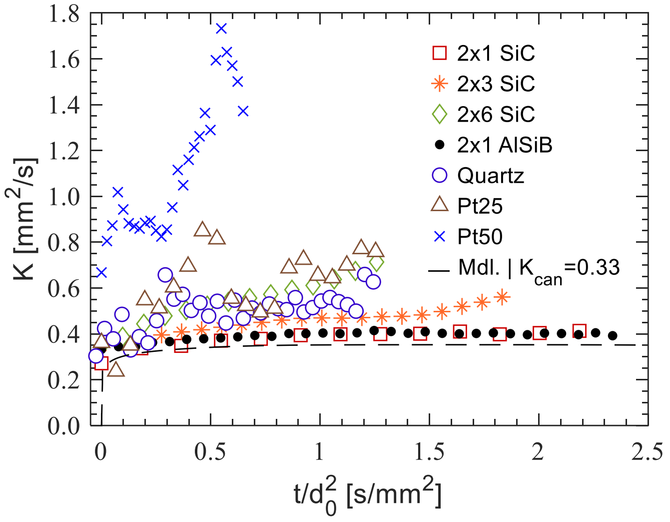

Figure 5.2, SDF experimental instantaneous evaporation rate for butanol droplets (d_0=500 μm) suspended at different fiber arrangements. The dashed line represents model predictions for the canonical case.

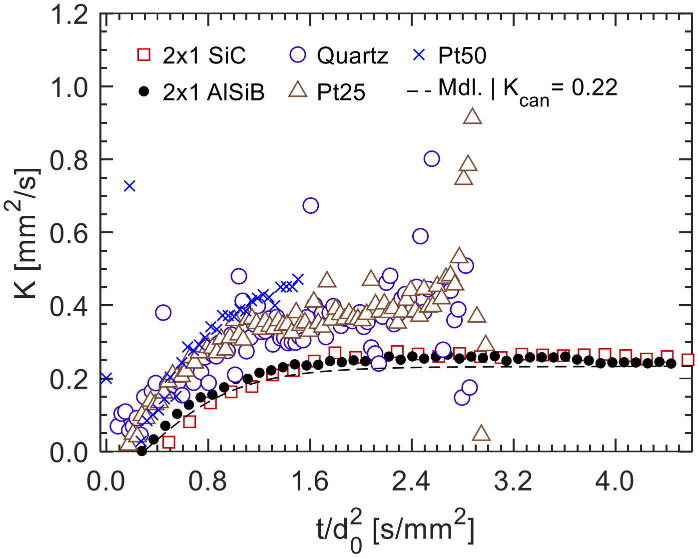

Figure 5.3, SDF experimental instantaneous evaporation rate for glycerol droplets (d_0=500 µm) suspended at different fiber arrangements. The dashed line represents model predictions for the canonical case.

Figure 5.2 confirms that the only cases where the butanol droplet evaporation rate reaches a quite constant value (as predicted by the d^2-law) is when the droplet is anchored by means of 2 single fibers of SiC or AlSiB. The addition of more fibers shifts the evaporation rate to larger values due to the additional heat input conducted through the filaments. This evaporation rate enhancement is found to be quite progressive and occurs throughout all the vaporization sequence. The progressive increase in K with time points to a larger impact of this artifact for small-sized droplets, as it will be elaborated further on. The curves for droplets suspended at quartz and Pt filaments show a completely different behavior, with significantly higher and more irregular instantaneous evaporation rates (Figure 5.2), in agreement with the more fluctuating droplet evaporation curves in Figure 5.1.a. This behavior is caused by the onset of internal bubbling and puffing events, as it will be discussed later. Figure 5.3 shows the instantaneous evaporation rate for glycerol droplets suspended at different fiber arrangements. Same as for the case of butanol droplets, the lowest deviation in evaporation rate from the canonical case are observed for 2×1 SiC and 2×1 AlSiB fiber arrangements. Furthermore, using 50 µm platinum wires (Pt50) significantly enhances the droplet evaporation rate and reduces the droplet life-span, generating also several instances of puffing.

Figure 5.4 displays the quasi-steady evaporation rate (K_{exp}) obtained in 225 different experiments conducted at SDF as a function of the initial droplet size. It is worth to note that only tests with smooth evaporation are included in this plot, removing those where puffing or microexplosions events were recorded (24 instances). As discussed before, these experiments encompass a wide range of conditions, with different droplet sizes (d_0) and fiber arrangements (diameter, conductivity, and number of fibers: d_f, k_f, n_f), using butanol (T_b = 390 K) and glycerol (T_b = 563 K) as fuels. The evaporation rate calculated for the canonical case (unsuspended droplet without radiation or convective effects), K_{can}, is also represented and, in agreement with theory, does not vary with d_0.

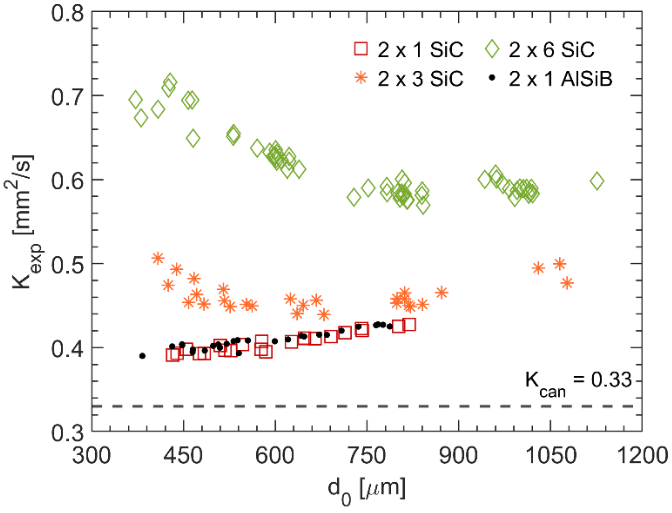

a)

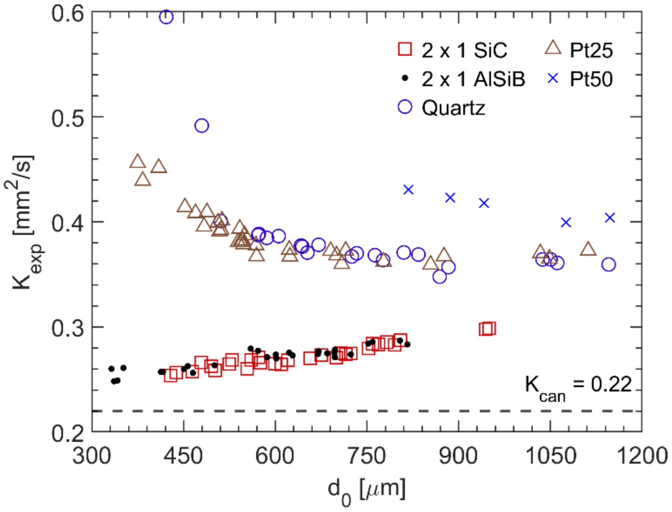

b)

Figure 5.4, Evaporation rate measured for fuel droplets vs. initial droplet size, with different fiber arrangements at SDF experiments. Dashed line: predicted canonical value (K_{can}) by modeling. a) butanol, b) glycerol.

In all cases, $K_{exp} > K_{can}$, with large differences (even exceeding 2×) in some of the tests, which can only be attributed to the artifacts occurring in the SDF experiments. Thus, it is clear that the deviation in the evaporation rate with respect to a canonical situation, $\Delta K = K_{exp} - K_{can}$, strongly depends on test conditions. As already discussed, fiber conduction can significantly enhance the heat input to the droplet (and therefore K_{exp}), being a function of the fiber size and material. This can explain the differences among the various test series, with ΔK increasing with the number, size and conductivity of the fibers. However, other effects are not so obvious, such as the fact that ΔK either increases or decreases with droplet size, d_0, depending on other test conditions. This is ascribed to the combination of different causes: fiber conduction, radiation, and convective effects. Droplets with larger d_0 expose a greater surface area, thereby increasing their capacity to receive radiative heat. In addition, an increase in d_0 also results in higher Grashof and Reynolds numbers ($Gr \propto d_0^3$ and $Re \propto d_0$) for the surrounding hot gas flow, leading to an augmented heat transfer from the hot gas through natural (Verwey & Birouk, 2018) and forced convection mechanisms (Rehman et al., 2016). Both effects would justify an increase in K_{exp} with d_0, but this only occurs when the effect of the fiber is sufficiently small (i.e., 2×1 SiC or AlSiB fibers). Cases with a larger number of fibers and/or thicker and more conductive filaments show the opposite behavior, with K_{exp} decreasing with d_0. This is ascribed to the reduced impact of the fiber for sufficiently large droplet sizes, in agreement with previous works which suggested the relevance of the d_0/d_f ratio (Avedisian & Jackson, 2000; Yang & Wong, 2002). All three potential artifacts must be considered in order to explain the experimental observations for a particular case. This will be attempted in the analysis presented in the next section.

As discussed before, some of the tests with droplets suspended on Pt wires reveal a distinct behavior, both for butanol (d_f =25 and 50 µm) and glycerol (d_f =50 µm), with sudden fluctuations in droplet size (see Figure 5.1) due to the occurrence of internal bubbling and puffing events, occasionally accompanied by weak micro-explosions. Figure 5.5 shows a series of images captured at different time intervals during the evaporation of a butanol droplet suspended on a 50 µm platinum wire. The formation of bubbles within the liquid begins and gradually expands (Figure 5.5.b), causing the surface of the droplet to wrinkle and exhibit puffing behaviors (Figure 5.5.c). At certain moments, the swelling of the droplet becomes more pronounced, leading to the ejection of tiny droplets with significant velocity from the droplet surface (Figure 5.5.d). These puffing events have been previously reported by Wang et al. (2020) and can be considered as a strong distortion of the droplet evaporation process. This behavior is ascribed to a very strong fiber conduction effect, favored by the high thermal conductivity of Pt and the relatively large filament cross-section. As a result, the fiber temperature increases above the liquid boiling temperature, creating hotspots where vapor nucleation can occur (Wang et al., 2020). This phenomenon leads to significant deviations from the quasi-steady linear surface regression characteristic of a single-component fuel droplet and, therefore, the experimental results obtained under such conditions are no longer a valid description of its real evaporation characteristics.

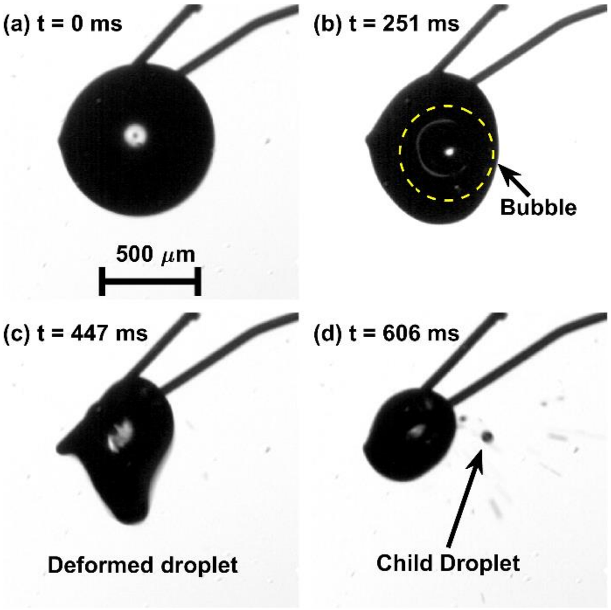

Figure 5.5, Different instances during SDF evaporation tests of a butanol droplet suspended on Pt50.

These artifacts were observed for droplets suspended on platinum and quartz filaments, but their occurrence and intensity varied among tests, as summarized in Table 5.1. The tendency to form bubbles is greater for butanol than for glycerol, decreases with droplet size, and results in more intense puffing for platinum than for quartz. For 15 μm SiC fibers, evaporation took place smoothly in all cases, with the only exception of tests with 500 μm butanol droplets, where some bubbling appeared but only at the very end of their lifetime (e.g., in one case it started when the droplet size fell below 58 μm). Therefore, it is not possible to propose simple rules to predict the onset of these artifacts, since they depend on the particular combination of experimental conditions. The formation of bubbles requires reaching nucleation conditions at some locations inside the droplet, which depends on both heat transfer through the fiber and liquid properties.

Table 5.1, Experimental occurrence of puffing or bubbling events for different fuels and conditions.

Fuel	d_0	Pt - 25μm	Pt - 50μm	Quartz - 100μm
Butanol	450 μm	Puffing	Puffing	Bubbling
	800 μm	Puffing	Puffing	Bubbling
Glycerol	450 μm	No	Micro-explosion	No
	800 μm	No	Puffing	No
	1076 μm	N/A	No	N/A

In order to further explore this hypothesis, the temperature profile along the fiber is calculated with the model described in Chapter 3.1.3 for different test conditions. The results are shown in Figure 5.6, in terms of the average temperature of the fiber in the portion inside the droplet, $\overline{T}_f$. As a reference, the critical temperatures for butanol and glycerol are indicated. Vapor nucleation is expected to occur when the liquid reaches its superheating temperature, typically around 90% of T_c (Avedisian, 1985), so the critical temperature can be used as a valid reference to assess bubble formation. The results in Figure 5.6 are fully consistent with the experimental observations summarized in Table 5.1. For the case of butanol, the fiber temperature widely exceeds its critical temperature for both Pt wires, becoming close to T_c at the very end of the droplet lifetime for SiC fibers. For glycerol, this only clearly happens for Pt-50, whereas for Pt-25 (for which no bubbling is observed) the critical temperature is only exceeded during the final instants of the evaporation process.

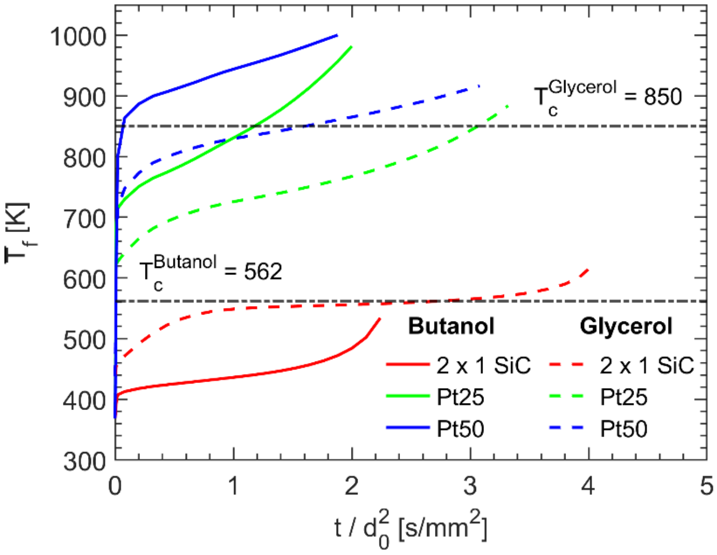

Figure 5.6, Predicted temporal evolution of the average temperature of the fiber inside the droplet for butanol (solid lines) and glycerol (dashed lines) for different fiber arrangements and $d_0 = 800\mu m$.

This simple analysis clearly demonstrates that the thermal disturbance due to the fiber can explain abnormal behaviors (bubbling or even micro-explosions for monocomponent droplets) that significantly modify the actual evaporation process of the liquid under study and, hence, must be avoided. Since it is not possible to obtain a valid evaporation rate from tests showing these experimental artifacts, they will not be further considered for subsequent analysis in the following sections.

5.2. Theoretical analysis of the artifacts

This section intends to evaluate and parameterize the impact of each experimental artifact due to additional heat transfer modes by introducing a simplified analysis based on global characteristic parameters of the problem of an isolated droplet evaporating within a high-temperature gas coflow.

Droplet evaporation is driven by the total heat transferred to the liquid, $\dot{Q}_t$. Assuming that the droplet vaporizes under the quasi-steady regime, where all the heat input to the droplet is used to evaporate, it can be stated that:

$$K \sim \frac{\dot{Q}_t}{mL_v} = \frac{\dot{Q}_{gc} + \dot{Q}_{fc} + \dot{Q}_{rd} + \dot{Q}_{cn}}{mL_v} = \frac{\dot{Q}_{gc}}{mL_v}\left(1 + \frac{\dot{Q}_{fc}}{\dot{Q}_{gc}} + \frac{\dot{Q}_{rd}}{\dot{Q}_{gc}} + \frac{\dot{Q}_{cn}}{\dot{Q}_{gc}}\right) \tag{5.1}$$

Where $\dot{Q}_t$ is decomposed into the possible heat transfer modes: conduction of heat through the gas-liquid interface for hypothetical stagnant conditions ($\dot{Q}_{gc}$) and through the fiber-liquid interface ($\dot{Q}_{fc}$), absorption of radiative heat ($\dot{Q}_{rd}$) and the excess heat input due to convective effects with respect to conduction in stagnant conditions ($\dot{Q}_{cn}$). Since the only heat transfer mechanism intrinsic to the canonical problem is $\dot{Q}_{gc}$, Equation (5.1) can be rearranged as:

$$K_{can} \sim \frac{\dot{Q}_{gc}}{mL_v} \rightarrow K/K_{can} = 1 + FN + RN + CN \tag{5.2}$$

where K_{can} is the quasi-steady evaporation rate for the canonical case and *FN*, *RN* and *CN* are dimensionless numbers related to the fiber conduction, radiation and convective effects, respectively. According to Equation (5.2), departures from ideal conditions due to additional heat transfer modes result in deviations in evaporation rate with respect to actual canonical conditions, which can be readily estimated from *FN*, *RN* and *CN*, i.e., as proportional to the contribution of the respective mechanisms to the total heat flow. Although this is only strictly valid if the heat transfer modes admit superposition (expected to occur only for small departures from ideal conditions), Equation (5.2) is a useful framework to assess the magnitude of experimental artifacts as well as to identify the role of the different variables.

The conduction of heat through the gas-liquid interface for stagnant conditions can be readily obtained from the classical theory of droplet evaporation. If the droplet is assumed to vaporize at its boiling temperature (valid for $T_g \gg T_b$) in a quiescent atmosphere and the Stefan flow is neglected:

$$\dot{Q}_{gc} = \pi d_d Nu_{d,can} k_g (T_g - T_b) \tag{5.3}$$

Being $Nu_{d,can}$ the Nusselt number for a stationary droplet immersed in a stagnant gas ($Nu_{d,can}$=2) (Yang & Wong, 2002). It is worth noting that the aim of this simplified analysis is to parameterize the problem based on characteristic parameters of the problem. More accurate estimations for $\dot{Q}_{gc}$ are naturally possible, but the dependence on characteristic, known variables would be lost.

The heat transferred to the droplet due to fiber-liquid conduction, $\dot{Q}_{fc}$, can be calculated as the heat flow through the fiber cross-section at the droplet surface:

$$\dot{Q}_{fc} = 2\,n_f\left(\frac{\pi}{4}d_f^2\right)k_f\left.\frac{dT_f}{dx}\right|_{x=a} \tag{5.4}$$

In agreement with previous works (Csemány & Józsa, 2019), this heat scales with the fiber diameter squared and the fiber conductivity. In order to obtain $\dot{Q}_{fc}$, a good estimate of the fiber temperature gradient at the droplet surface is required. This can be readily and accurately calculated by means of models such as the one described in Chapter 3.1.3. However, with some simplifications, the required temperature gradient can also be estimated from the global parameters of the problem. For sufficiently thin fibers ($d_f << d_d$), the fiber can be approximated as a fin with $T_f \approx T_b$ at its base ($x = 0$), in a flow at T_g. According to the pin fin theory (Bergman et al., 2015), the temperature profile along the fiber is:

$$T_f(x) = T_g + \left(T_b - T_g\right)\exp\left(-\sqrt{4\,Nu_f\frac{k_g}{k_f}}\frac{x}{d_f}\right) \tag{5.5}$$

For negligible velocity of the hot gas, the fiber Nusselt number is $Nu_f = 0.3$ (Churchill & Bernstein, 1977). From Equation (5.5), the thermal gradient at the surface can be readily obtained, yielding the following expression for $\dot{Q}_{fc}$:

$$\dot{Q}_{fc} = 2\,n_f\left(\frac{\pi}{4}d_f^2\right)k_f\frac{(T_g - T_b)}{\sqrt{\frac{k_f}{k_g}\frac{1}{4\,Nu_f}}\,d_f} \tag{5.6}$$

Therefore, the dimensionless number *FN* accounting for the effect of the heat conduction through fibers on the droplet evaporation rate can be calculated as:

$$FN = \frac{\dot{Q}_{fc}}{\dot{Q}_{gc}} = n_f\frac{d_f}{d_d}\sqrt{\frac{k_f}{k_g}}\frac{\sqrt{Nu_f}}{Nu_{d,can}} \tag{5.7}$$

The heat input due to radiation absorption ($\dot{Q}_{rd}$) can be estimated from average values for the incident thermal radiative heat flux ($\dot{Q}_r^{"}$) and the radiation absorption efficiency factor ($\bar{E}_a$). If the droplet sees the radiation source under a solid angle Ω_d and neglecting the radiative emission from the liquid droplet (since $T_g >> T_b$), the resulting heat input to the droplet becomes:

$$\dot{Q}_{rd} = \pi\, d_d^2\, \bar{E}_a \frac{\Omega_d}{4\pi} \dot{Q}_r^{"} \tag{5.8}$$

The dimensionless *RN* can be therefore estimated as:

$$RN = \frac{\dot{Q}_{rd}}{\dot{Q}_{gc}} = \frac{d_d \bar{E}_a \frac{\Omega_d}{4\pi} \dot{Q}_r^{"}}{Nu_{d,can} k_g \left(T_g - T_b\right)} \tag{5.9}$$

The case of the last additional heat transfer mechanism (convective effects) is quite straightforward. The ratio of the heat input to the droplet due to convection ($\dot{Q}_{cn}$) and the heat input due to gas-liquid conduction ($\dot{Q}_{gc}$) can be simply expressed in terms of the droplet Nusselt number. Therefore, *CN* can be defined as:

$$CN = \frac{\dot{Q}_{cn}}{\dot{Q}_{gc}} = \frac{Nu_d - Nu_{d,can}}{Nu_{d,can}} = \frac{Nu_d}{2} - 1 \tag{5.10}$$

In this manner, the three proposed dimensionless numbers can be readily calculated based on global characteristic parameters of the problem, allowing a simple estimation of the impact of each experimental artifact on the droplet evaporation rate.

5.3. Analysis and evaluation of the artifacts

The magnitude of the different artifacts is now evaluated under a wide range of conditions, while also assessing the capability of the proposed simplified approach to capture their effects on the droplet evaporation behavior. To that end, this section will make use of both model predictions and experimental data.

5.3.1 Analysis based on model predictions

The model introduced in Chapter 3 can be used to evaluate the individual effect of each artifact on the droplet evaporation process, estimating its relevance for different conditions. For instance, Figure 5.7.a illustrates the variation of K/K_{can}, as predicted with the model, for butanol droplets attached by a single SiC fiber vaporizing in N_2 at 1400 K, for different fiber and droplet diameters. As expected, K/K_{can} increases with d_f and decreases with d_0, consistently with the relative importance of the heat transferred through the suspension fiber compared with the heat received through the gas-liquid interface. As it can be seen, even a low-conductivity material like

SiC (k_f = 2 W/m/K) can significantly enhance the evaporation rate of a 500 µm droplet (by ~20%) when the fiber size is sufficiently large (d_f = 60 µm).

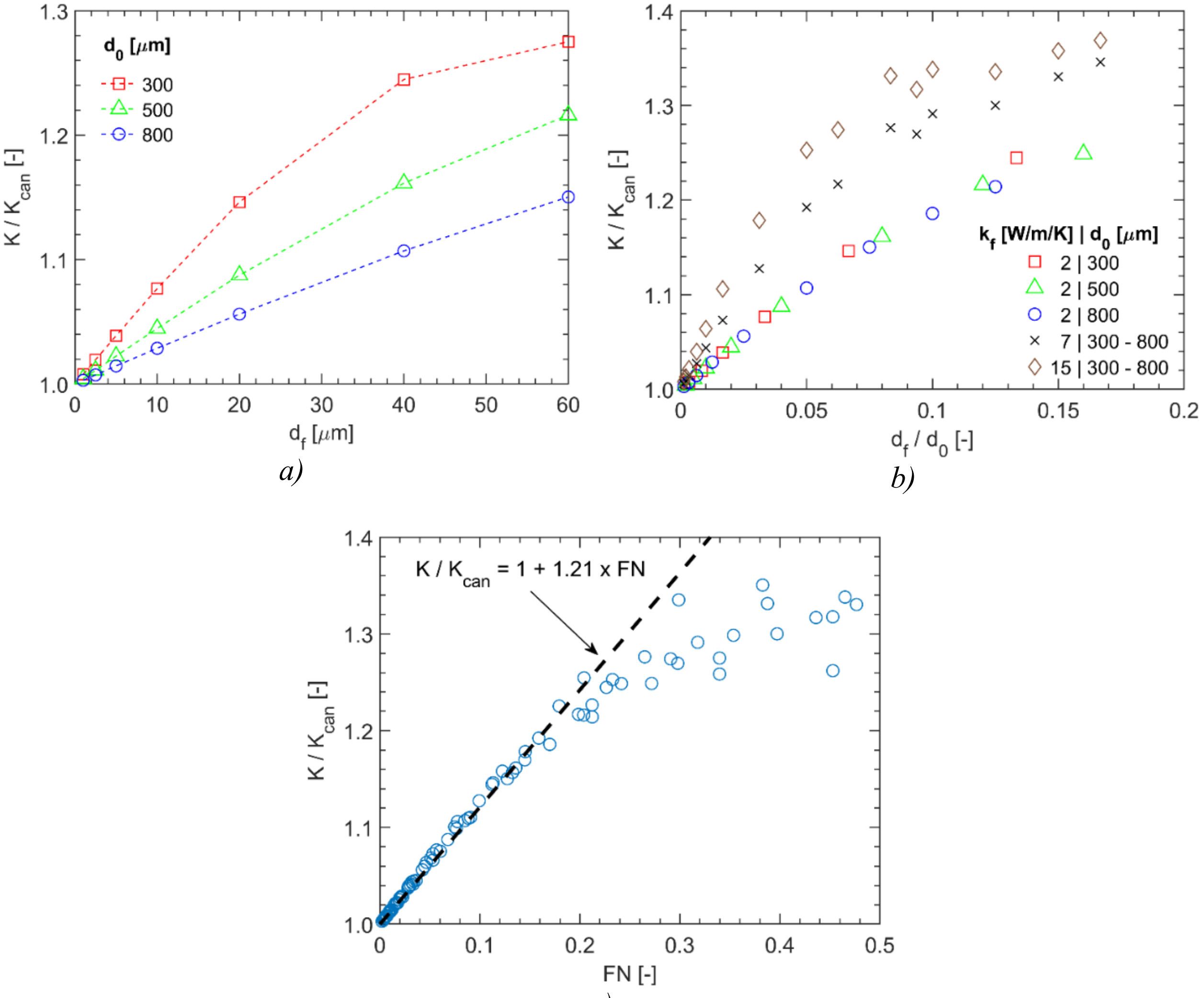

a)

b)

c)

Figure 5.7, Calculated K/K_{can} for different droplet and fiber configurations. (a) Effect of d_f and d_0 for butanol droplets suspended on a single SiC fiber, T_g = 1400 K; (b) K/K_{can} as a function of d_f/d_0 for butanol and different fiber conductivities, T_g = 1400 K. (c) K/K_{can} as a function of FN for a wide range of conditions: butanol and glycerol, T_g = 700 - 1400 K, d_f=1 - 60µm, d_0=300 - 800µm, k_f=2 - 15 W/m/K.

According to (Avedisian & Jackson, 2000; Farouk & Dryer, 2011; Yang & Wong, 2002), the fiber-to-droplet diameter ratio is a representative quantity for the fiber conduction artifact. This is also confirmed in this study, where all the data in Figure 5.7.a have been plotted against d_f / d_0 in Figure 5.7.b and get perfectly aligned along a narrow band (see data for k_f = 2 W/m/K). However, the fiber conduction artifact also depends on the thermal conductivity of the material, as confirmed by the predictions shown in Figure 5.7.b, showing that the deviation in K consistently increases with k_f.

Similarly, other parameters like the number of fibers or Nusselt numbers also modify the relative importance of the different heat transfer modes and should be considered. This is precisely the purpose of *FN* (Equation (5.7)), expressing the ratio between heat conduction through the fiber and at the droplet-gas interface. Figure 5.7.c represents K/K_{can} as a function of *FN* for all the test cases analyzed: a total of 116 combinations, including different liquids (butanol and glycerol) and a wide range of gas temperatures (700 and 1400 K), initial droplet size (300 - 800 μm), fiber diameter (1 - 60 μm) and fiber thermal conductivity (2-15 W/m/K). Despite the broad range of conditions considered in these simulations, all data points collapse in Figure 5.7.c to depict a very well-defined trend. Furthermore, the dependency is practically linear for $FN<0.2$, as predicted in the simplified analysis of section 5.2, and quite close to $1+FN$. Actually, the best fit in that interval is obtained for $K/K_{can}=1+1.21\times FN$. The factor 1.21 can be interpreted as a calibration factor to match the actual thermal behavior of the fiber, not perfectly captured in this order-of-magnitude analysis (in particular, the temperature gradient is roughly estimated from the pin fin theory for uniform gas temperature). Anyway, this appears to be quite a modest correction. As *FN* increases beyond 0.2, linearity is gradually lost, as could be expected since the addition of heat transfer modes is only valid for small departures from canonical conditions. For large fiber sizes and/or conductivities, the problem becomes far more complex, temperature profiles in the droplet and fiber are no longer 1-D and the solution does not admit superposition. As reported in (Han et al., 2016), for sufficiently thick fibers the evaporation rate can even start to decrease, since the fiber heating rate is slower, reducing in that way the heat input to the droplet and *K*. In any case, this analysis is mainly focused on the region not very far from canonical conditions, where deviations in evaporation rate can be estimated or even, at least in a first approximation, corrected; cases with large *FN* values will result in large deviations and, in those cases, rough estimates could be more than enough to assess the magnitude of this experimental artifact.

As for the radiation artifact, Figure 5.8.a shows the impact of the incident radiative heat flux and initial droplet size on K/K_{can} as predicted for unsuspended droplets. An increasing trend exists between K/K_{can} and d_0 due to a larger effective surface for radiative heat absorption. Obviously, increasing $\dot{Q}_r''$ also enhances the evaporation rate, so that a radiative heat flux of 150 kW/m^2 would increase the evaporation rate of 600 μm droplets by approximately 75%. Such a thermal radiative heat flux could be perfectly reached in furnaces (e.g., hot walls at 1400 K behaving as a grey body with $\varepsilon = 0.7$), and therefore a careful assessment of this effect should be considered when extracting droplet evaporation characteristics under high-temperature conditions, particularly when using big droplets.

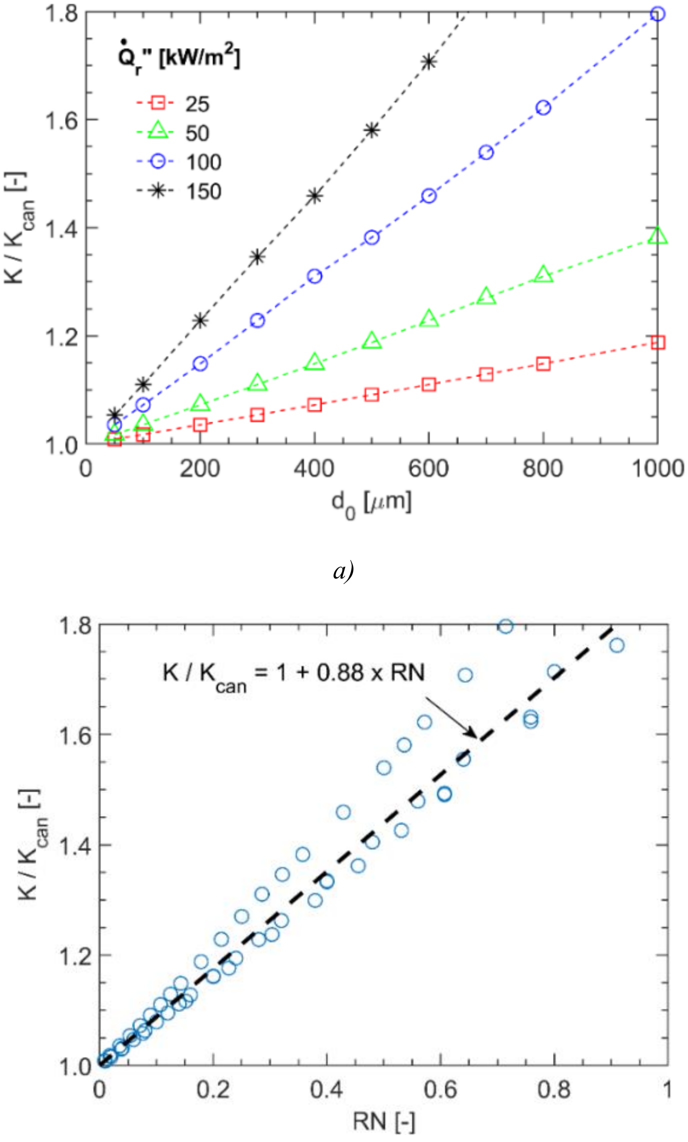

a)

b)

Figure 5.8, (a) Calculated K/K_{can} for unsuspended butanol droplets along with d_0 (50 – 1000 μm) for different $\dot{Q}_r''$ (25 - 150 kW/m^2) at T_g = 1400 K, $\Omega=4\pi$, $\bar{E}_a = 0.75$. (b) Calculated K/K_{can} along with RN for a wide range of conditions: butanol and glycerol, T_g = 700 - 1400 K, d_0=50 – 1000 μm, $\dot{Q}_r''$ =25 - 150 kW/m^2, $\Omega=4\pi$, $\bar{E}_a = 0.75$.

Analogously to the case of fiber conduction, the magnitude of the radiation artifact depends on several parameters. Once again, the simplified approach proposed in section 5.2 aims to unify all of them into a single non-dimensional 'radiation number', *RN* (Equation (5.9)). Figure 5.8.b shows the variation of K/K_{can} versus *RN* for a wide range of test conditions (butanol/glycerol, T_g=700- 400 K, d_0=50-1000 μm, $\dot{Q}_r''$=25-150 kW/m^2). A clear correlation and even a good linearity can be observed for the whole range explored, with slight differences when the fuel and T_g are changed. Again, the simplifications applied to obtain a *RN* based on global characteristic parameters are the cause for these differences. For instance, it should be noted that *RN* is defined in Equation (5.9) based on the instantaneous droplet diameter, d_d. This implies a continuously-changing RN for each test case, whereas in Figure 5.8.b a single representative RN is assigned to each simulation based on its initial droplet size, d_0. The evaluation of properties can also cause some slight differences when modifying the fuel or the gas temperature. All the required gas properties are estimated based on the one-third rule proposed by Sparrow and Gregg (1985), assuming that the droplet surface is at T_b. Overall, a calibration factor of 0.88 provides the best fit for the whole set of data (see the linear fitting in Figure 5.8.b).

Regarding the effect of forced convection on the deviation of the droplet evaporation rate from the canonical case, Figure 5.9.a presents the model results for a range of test conditions (d_0=50 - 1000 µm, v_g = 0.25 - 1 m/s). As expected, the relevance of forced convection increases with d_0 and v_g, since these parameters increase Re (and, therefore, also Nu). These cases, along with additional simulations changing the fuel (butanol/glycerol) and T_g (700 - 1400 K) are presented in Figure 5.9.b, where a clear linear correlation is found between K/K_{can} and CN. In this case, these results were to be expected, since CN is just a derivation of the Nusselt number for the droplet, and the dependence of the evaporation rate with Nu is well established (Abramzon & Sirignano, 1989). Even though Nu is expected to provide a good estimate for convective effects, a coefficient of 0.54 is obtained, ascribed to the use of the initial diameter in CN and the fact that Stefan flow is neglected in this order-of-magnitude analysis.

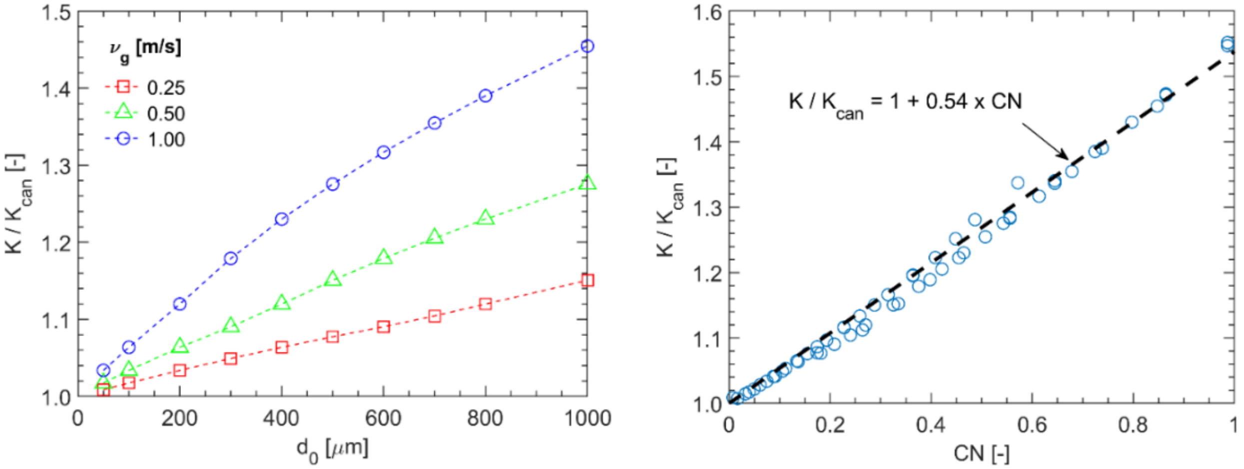

a) b)

Figure 5.9, (a) Calculated K/K_{can} for unsuspended butanol droplets along with d_0 (50 - 1000 µm) for different v_g (0.25 - 1.00 m/s) at T_g = 1400 K. (b) Calculated K/K_{can} along with CN for a wide range of conditions: butanol and glycerol, T_g =700 - 1400 K, v_g =0.25 - 1 m/s, d_0 =50-1000 µm.

5.3.2 Analysis based on experimental data

This section intends to evaluate the impact of the different artifacts for isolated droplet evaporation experiments, assessing also the ability of the proposed dimensionless numbers to accurately capture this impact for a wide range of experimental conditions. To that end, Figure

5.10 shows the isolated droplet evaporation results obtained at the SDF setup for a total of 225 cases, including different fiber arrangements, fuels, droplet sizes, etc. (results already introduced and discussed in section 5.1), as well as the unsuspended free-falling droplet experiments obtained at the DCF (reported in detail in (Muelas et al., 2020)).

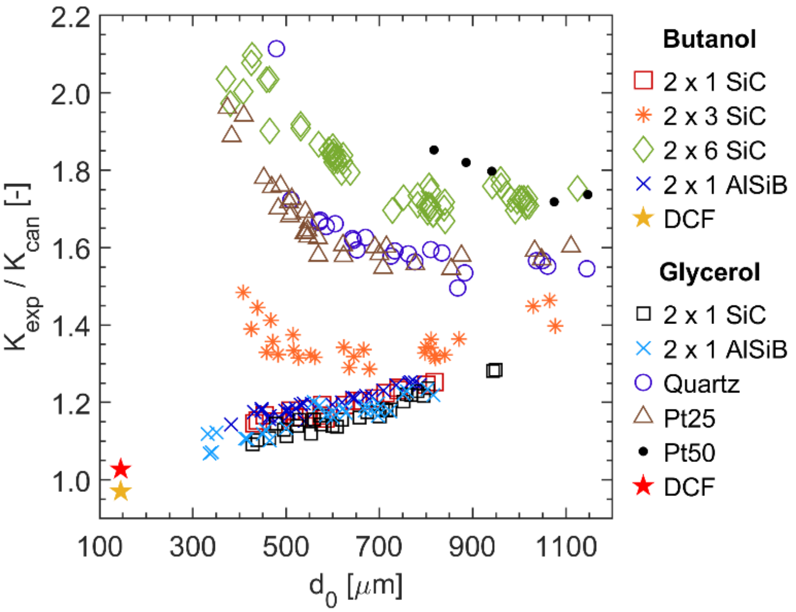

Figure 5.10, K_{exp}/K_{can} vs. d_0 for different fuels and fiber arrangements.

As discussed before, some of the results from the SDF setup display clear signs of experimental artifacts, with K_{exp}/K_{can} values strongly depending on the fiber arrangement as well as on the initial droplet size. The experimental data with the lowest deviation from the canonical, artifacts-free case corresponds to very thin fibers (d_f =11 - 15 µm) of low-conductivity material (AlSiB and SiC) and small droplets (d_0 ~ 400 µm). This combination simultaneously reduces the non-desired additional heat transfer mechanisms to a point where K_{exp}/K_{can} ~ 1.10. On the contrary, more conductive fiber arrangements (higher k_f and/or larger fiber cross-section) in combination with small droplets can result in large errors in the measured evaporation rate, up to ~100%, as compared to the canonical condition. As already noted, Figure 5.10 only shows the cases with a smooth evaporation process, removing the experiments where internal bubbling or puffing events were detected (see Figure 5.5), with even larger errors in K. In contrast with the SDF results, experimental data obtained at the DCF setup display much smaller deviations from the canonical evaporation rate (~3%). This is ascribed to the absence of suspension medium, as well as to the low radiation absorption and weak convective effects arising from the very small droplet sizes used in these experiments.

In Figure 5.11, all the K_{exp}/K_{can} values shown in Figure 5.10 are plotted against (FN+RN+CN) which, as proposed in section 5.2, represents the combined effect of the various experimental artifacts. As in the previous section, all properties required to calculate those dimensionless numbers are evaluated by following the 1/3 rule (Sparrow & Gregg, 1958) and assuming a droplet surface temperature equal to the fuel's boiling point.

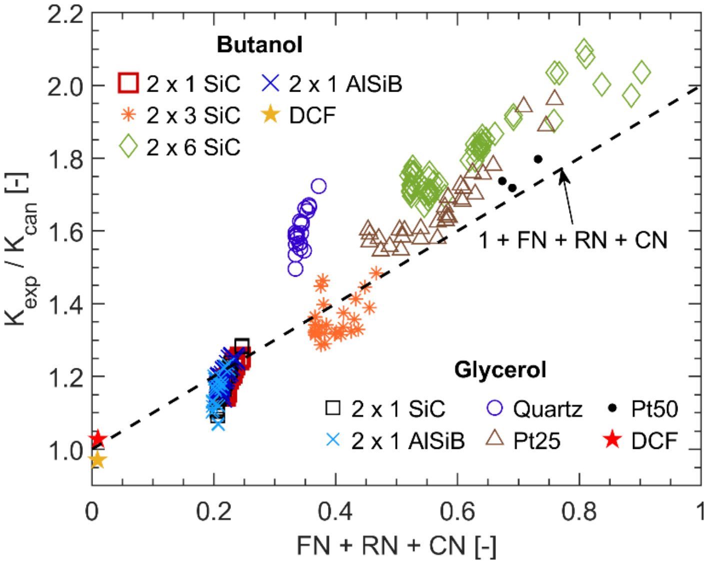

Figure 5.11, K_{exp}/K_{can} vs. (FN+RN+CN), for SDF and DCF experimental results. The dashed line represents Equation (5.2).

Despite the widely different trends observed in Figure 5.10, the data points in Figure 5.11 depict a well-defined tendency and, moreover, show a remarkable agreement with Equation (5.2): $K_{exp}/K_{can} = 1 + (FN + RN + CN)$. As discussed before, the experimental evaporation rates obtained in the fiber-free DCF setup show negligible deviations from the canonical values, in accordance with the very small values estimated for their cumulative dimensionless numbers. The SDF tests cover a much wider range of $FN+RN+CN$ values (namely, between 0.2 and 0.9), which translates into substantially different K_{exp}/K_{can} values, in agreement with Equation (5.2). This good alignment of the experimental data is believed to clearly support the validity of the proposed approach, as well as the ability of the dimensionless numbers to capture the shifts in droplet evaporation rate caused by these artifacts (at least for the range explored in Figure 5.11). Here it is worth noting that the simulations in Figs. 5.7.c, 5.8.b and 5.9.b provided with linear fitting equations, which can be used to improve the agreement of the experimental data with Equation (5.2). Namely, K_{exp}/K_{can} could be plotted against ($1 + f_{cd}$ FN + f_{rd} RN + f_{cn} CN), being $f_{cd} = 1.21$, $f_{rd} = 0.88$ and $f_{cn} = 0.54$ correction factors obtained from the aforementioned linear regressions. However, in view of the quite good agreement in Figure 5.11, the use of these correction factors is deemed unnecessary.

Among the various fiber arrangements presented in Figure 5.11, the cases using a quartz fiber show the largest deviations from the predicted linear behavior. This discrepancy is hypothesized to stem from the larger diameter of the quartz fibers (100 µm) and the smaller droplet-to-fiber diameter ratio since, as discussed before, the proposed simplified approach's validity is more suitable for thin fibers. Therefore, although the authors opted to include these data in the plot, they are not a good reference to evaluate the quality of the agreement with dimensionless numbers.

Published studies from other authors have been thoroughly revised to identify experimental data that could be analyzed in the framework of the proposed approach. Several data sets have been selected, corresponding to conditions significantly different from those presented above and, at the same time, providing all data required to evaluate K_{exp} and K_{can} as well as the corresponding *FN*, *RN* and *CN*. Results from (Nomura et al., 1996; Yang & Wong, 2001, 2002) are presented in Figure 5.12 along with the already discussed SDF and DCF data, adding therefore results for a different fuel (heptane), vaporizing at significantly lower environmental temperatures (471 and 750 K). As detailed in Chapter 3.2.1, the experiments of Nomura et al. (1996) are known to be affected by fiber conduction effects and the absorption of thermal radiation. Yang and Wong quantified in (Yang & Wong, 2001) these effects and provided a valuable analysis on the calculation of radiative absorption by the droplet. The geometric optics method and a simplified effective surface absorptance approach yielded identical results when the effective absorptance ($\bar{E}_a$) is set as 0.93 (Yang & Wong, 2001). Using this approach, they modelled the droplet evaporation curves from microgravity experiments conducted by Nomura considering: a) the absence of both fiber conduction and radiation absorption (i.e., canonical case without artifacts), b) including only radiation absorption, and c) including both radiation absorption and fiber conduction (i.e., reproducing the full experiment by Nomura). The latter two cases have been included to Figure 5.12 for the three ambience temperatures explored in (Nomura et al., 1996; Yang & Wong, 2001), yielding a remarkably good agreement with the proposed Equation (5.2). The relevance of radiation becomes evident, with an increase in the droplet evaporation rate of 13, 19 and 34% solely due to this artifact (for T_g= 471, 555 and 741 K, respectively). If fiber conduction through the 150 μm quartz filament is added, this deviation increases to 66, 72 and 90%.

A second set of data is obtained from (Yang & Wong, 2002), in this case, exploring the fiber conduction and forced convection effects. Due to the specific experimental setup used, radiative heating can be considered to be negligible, and therefore, a droplet evaporation model accounting only for the additional effects of fiber conduction and convection is able to reproduce the experiments. Model calculations allow to separate both effects, since in (Yang & Wong, 2002) the droplet evaporation curves predicted for a no-fiber case were added, along with those accounting for different quartz fiber sizes. These two cases can be discerned in Figure 5.12, where the effect of forced convection becomes apparent for the rather big-sized droplets tested in (Yang & Wong, 2002) (700 and 1000 μm). Namely, an enhancement of 96% can be ascribed to this effect for a 1000 μm droplet vaporizing at 750 K. If a fiber is added (50, 150, 300 μm), this deviation increases to 112, 145 and 190%, respectively. Again, all these cases align reasonably well with the linear correlation proposed in Equation (5.2), further supporting the use of these dimensionless numbers to estimate the deviations in droplet evaporation rate due to experimental artifacts.

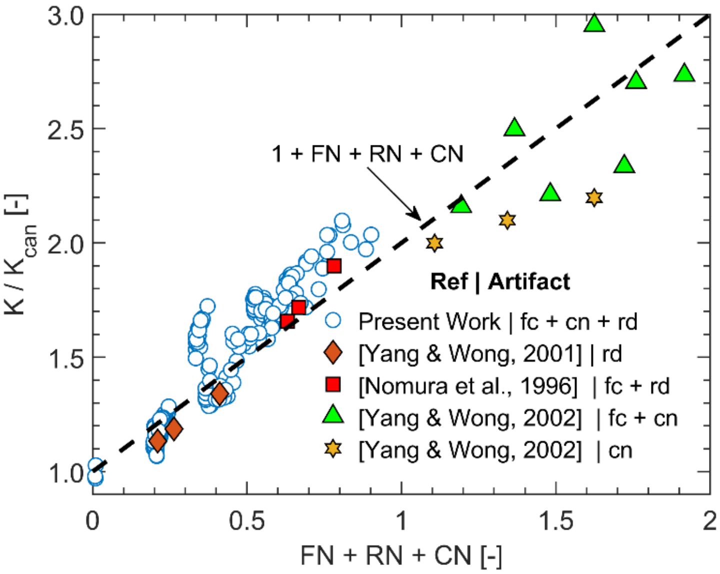

Figure 5.12, Evolution of the K/K_{can} along with the cumulative effect of non-dimensional numbers for the three artifacts (fiber conduction, convection and radiation: fc, cn and rd, respectively), extended for literature data from (Nomura et al., 1996; Yang & Wong, 2001, 2002). The dashed line represents Equation (5.2).

As it can be observed from the reported experimental data, the occurrence of several artifacts usually takes place simultaneously, so that the separate effect of each artifact can only be discerned either by applying some simplifying assumptions or by using evaporation models. For suspended, stationary droplet tests at high temperatures, the effects of fiber conduction and radiative heating are, arguably, the most relevant ones and their combined effect can be estimated based on model predictions. Figure 5.13 shows the values of K/K_{can} predicted with the model described in Chapter 3 as a function of FN and RN, for moderate deviations from canonical conditions (both FN and RN below 0.5). This plot can be used as a two-entry chart where the magnitude of the enhancement in droplet evaporation rate due to these artifacts can be readily estimated from the values of both dimensionless numbers as the only inputs required. Iso-lines in the low FN/RN region are straight lines, as predicted by Equation (5.2). Larger departures from canonical conditions result in increased curvature of the iso-lines, due to the non-additive nature of the different heat transfer modes. The model can account for this behavior, as long as the configuration can be reasonably assumed as 1-D, and Figure 5.13 can provide better estimates than Equation (5.2) for the combination of conduction and radiation artifacts. If convective effects are not negligible, its contribution could be reasonably estimated by adding 0.54×CN (see Figure 5.9.b) to calculate the total deviation in K due to experimental artifacts.

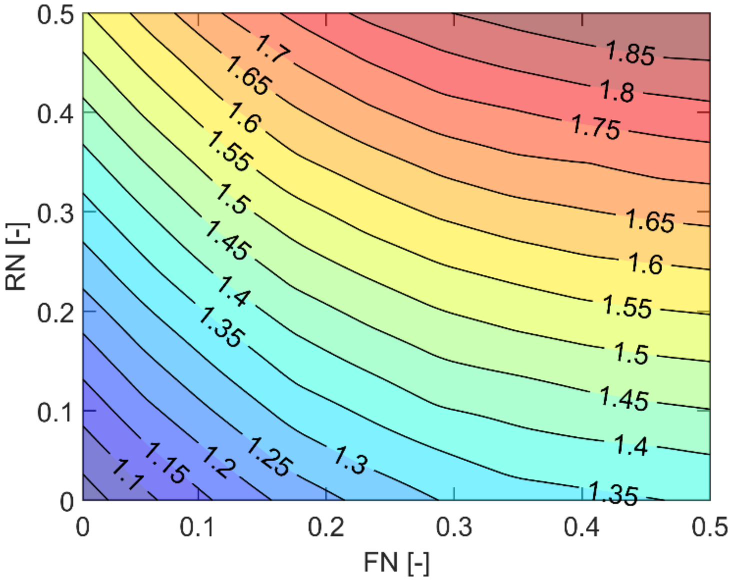

Figure 5.13, Variations of K/K_{can} along with the changes in FN and RN, as predicted by the evaporation model.

In summary, experimental and modeling studies clearly confirm that measured evaporation rates can significantly deviate from the value that would be obtained in canonical situations, and the magnitude of this deviation varies with the particular experimental conditions. Actually, all real-world tests are affected to some extent by the discussed artifacts, which can be estimated from the reported experimental and model results (e.g., Figures 5.12 and 5.13). Nevertheless, rather small deviations can be attained by suitably selecting test conditions, the most favorable situations being those using unsuspended droplets or very thin supporting fibers, low-radiative environments and small convective effects (ideally, quiescent atmosphere in microgravity).

6. Development of evaporation surrogates using a pseudo-component approach

This chapter develops and validates a systematic methodology to formulate surrogates that can efficiently mimic the evaporation behaviors of real fuel droplets at elevated temperatures. The surrogates are designed by employing the discrete-component evaporation model described in Chapter 3, using also the sensitivity analysis (SA) assessment presented in Chapter 4. Specifically, this assessment is used to determine the most important physical properties that influence the fuel droplet evaporation behaviors. Once this is done, the pseudo-component approach is employed to characterize the target fuel and to estimate its physical properties based on hypothetical components. Comparing each pseudo-component (PC) with alkane hydrocarbons based on the most relevant properties (as identified from the SA) led to finding the most similar alkanes to those PCs. Thus, the proposed methodology allows to obtain the optimal palette in a systematic manner. After this palette is chosen, the final step optimizes the mass fractions of the different constituents to emulate the evaporation characteristics of the target fuel by means of a multi-objective genetic algorithm. The fuel droplet evaporation is modeled for those selected compositions, and the results are validated against high-temperature experimental data obtained at a free-falling droplet facility (DCF, see Chapter 2). The method is applied on three different practical fuels, covering a broad range of real applications.

6.1 Composition and properties of the target fuels

The target fuels selected as case studies for surrogate formulation are a commercial heating oil (fuel oil No. 2), an automotive diesel and a standard Jet A fuel. The fuel samples were characterized to determine their most important physicochemical properties, which are presented in Table 6.1. According to the analyzed data, these three fuels have almost identical mass fractions of carbon and hydrogen. However, there are substantial differences among their densities and distillation curves. Some properties were not available (for example, average molecular weight for diesel), but the surrogate algorithm is designed to flexibly handle the modeling problem by considering a variable number of bulk properties as inputs. In addition to the data listed in Table 6.1, the distillation curves were measured for the three fuels. Figure 6.1 shows these curves for diesel, heating oil and Jet A, which were obtained by ASTM-D86 (ASTM, 2012), Advanced Distillation Method (Bruno, 2006) and ASTM-D2887 (ASTM, 2019), respectively.

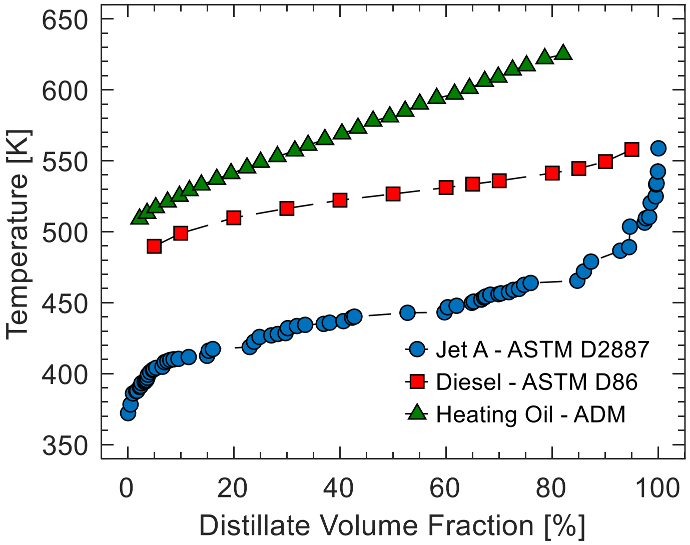

Figure 6.1, Distillation curves for diesel, heating oil and Jet A.

Table 6.1, Main properties of the three target fuels

	Heating Oil[a]	Diesel	Jet A[b]
Molecular formula	$C_{13.21}H_{24.63}$	-	$C_{10.60}H_{19.63}$
$\overline{MW}$ (kg kmol^{-1})	184.50	-	146.80
% C (mass)	86.40	86.00	86.60
% H (mass)	13.60	13.30	13.40
% O (mass)	0	0	0
C/H (-)	0.54	-	0.54
HHV (MJ kg^{-1})	44.60	45.31	45.39
Density at 20 °C	861	838	791
Viscosity at 40 °C	3.43	2.39	-
T5 - T80 (°C)	243 - 350	216 - 268	130 - 191

[a] *From ref. (Muelas et al., 2019b)*, [b] *From ref. (Muelas et al., 2018)*

6.2 Multicomponent droplet evaporation model considering pyrolysis reactions

As mentioned before, the surrogate formulation procedure uses a multi-component droplet evaporation model (described in Chapter 3) to predict the evaporation behavior for different blends. Since the methodology proposed here focuses on evaporation surrogates for elevated temperature applications, DCF tests and conditions (with gas temperatures in the order of 1730 K) are employed. At such high temperature environments, pyrolysis reactions in the vapor phase may have a significant impact on the droplet diameter evolution for certain hydrocarbon fuels. Muelas et al. (2020) recently investigated these effects for different pure alkanes, developing an analytical model that includes the effect of gas-phase pyrolysis on the isolated droplet vaporization characteristics by considering a one-step irreversible reaction coupled with the evaporation process for mono-component droplets.

Since, to best of the author's knowledge, there is currently no analytical model able to predict the effect of pyrolysis on the droplet vaporization process for the case of fuel mixtures, the current chapter includes these effects by employing a simplified empirical correlation. This simplified approach consists in simulating the heat sink due to pyrolysis by adding a term related to the enthalpy of pyrolysis reaction (q_{pyr}) to the Spalding heat transfer number (B_t) (see equation 6.1). The value of q_{pyr} is adjusted so that the predicted quasi-steady evaporation rate matches the experimental observations.

$$\frac{d}{dt}(d^2) = -\frac{8k_v}{\rho_l\, C_p}\ln\left(1+\frac{C_p(T_g - T_s)}{Lv + q_{pyr}}\right) \tag{6.1}$$

The optimal value of q_{pyr} for some saturated alkanes (n-heptane, n-dodecane, n-hexadecane and n-icosane) is therefore calculated from the experimental data obtained at the DCF, being presented in Table 6.2.

Table 6.2, Values calculated as optimum for q_{pyr} *for different saturated, linear alkanes*

	C_7	C_{12}	C_{16}	C_{20}
q_{pyr} (MJ kg^{-1})	0.1275	0.2050	0.2895	0.3464

Figure 6.2 displays the predicted droplet evaporation curves obtained when these values of q_{pyr} are included in the simulations, along with the results of the pure evaporation model (i.e., without pyrolysis corrections), comparing these curves with the DCF experimental data. As shown in Figure 6.2, model predictions fit remarkably well the experimental data by employing the q_{pyr} correction factor. It is worth to note that this correction was not required for the data previously reported in this dissertation for alcohol droplets (ethanol, butanol, glycerol) vaporizing at high-temperature conditions, given the much lower tendency to pyrolyze for these compounds (Muelas et al., 2020).

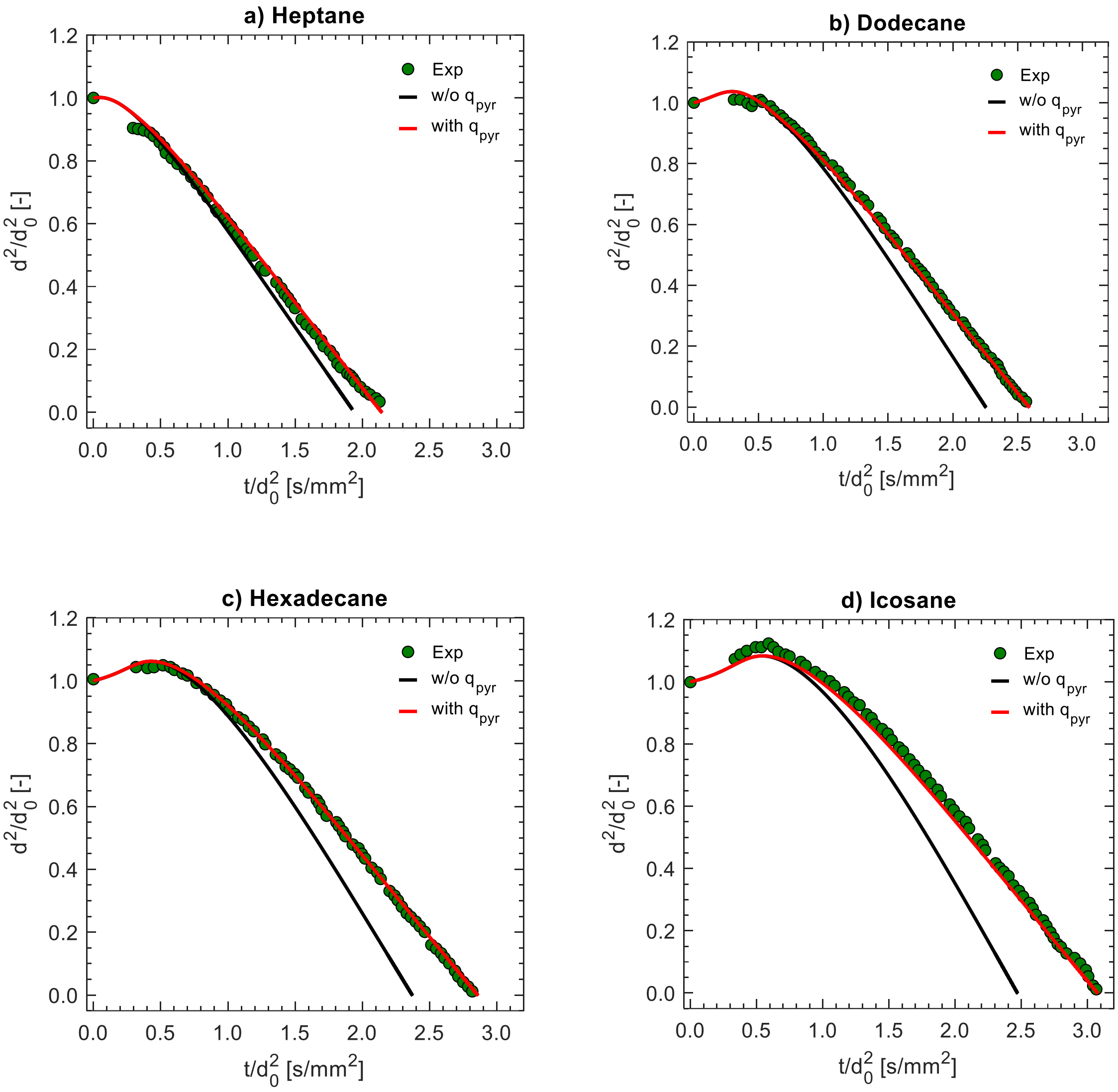

Figure 6.2, Predicted and experimental evaporation curves for different alkanes. The q_{pyr} *values of each component are presented in Table 6.2*

Finally, as it can be observed in Figure 6.3, there is a linear trend between the enthalpy of pyrolysis reaction (q_{pyr}) and the alkane's carbon atom number. Therefore, and due to the lack of experimental data for other alkanes, a linear regression is applied to interpolate the correction factors for different paraffinic components.

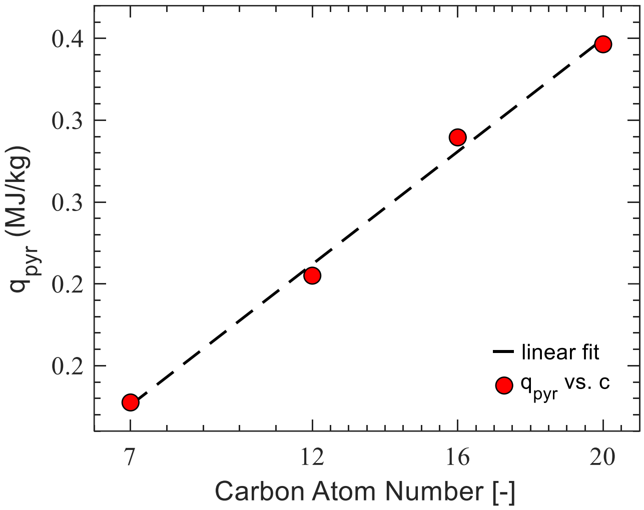

Figure 6.3, Correction factor, q_{pyr}, versus carbon atom number extracted for different linear alkanes vaporizing at the DCF test conditions.

6.3. Fuel properties and evaporation metrics

In the design of an efficient surrogate, there are two key steps that have to be addressed, namely: first, to choose the set of components composing the mixture and, second, to determine their optimal mass/molar fractions. The most common approach to deal with the first step has been to define a palette based on predefined components (Chen et al., 2016; Elwardany et al., 2016; A. l. Muelas et al., 2019; Su & Chen, 2015). Although this approach may satisfy the requirements for a particular application, due to the lack of a defined procedure, the final success of the process heavily depends on previous knowledge and sometimes even on subjective criteria. A well-defined procedure for the selection of palette compounds would help to systematize this task and to find the most suitable components. However, to the best of the author's knowledge, there are no precedents in the literature in that respect. This chapter attempts to propose a systematic procedure, which can be divided into two different steps. The first one, which was previously addressed in the Sensitivity Analysis (SA) presented in Chapter 4.3, is the identification of the physico-chemical properties with a stronger impact on the droplet vaporization characteristics. The second step, treated in the next section, consists in selecting the compounds that enable the closest agreement with respect to the properties of the target fuel.

In order to evaluate the impact of the different properties on the fuel droplet evaporation behavior, the evaporation curve is quantized into five different metrics, intended to describe the evaporation features of the fuel droplet in a concise manner. Figure 6.4 depicts the evolution of the droplet diameter squared as a function of time, both of them normalized by the initial droplet diameter squared, d_0^2. The five metrics selected to parametrize this curve are:

1. t_c (s/mm^2): heat-up time
2. t_{20} (s/mm^2): evaporation time from $d^2/d_0^2 = 0.6$ until $d^2/d_0^2 = 0.2$
3. t_{60} (s/mm^2): evaporation time from $d^2/d_0^2 = 1.0$ until $d^2/d_0^2 = 0.6$
4. t_t (s/mm^2): total evaporation time
5. K (mm^2/s): Quasi-steady state evaporation rate, calculated as the slope of the curve between $(d/d_0)^2 = 0.6$ and 0.2. $1/K$ would be the hypothetical time (normalized) required to completely evaporate a droplet under ideal quasi-steady state conditions.

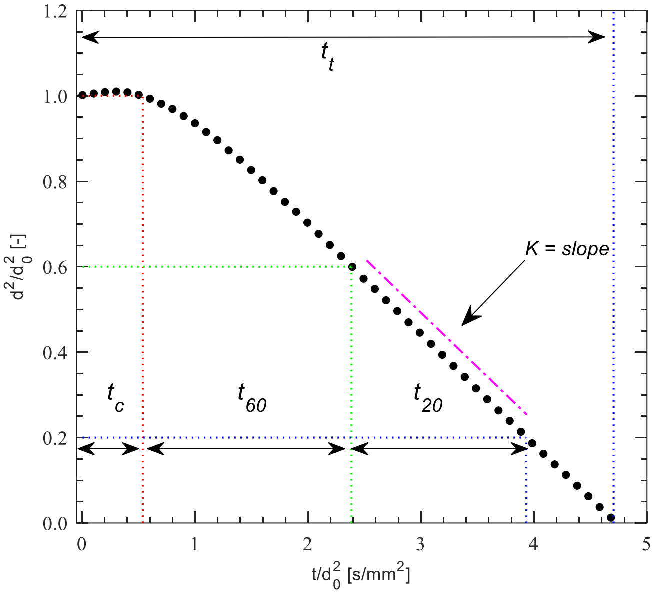

Figure 6.4, Droplet evaporation curve and associated metrics

After performing the aforementioned sensitivity analysis (see Section 4.3 for details), the physico-chemical properties which are found to have a stronger impact on droplet evaporation are the boiling point temperature (T_b) and the thermal conductivity of the vapor mixture (k_{mix}), followed by the heat capacity of the vapor mixture (Cp_{mix}), liquid density (ρ_l), liquid heat capacity (C_l) and latent heat of vaporization (L_v). As explained below, these properties will provide the reference data used to select the most suitable palette compounds.

6.4. Fuel surrogate modeling and optimization

Figure 6.5 describes the procedure applied to formulate and optimize the surrogate mixture for any target fuel, which is divided into three main steps. The first one aims to shrink the compositions of the target fuel into a mixture of a few pseudo-components (PCs) by lumping the similar compounds into groups that have close properties (Azimi et al., 2018; Riazi, 2005). Due to its simplicity and capability in reducing computation time, this method is specially favorable for the characterization of petroleum-based fuels composed of complex mixtures with a wide range of boiling point and molecular mass (Castells et al., 1992; Riazi, 2005). Although this approach shares mutual features with the quasi-discrete model (QDM) proposed by Sazhin et al. (2014), such as lumping similar constituents into a single component, there are still differences in the estimation procedure of the target fuel properties, since the current approach uses the Watson factor hypothesis (Castells et al., 1992; Riazi, 2005) to calculate the PCs on the basis of the distillation curve of the fuel and some of its bulk properties (average molecular mass, density and viscosity). Following the approach detailed in (Castells et al., 1992), the distillation curve of the target fuel is divided into a number of equal temperature intervals. Hereafter, each temperature interval is treated as a petroleum cut or PC, whose boiling point is set according to the average boiling temperature of the interval. By solving the conservation equations, the specific gravity for each PC is determined (for a detailed description of this procedure, see Appendix D). The rest of relevant properties for each PC is estimated on the basis of the correlations reported by Riazi (2005).

In the following step (2.1 and 2.2 in Figure 6.5), a similarity index is established based on the most important properties which were defined by the sensitivity analysis in Section 4.3. This index serves to quantitatively compare the PCs and a database of saturated alkanes in order to find the most similar real compound to each PC. Accordingly, the first and second steps are devoted to find the proper surrogate palette compounds in a systematic and unambiguous way. In the final step (stage 3 in Figure 6.5), a multi-objective optimization algorithm is employed to optimize the mass fraction of the designed mixture to match the fuel droplet evaporation curves obtained from experiments at the DCF.

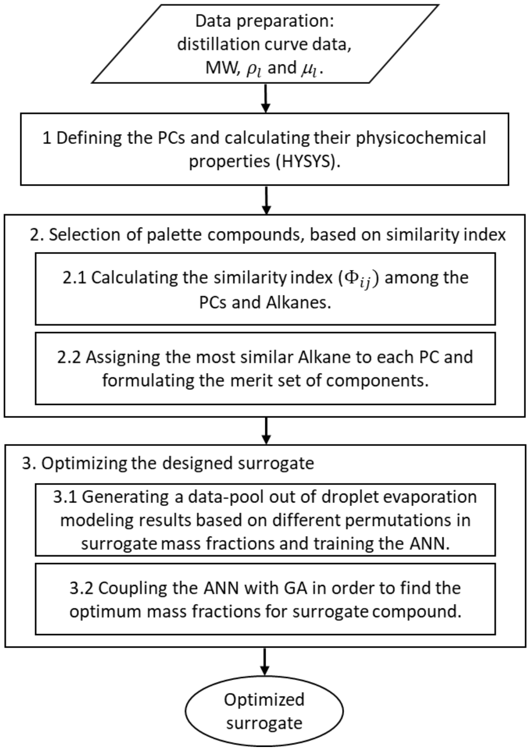

Figure 6.5, Block diagram of the procedure applied to formulate a surrogate.

These three steps are further described in the following paragraphs:

1. The first step consists in discretizing the target multicomponent fuel into three hypothetical pseudo-components. Therefore, three PCs are defined by dividing the distillation curve into three sections and assigning the average boiling point of each interval to each PC. Then, the specific density of each PC is calculated using the correlations presented in (Castells et al., 1992). The process for extracting the PCs from the input data is performed with the HYSYS software (Aspen, 2017). After obtaining the PCs mass fractions and their related state properties (such as average boiling point, critical pressure, critical temperature etc.), the physical properties of each PC can be estimated with the correlations presented in Appendix E. The number of PCs chosen here (3) is a compromise between the accuracy in the emulation of the evaporation curve and the CPU-work required to conduct the whole optimization method.

2. Next, a similarity index (Φ_{ij}) is used to identify a set of real alkanes with properties similar to those of the pseudo-components defined in the previous step. The alkanes included in the database are chosen by conducting a gas-chromatography analysis on the target fuel. The similarity index is defined as the rms of the Euclidean distance among the set of physicochemical properties of the PCs and those of the saturated alkanes (see Equation 6.2). These properties, ψ, are selected through the sensitivity analysis (described in Chapter 3.3) and include: T_b, k_{mix}, L_v, Cp_{mix}, ρ_l and C_l.

$$\Phi_{ij} = \sqrt{\frac{1}{n}\sum_{k=1}^{n=6}\left(\frac{\psi_{i,k}^{PC} - \psi_{j,k}^{Real}}{\psi_{j,k}^{Real}}\right)^2} \tag{6.2}$$

where, $\psi_{i,k}^{PC}$ is the kth property for the ith pseudo-component and $\psi_{j,k}^{Real}$ is the same property for the jth alkane. The physicochemical properties for the liquids are calculated as the average in the temperature interval from melting to boiling point, whereas the range from boiling to the critical point is used for vapor phase properties. Finally, the similarity between specific alkanes and pseudo-components is evaluated as the root mean square of the normalized errors. The most similar alkane to each PC is identified as the one minimizing Φ_{ij}. Thus, the hypothetical pseudo-components in the initial ternary mixture (estimated in step 1) can be replaced by their corresponding alkanes, so that the surrogate will be defined as a blend of real compounds.

3. In this last step, an optimization tool is applied to find the mass fractions of the palette compounds that best reproduce the evaporation behavior of the target fuel. Since the simulation of multi-component droplet evaporation may require considerable CPU time, especially if using detailed numerical evaporation models, it can be convenient to reduce the number of simulations required to explore the whole compositional range. With this aim, the

procedure has been designed to perform the optimization from a limited set of predicted evaporation curves, obtained from calculations for a reduced set of mass fractions permutations in the mixture palette. Namely, 231 composition instances were evaluated, consisting of a regular grid with 5% mass fraction increments for each component. The evaporation metrics proposed in Section 6.3 were calculated for each instance, being these data tabulated and utilized to develop a universal predictor for evaporation metrics as a function of the blend mass fractions. Artificial Neural Networks (ANN) (Hagan et al., 1997) are employed for this task, as they offer the required plasticity to adapt to arbitrary, nonlinear relationships.

A multi-layer Perceptron Neural Network (Hagan et al., 1997) with two hidden layers and 10 neurons per layer is used to establish the relationship between surrogate composition and the predicted evaporation metrics (see Figure 6.6). The input layer consists of three neurons corresponding to the mass fractions of the ternary mixture (c_1, c_2 and c_3). The four neurons in the output layer provide the four metrics used to describe the evaporation curve, namely, t_c, t_{20}, t_{60} and t_t. Sigmoid activation functions are assigned for the two hidden layers and a linear activation function is considered for the output layer. The root mean square of relative error (RMSRE) in the prediction of test data is adopted as the stop-limit condition for the training process. The evaporation model results for the 231 instances are tabulated and randomly distributed to be used in the different stages of the training process: 50% for training the ANN (Levenberg–Marquardt algorithm), 25% for validation and the remaining 25% of the data is used as test set.

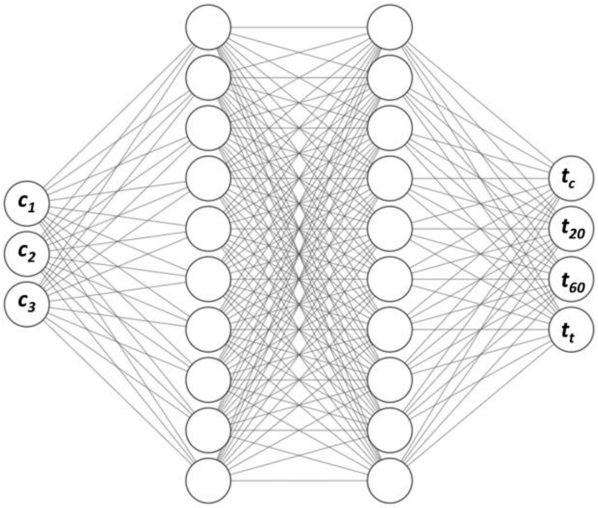

Figure 6.6, Architecture of the neural network used

Overall, the final evaluation of the performance of the three ANN developed for the three real fuels studied (i.e., diesel, Jet A and heating oil) showed that they could accurately predict the outputs, with a coefficient of determination above 0.97 and RMSRE below 0.05%. Once trained and validated, the ANN are employed to estimate the evaporation metrics for any blend composition.

The last step (3.2 in Figure 6.5) intends to find the optimum mass fractions to accurately match the target experimental evaporation curve. A multi-objective Genetic Algorithm (GA) utilizes the trained ANN to find the optimal mass fractions. GA is a powerful optimization tool already used in some previous studies on surrogate modeling (Bai et al., 2021; Kim & Violi, 2021). The optimization code uses built-in functions in MATLAB. In order to combine different evaporation metrics into a single cost function, a weighted-sum approach is employed (Kim & Violi, 2021). This allows converting a multi-objective optimization problem into a single-objective one. Besides, the individual weights can be adjusted to prioritize the metrics based on their importance. After running the optimization code, the optimal mass fractions are those that minimize the difference among the experimental target metrics and those predicted by the model. The objective function utilized in the optimization problem is defined by the following equation:

$$OF = \sqrt{\sum_{i=1}^{k}\{w_i O_i(c)\}^2} \qquad O_i = \frac{mtr_i^{exp} - mtr_i^{mdl}}{mtr_i^{exp}} \tag{6.3}$$

where *OF* is the objective function, w_i are the weights assigned to each cost function, O_i is the ith cost function defined as the relative difference between the experimental and the predicted evaporation metrics (mtr_i^{exp} and mtr_i^{mdl}, respectively), k is the number of cost functions (k = 4, equal to the number of evaporation metrics), c [c_1, c_2, and c_3] is the mass fraction vector defining the blend of three components, subjected to the following constraints:

$$0 \leq c_k \leq 1, \qquad \sum_{i=1}^{n} c_k = 1 \tag{6.4}$$

In the same manner, the w_i values are subjected to optimization during the minimization of *OF*, with the following constraints:

$$0.25 \leq {w_i}/{w_{\substack{j \\ j \neq i}}} \leq 4 \tag{6.5}$$

These limits were imposed to prevent neglecting any of the metrics, which could yield a lower global objective function but at the risk of great deviations in the individual evaporation metrics with the lowest weights. Finally, it is worth mentioning that the PCs mass fractions provided by Aspen HYSYS in the first step were set as the initial guess for this optimization algorithm to find the optimum values for the mass fraction vector *c*.

6.5. Results and discussion

The surrogate formulation procedure explained in the previous section has been applied to three different target fuels: diesel, Jet fuel and heating oil. These define a notably broad range of real, petroleum-based fuels of great practical interest. The following subsections describe the results obtained for each fuel.

6.5.1 Diesel

After defining three PCs for the diesel sample (the first step of the procedure described in Section 6.4), the three alkanes with the highest similarity indices were identified. The resulting palette compounds are n-undecane (C_{11}), n-tetradecane (C_{14}) and n-pentadecane (C_{15}). These components yielded similarity indices of 65.59% (C_{11}), 60.45% (C_{14}) and 57.50% (C_{15}) in comparison with their corresponding PCs. The optimization procedure (step 3.2 in Figure 6.5) yielded the following optimal mass fractions: 88.0% C_{11}, 10.7% C_{14} and 1.3% C_{15}.

Figure 6.7 shows the errors in the prediction of the various evaporation metrics for the whole range of mass fractions explored, along with the location of the aforementioned optimal mixture.

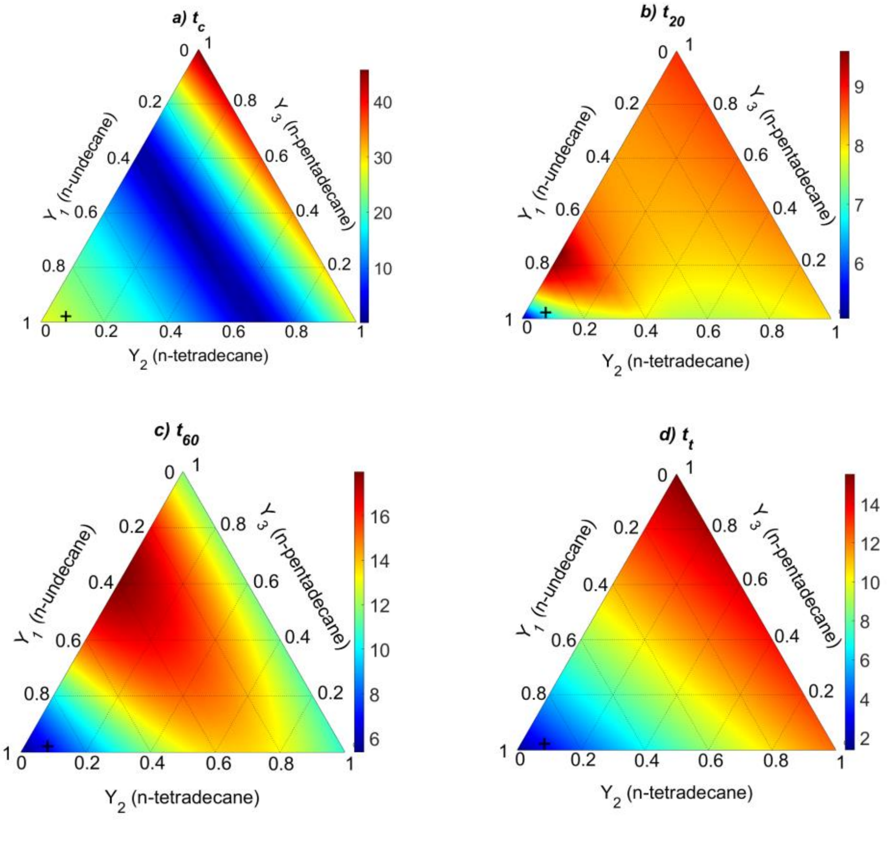

Figure 6.7, *Errors (%) in the prediction of diesel droplet evaporation metrics as a function of the surrogate composition. The black cross marks the optimal point.*

Even though all evaporation metrics are affected by the surrogate composition, the influence of surrogate composition is different for the various metrics. For example, t_{20} and t_c display, respectively, the lowest and highest sensitivity with respect to composition. In the iterative process for finding the optimal mass fraction, the GA converged to the following values for the weight factors: 0.63, 0.70, 0.34 and 0.36 for t_{20}, t_{60}, t_c and t_t, respectively. Thus, all the evaporation metrics significantly contributed to the calculation of the global objective function.

The evaporation characteristics of the selected ternary surrogate is compared in Figure 6.8 with the target diesel fuel as well as with three other different diesel surrogate mixtures proposed in the literature. Two of them are single compounds, namely n-dodecane and n-tetradecane, which were employed in previous works to emulate the evaporation behavior of diesel ((Kryukov et al., 2004) and (Ra & Reitz, 2009), respectively). The third one is a four-component blend (S4), which is proposed by Yi et al. (2021) also to capture the evaporation characteristics of diesel, being composed of n-heptane (C_7, mass fraction 10%), n-dodecane (C_{12}, 26%), n-hexadecane (C_{16}, 22%) and n-icosane (C_{20}, 42%). Figure 6.8 shows the temporal evolution of the droplet diameter squared calculated with the droplet evaporation model for these four surrogates, along with the experimental curve obtained at the DCF for diesel droplets.

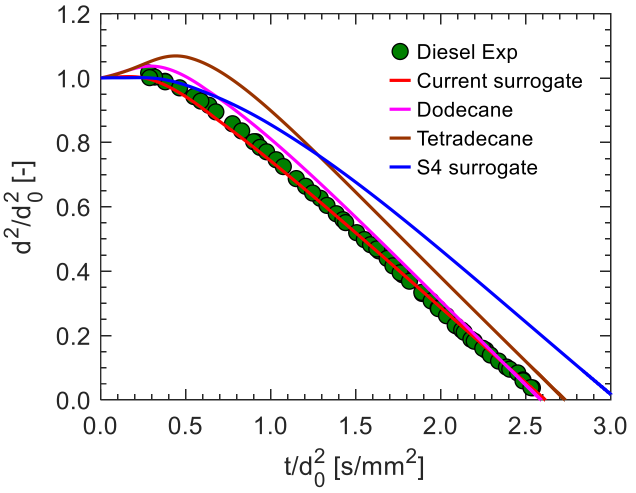

Figure 6.8, Predicted temporal evolution of droplet diameter squared for different surrogates and the experimental curve obtained at the DCF for diesel.

The two pure compounds display quite different evaporation behaviors with respect to the diesel fuel tested in this chapter. Namely, adopting C_{14} and C_{12} as surrogates would lead to a significant over-prediction in both heat-up time and a steady evaporation rate. The S4 blend vaporizes noticeably more slowly than diesel, with a shorter heat-up time and a considerably lower steady evaporation rate when compared to the monocomponent surrogates. Finally, the current surrogate matches very well the whole diesel evaporation curve, with a slightly faster evaporation at the onset of the droplet vaporization and a somewhat smaller *K* when compared to the experimental curve. This validation exercise shows that the 3-component surrogate designed following the systematic procedure proposed in this chapter leads to the best agreement among the proposed surrogate mixtures in matching the experimental droplet evaporation curve.

Table 6.3 quantifies and compares the target evaporation metrics as well as the relative errors for each surrogate mixture considered in Figure 6.8. Despite the fact that the evaporation rate is not considered for the formulation of the optimal mixture (since it is directly related to t_{20}), its addition is deemed interesting for validation purposes due to its extensive use in the droplet evaporation literature. The last row of Table 6.3 shows the root mean square of the relative error in predicting the five evaporation metrics for each surrogate.

Table 6.3, Experimental and predicted evaporation metrics for different diesel surrogates, along with the relative deviations found between surrogates and the target fuel.

	Experiment at DCF	Current surrogate	S4 surrogate	Dodecane	Tetradecane
t_t	2.53	2.61(+3.1%)	3.03(+19.7%)	2.59(+2.3%)	2.73(+7.9%)
t_c	0.33	0.26(-21.2%)	0.30(-9.1%)	0.51(+54.5%)	0.76(+129%)
t_{20}	0.82	0.86(-4.8%)	0.90(+9.7%)	0.77(-6.1%)	0.76(-7.3%)
t_{60}	1.01	1.06(+4.9%)	1.39(+37.6%)	0.92(-8.9%)	0.82(-18.8%)
k_{evp}	0.49	0.46(-6.1%)	0.44(-10.2%)	0.52(+6.1%)	0.53(+8.1%)
t_t	2.53	2.61(+3.1%)	3.03(+19.7%)	2.59(+2.3%)	2.73(+7.9%)
RMSRE[a]	-	10.40%	20.4%	25.00%	58.60%

[a] $RMSRE = \sqrt{\frac{1}{n}\sum_{i=1}^{n=5}\left(\left(mtr_i^{exp} - mtr_i^{mdl}\right)/mtr_i^{exp}\right)^2}$

The diesel surrogate defined in this section acceptably reproduces the experimental behavior with errors in t_t, t_{20}, and t_{60} of 3.1%, -4.8%, and 4.9%, respectively. The largest deviation is obtained in the heat-up time (-21.2%), but this has a limited influence on the global result because it only accounts for a small fraction of the total evaporation time. The relatively fast heat-up process (i.e., short t_c) is thought to be precisely the main reason for the larger deviation found for this metric, since the experimental uncertainty is amplified when expressed in relative terms, although with little impact on the total evaporation time. Overall, the surrogate proposed in this chapter achieved the best performance in matching the experimental evaporation curve of diesel droplet with RMSRE=10.4%.

According to these results, both mono-component surrogates significantly overestimate heat-up times (errors of 54.5% and 129% for n-dodecane and n- tetradecane, respectively) as well as the degree of the initial droplet swelling (see Figure 6.8). Between the two multicomponent surrogates, S4 shows a better performance in predicting the heat-up time. However, it significantly underestimates the quasi-steady evaporation rate, leading to a global error RMSRE, approximately double than that calculated for the proposed surrogate. It is speculated that, since the S4 blend was designed and validated at ambient temperatures between 688 K to 1023 K, it cannot accurately match the evaporation curve at a significantly higher temperature (~1730 K).

The performance of both monocomponent surrogates, C_{12} and C_{14}, is clearly worse than the other 3- and 4-component blends compared in Figure 6.8 and Table 6.3. This is not surprising, since practical fuels like diesel are markedly multicomponent, so that their evaporation behavior is dominated by different compounds along the time and, in particular, in the initial and final stages. Moreover, from a mathematical point of view, multicomponent blends offer more degrees of freedom that greatly facilitate matching different features of the evaporation curve. The radar chart in Figure 6. 9 depicts the evaporation metrics predicted for the current surrogate and the experimental results extracted for the target diesel fuel at DCF.

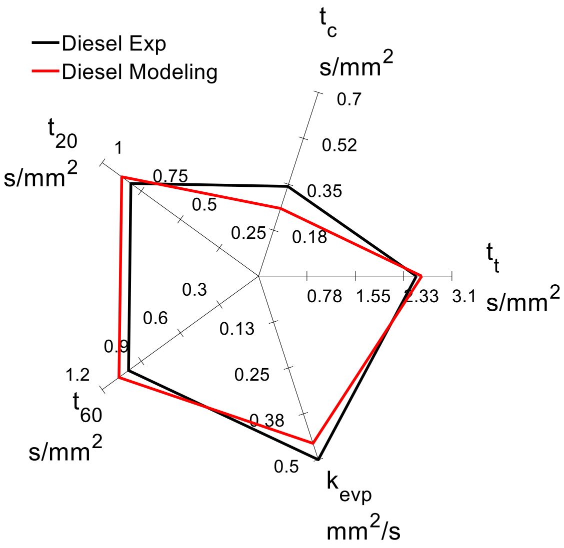

Figure 6.9, Comparison among the predicted metrics for the surrogate and experimental data for Jet A.

To give further insight into the multicomponent behavior, Figure 6.10 shows the mass fraction distribution of the lightest (C_{11}) and heaviest component (C_{15}) within the liquid droplet for the current diesel surrogate. These radial profiles are normalized by the instantaneous droplet radius (a). As it is shown, during the initial stage ($t/d_0^2 = 0$ up to $t/d_0^2 = 0.4$ s/mm^2), there are practically no compositional gradients within the liquid for both C_{11} and C_{15}. In other words, in this very short time interval, the vaporization behavior is close to a batch distillation scenario. However, the slow diffusion of species within the liquid limits the arrival of the lighter species close to the surface, where they are being quickly removed. As a result of these limitations in mass transport, significant compositional gradients appear near the surface, as it can be seen through time steps $t/d_0^2 = 2.20$ s/mm^2 and $t/d_0^2 = 2.65$ s/mm^2. This behavior displays significant differences when compared to the aforementioned batch distillation scenario, predominant in low temperature applications. In that case, there would be no spatial composition gradients at any point of the droplet evaporation lifespan. In this regard, although the distillation curve data have been frequently employed as a target property to formulate physical surrogates (Chen et al., 2016; Elwardany et al., 2016; Kim & Violi, 2021; Luo & Liu, 2021; Su & Chen, 2015), it mainly represents the fuel evaporation characteristics at low temperature. In other words, a surrogate formulated to match the distillation curve would probably emulate the evaporation behaviors of the target fuel in a correct manner under low temperature conditions, but it might not match its evaporative characteristics under high temperature conditions such as those typically occurring in combustion applications.

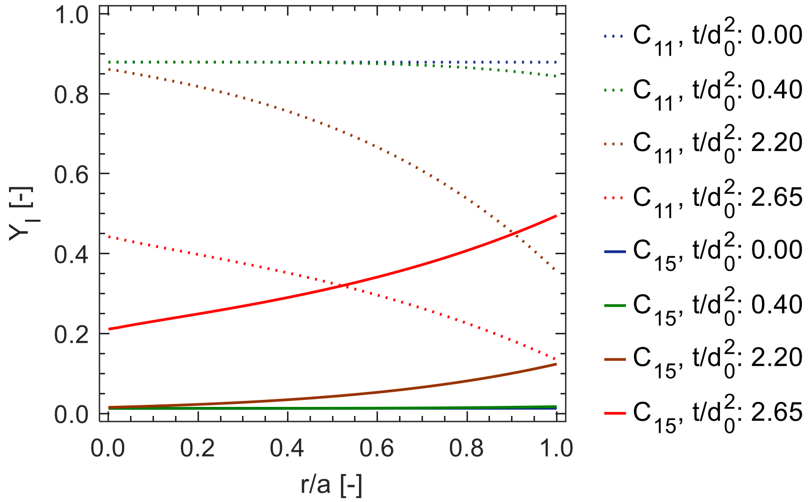

Figure 6.10, Radial profiles of liquid mass fraction of the lightest and heaviest components in diesel's surrogate mixture at different time instants.

6.5.2 Jet A

The application of the systematic procedure proposed in section 6.4 to the case of Jet A fuel yielded a surrogate blend composed of n-undecane (C_{11}), n-tridecane (C_{13}) and n-tetradecane (C_{14}), which were the compounds that minimized the similarity indexes described in Eq. (6.2). The optimal mixture for Jet A is composed of 84.3% n-undecane, 11.3% n-tridecane and 4.4% n-tetradecane. Figure 6.11 shows the variation of the predicted errors for different mass fraction permutations in the surrogate mixture. Similarly to the case of diesel, t_c shows the highest sensitivity toward changes in composition. On the other hand, t_{20} and t_{60} are much less affected by mass fractions permutations. It is noteworthy that the patterns in the ternary error diagrams calculated for Jet A are very similar to those shown in Figure 6.7 for diesel. It is speculated that this can be due to the similarity between the evaporation characteristics of both target fuels. In fact, the surrogate design procedure resulted in very close palette compounds selected for both target fuels (C_{11}, C_{13}, C_{14} for Jet A and C_{11}, C_{14}, C_{15} for diesel).

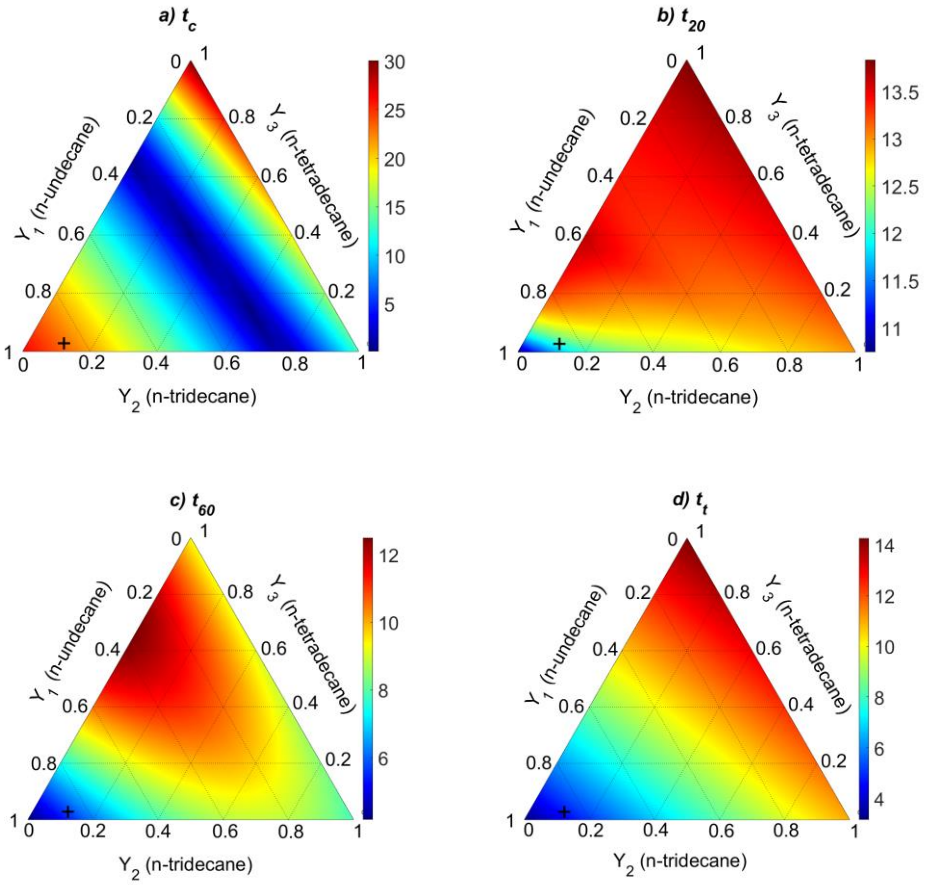

Figure 6.11, Errors (%) in the prediction of Jet A droplet evaporation metrics as a function of the surrogate composition. The black cross marks the optimal point.

In the search for the optimal surrogate for both Jet A and diesel, the final mixture for three of the metrics (t_{20}, t_{60}, t_t) appears to be located close to the pure lightest compound C_{11}. However, neat C_{11} would yield a high error in terms of t_c, so that additional compounds are required to reproduce the actual evaporation behavior of Jet A. There are a set of quite heavier mixtures (approximately composed of 20-40% C_{11} in Figure 6.11) that would minimize the prediction error in t_c, but tend to increase deviations in other metrics. Finally, the emulation of t_{20}, t_{60} and t_t outweighs the matching of t_c, resulting in surrogate mixtures very rich in C_{11} (88% for diesel and 84% for Jet A).

Figure 6.12 shows the predicted temporal evolution of droplet diameter squared for the current surrogate, along with the experimental data obtained for Jet A at the DCF. Comparing both, the evaporation model is able to predict the t_t and t_{60} of Jet A with errors of 5% and 6%, respectively. However, the errors in K_{evp} and t_c are somewhat larger (10.92% and 22.4%, respectively). Overall, the RMSRE of the surrogate with respect to the experimental evaporation curve of Jet A is calculated as 12.9%. Comparing the droplet diameter evolution of Jet A (Figure 6.12) and diesel (Figure 6.8), it is worth noting that shorter heat-up times are predicted for both surrogate models, with slightly lower steady evaporation rates when compared to the experimental results. For the case of Jet A, this results in a somewhat longer predicted evaporation time when compared to the experiment, whereas the diesel surrogate achieves a quite good agreement in terms of t_t. The radar chart in Figure 6.13 graphically compares the evaporation metrics predicted for the current surrogate and the experimental results extracted for Jet A fuel.

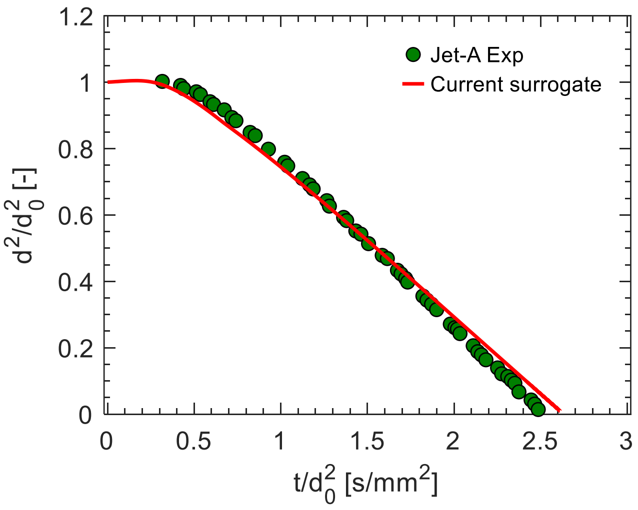

Figure 6.12, Predicted temporal evolution of droplet diameter squared for surrogate and experimental curve obtained at the DCF for Jet A.

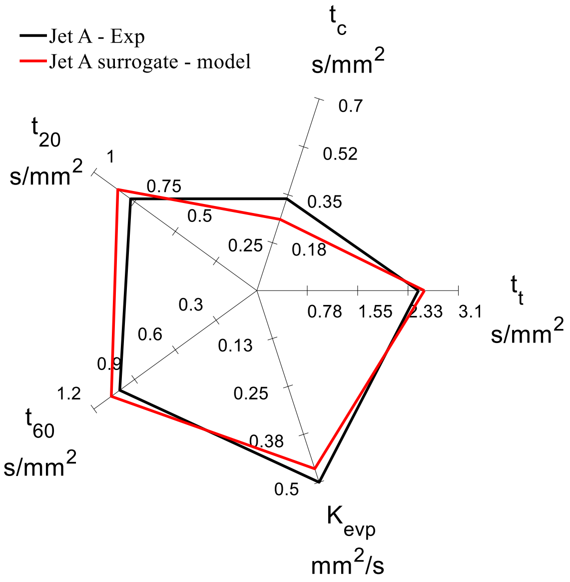

Figure 6.13, Comparison among the predicted metrics for the surrogate and experimental data for Jet A.

6.5.3 Heating Oil

The merit set of surrogate components selected for the case of heating oil (HO) are n-tetradecane (C_{14}), n-heptadecane (C_{17}) and n-icosane (C_{20}), being the optimum blend for HO composed of 21.8% C_{14}, 76.1% C_{17} and 2.1% C_{20}. As it can be noted, the HO surrogate components are notably heavier in terms of molecular mass in comparison with those of diesel and Jet A. This is consistent with the average molecular mass and standard density reported in Table 6.1 for these three real fuels. Figure 6.14 shows the predicted errors for each evaporation metric for the different surrogate compositions.

Due to the tangible differences in the surrogate palette for HO in comparison with those of diesel and Jet A, the patterns for variations in the predicted errors for HO are significantly different. For instance, the lowest errors for t_c occurs for mixtures with approximately 18~28% of the lightest compound C_{14}, the rest (82~72%) consisting of heavier compounds, C_{17} and C_{20}. According to the error diagrams, t_t and t_{60} have the lowest sensitivity toward changes in mass fractions in comparison with t_c and t_{20}.

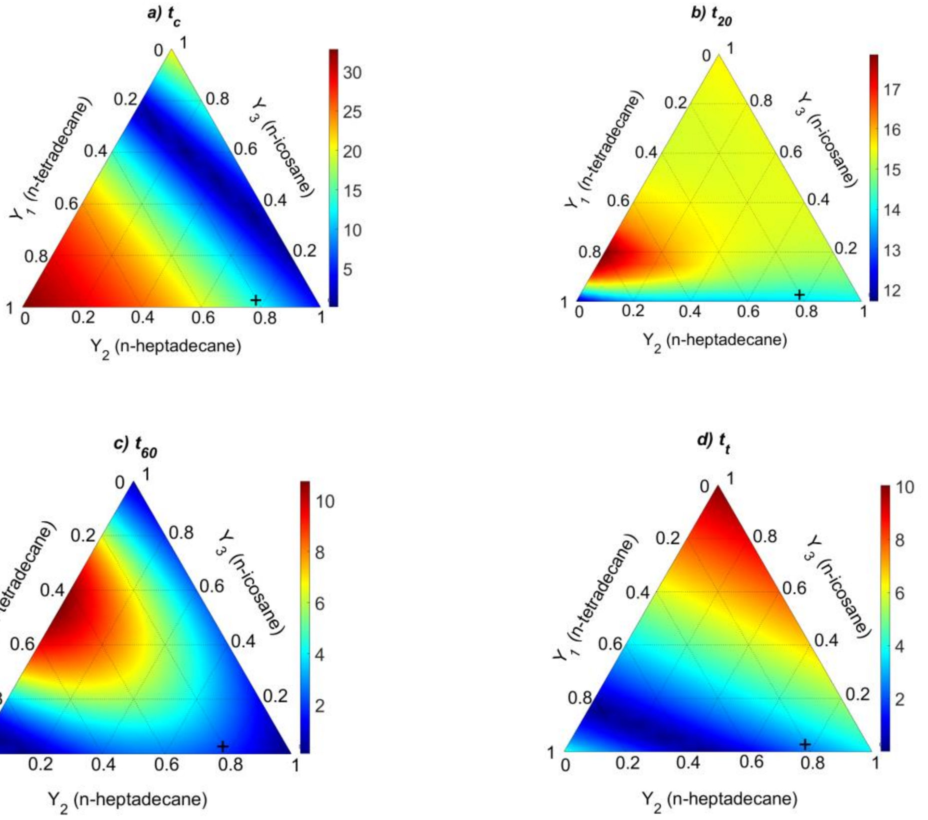

Figure 6.14, Errors (%) in the prediction of heating oil droplet evaporation metrics as a function of the surrogate composition. The black cross marks the optimal point

The model results for this surrogate along with experimental data for HO are presented in Figure 6.15. The metrics obtained from the predicted evaporation curve for the surrogate are compared to those derived from measurements in Figure 6.16. Similarly to the results already discussed for diesel and Jet A, the designed blend shows a shorter heat-up time and a slightly longer evaporation time. The predicted errors for t_c, K_{evp} and t_t are calculated as 13.1%, 12.3% and 3.3%, respectively. For the case of t_{20} and t_{60}, the deviations with respect to the experimental observations are estimated as 14.0% and 2.1%, respectively. Lastly, the RMSRE of the current surrogate for matching the experimental evaporation curve of HO is calculated as 10.3%, quite alike to those obtained for diesel (10.4%) and Jet A (12.9%).

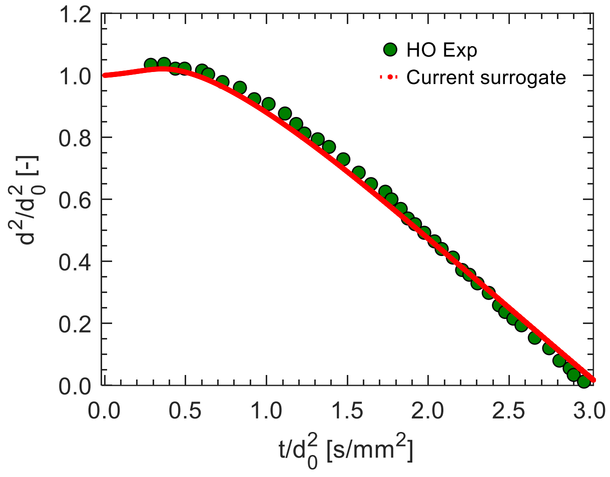

Figure 6.15, Predicted temporal evolution of droplet diameter squared for surrogate and experimental curve obtained at the DCF for heating oil.

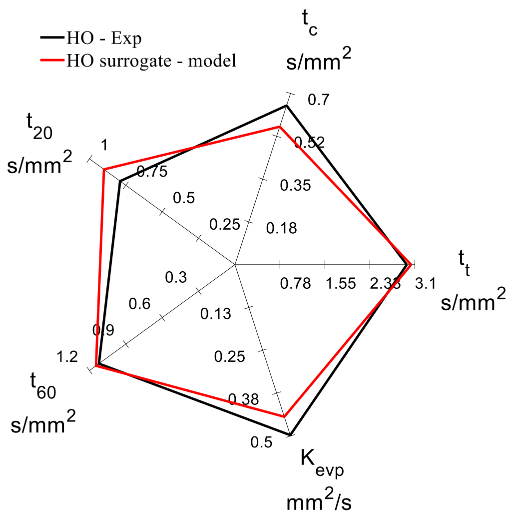

Figure 6.16, Comparison among the predicted metrics for the surrogate and the experimental data for heating oil.

7. Nanofuel droplet evaporation

In line with prior discussions in Chapter 1, nanoparticles can significantly influence the evaporation and combustion behaviors of fuel droplets. Some works report that their addition enhance droplet evaporation, leading to improved fuel-air mixing, reduced emissions and enhanced combustion efficiency (El-Seesy et al., 2017; Khond & Kriplani, 2016). However, the effects of nanoparticles on droplet evaporation rates can be quite contrasting, depending on specific conditions (NPs type, concentration, environment temperature, etc.). For instance, at moderate temperatures, nanoparticles have been reported to slow down evaporation. This is thought to be related to the formation of a solid shell around the droplet during evaporation. Research by Javed et al. (2013a; 2014) shows that nanoparticles can agglomerate and form a thick shell around the heptane droplet leading to a reduction in thermal diffusion and evaporation rates.

Furthermore, preceding research endeavors have frequently centered their investigations on conducting experiments under relatively low environmental temperatures, specifically those falling below the threshold of 1000 K. In the research conducted by Javed et al. (2013b) and Wang et al. (2019), findings have occasionally been less definitive, attributable to the intricate task of isolating the influence of nanoparticles on droplet evaporation. This complexity is especially pronounced in the examination of nanofuels' behavior under certain experimental parameters, like large droplets suspended on thick fibers where the effects of natural convection and fiber conduction can also influence droplet evaporation dynamics. This ambiguity in findings has consequently posed a challenge in obtaining a comprehensive understanding of the impact exerted by nanoparticles on the dynamics of droplet evaporation.

Hence, in order to analyze the impacts of nanoparticle addition, this chapter summarizes an exploratory work that seeks to expand research into nanofuel droplet evaporation at significantly higher, flame-like temperatures. Particular emphasis is placed on maintaining precise control over the experimental parameters, testing small diesel droplets (d_0 =500μm) suspended on fine low-conductivity fibers (15μm SiC). Regarding the particles tested, cerium oxide (CeO_2), aluminum oxide (Al_2O_3), and carbon nanotubes (CNT) are chosen because of their relevance, as detailed in the Introduction.

7.1 Nanofuel preparation

The preparation of a nanofuel involves a meticulous process incorporating three distinct nanoparticles: ceria (CeO_2), carbon nanotubes (CNT), and alumina (Al_2O_3) to a base liquid fuel (diesel), ensuring their homogeneous dispersion. The nanoparticles display a nominal size of 5-20 nm (CNT), <25 nm (CeO_2) and <50 nm (Al_2O_3), as reported by the manufacturer.

The preparation process begins with accurately weighing both the selected nanoparticle and the base fuel (diesel) on an analytical scale (Sartorius CP225D, repeatability ±20 μg). Based on the literature review summarized in the Introduction, the concentration of nanoparticles has been fixed at 0.5% (wt.). This proportion is expected to yield changes in the droplet vaporization process while avoiding the addition of an unrealistically high amount of nanoparticles. Thus, the nanoparticles and the base fuel are transferred in this proportion into a beaker, where they undergo an intensive mixing process.

This is achieved using a high-speed rotary device operating at speeds ranging from 15,000 to 20,000 rpm for a duration of six minutes. This initial high-shear mixing ensures disintegrating the big-sized initial agglomerates into much smaller particles (ideally, reaching the nominal sizes reported by the manufacturer). After this first mixing stage, the nanofuel is subjected to ultrasonication. This process involves placing the mixture in an ultrasonic bath that generates sound waves at 50 kHz for a period of half an hour. Ultrasonication has been found to be a critical step, as it employs high-frequency sound waves to agitate particles in the fuel, promoting an even finer dispersion of the nanoparticles.

Following ultrasonication, the next step involves the addition of a surfactant that avoids the coalescence of particles. To this end, sorbitan monooleate (Span 80) at a 0.5% (wt.) concentration was chosen after a specific parametric study where different surfactants combinations were tested. The precise amount of Span is carefully weighed and then added to the beaker. Once again, the high-shear rotatory device is employed for mixing, ensuring that the surfactant is evenly distributed throughout the mixture over another six-minute period. After that, once again the sample is ultrasonicated for a period of half an hour.

The final step in the nanofuel preparation process is to assess the stability of the mixture. This is done through visual inspection over a period of several hours, closely observing for any signs of sedimentation. For the cases of ceria and alumina, the nanofuel mixture was found to be very stable, without any evidence of solids sedimentation in several hours. However, for the case of CNT, it is noteworthy that the stability of the nanofuel blend persisted for a duration of approximately thirty minutes, during which tiny micron-sized could be detected. Fresh samples were tested immediately after their preparation at the SDF setup under pure evaporation conditions (0% O_2 in coflow) and using a pair of 15 μm silicon carbide fibers to suspend the droplet.

7.2 Experimental results

As detailed before, three distinct mixtures of diesel fuel and nanoparticles (NPs) were prepared for the purpose of conducting experimental measurements. These mixtures consisted of diesel fuel with the addition of 0.5% wt. of alumina, 0.5% wt. of ceria and 0.5% wt. of carbon nanotubes. To ensure the reliability and consistency of the experimental measurements, the experimental procedure was repeated multiple times using droplets with initial sizes close to 500 µm. Figure 7.1 illustrates the temporal evolution of the droplet diameter squared for the cases of pure diesel fuel and the various nanofuels. For the case of pure diesel, it is evident that the evaporation process exhibits a consistent behavior in accordance with the d^2-law pattern, with a smooth evaporation which, after an initial heating-up transient, converges to a quite linear decrease of the droplet diameter squared with time (i.e., constant evaporation rate). In contrast, the incorporation of nanoparticles into the diesel droplets induces alterations to the evaporation profile, notably characterized by instances where the droplet increases abruptly its size. This increase in size can only be due to the formation of bubbles within the droplet. The sudden formation of bubbles, which are retained inside the liquid, increase the droplet size without noticeably affecting the evaporation rate, as it occurs in Figure 7.1 (particularly for the case of Alumina and Ceria nanoblends). Comparing the total consumption time of pure diesel (t_t = 2.5 s/mm^2) with nanofuels reveals a subtle reduction in this total evaporation time for nano-diesel droplets: 2% for the case of diesel + alumina, 7.7% for diesel + CNT and 5.2% for diesel + ceria.

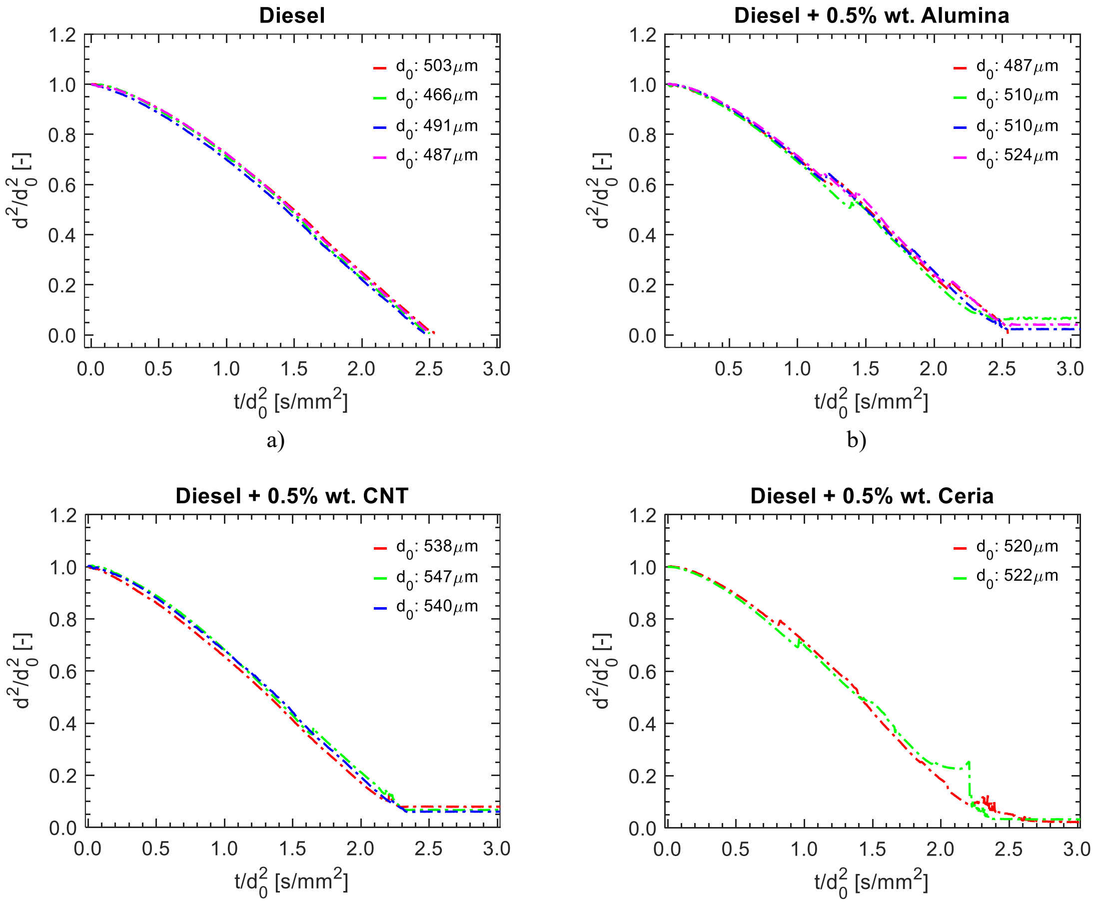

a) b) c) d)

Figure 7.1, Evolution of the droplet diameter squared of different diesel nanofuels.

The general evaporation process of the nanofuel droplets displayed in Figure 7.1 can be delineated into three distinct phases. Firstly, there is an initial phase referred to as the ’smooth evaporation sequence’, during which the concentration of nanoparticles within the liquid bulk is low and the evaporation behavior remains smooth and similar to that of pure diesel, as depicted in Figure 7.2.a. However, the presence of the solid nanoparticles within the droplet is found to slightly accelerate this initial heating transient, as it will be detailed further on. This is ascribed to the effect of radiation heat absorption by nanoparticles (Gan & Qiao, 2012), as well as to the enhancement of liquid thermal conductivity due to these solids (Aboalhamayie et al., 2019). Secondly, there is the subsequent stage named as ’fluctuating droplet evaporation’, characterized by the intermittent occurrence of abrupt changes in the droplet size, which are clearly related to the inception of bubbles (as illustrated by Figure 7.2.b and 7.2.c, respectively). The onset of this phenomenon is clearly related to the inclusion of the nanoparticle additives, which may act as a heterogeneous nucleation site promoting the formation of vapor bubbles (Mei et al., 2023). The sudden ejection of vapor pockets can even cause the expelling of small fragments of liquid (child droplets), as it can be noticed in Figure 7.2.b. Lastly, the third stage occurs when the droplet is close to complete depletion. During this phase, the concentration of NPs within the liquid bulk increases, causing the droplet to lose its spherical shape and undergo a gelation process (Lai & Pan, 2023) that significantly affects its morphology. Ultimately, this leads to a complete dry-out of fuel droplet and the deposition of solid particles at the suspension site on the fibers (see Figure 7.2.d). This is depicted as the horizontal line at the end of evaporation curves in Figure 7.1.

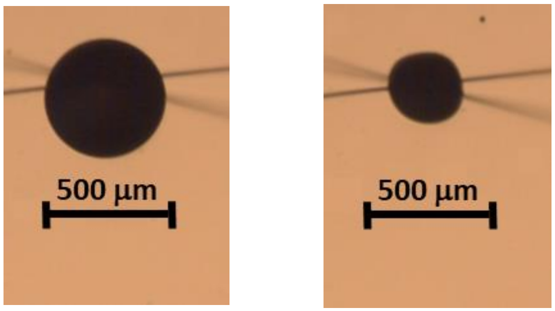

a) smooth evaporation b) child droplet expulsion

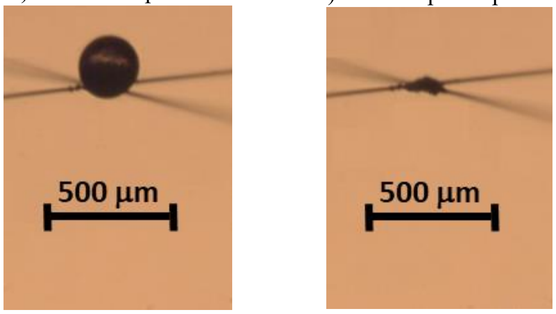

c) droplet swelling d) solid particle deposits

Figure 7.2, Different sequences of nanofuel droplet evaporation on suspension fiber (the background is removed in the images).

The aforementioned phenomena add more complexity to the process of droplet evaporation, causing also clear variations between experimental runs for a given fuel. The occurrence of a bubbling event is thought to be a stochastic phenomenon, as proven by the variability shown in Figure 7.1 for the different nanofuels. Due to this variability, and in order to rigorously assess the influence of nanoparticle additives on the evaporation behavior of diesel, a set of quantitative metrics are introduced for this evaluation. Hence, the evaporation curve is discretized into eight distinct metrics, as illustrated in Figure 7.3. These metrics are denoted as t_{90}, t_{80}, t_{70}, t_{60}, t_{50}, t_{40}, t_{30} and t_{20}. The definition of these metrics helps to assess the effects of nanoparticle addition on the different intervals of the droplet evaporation sequence.

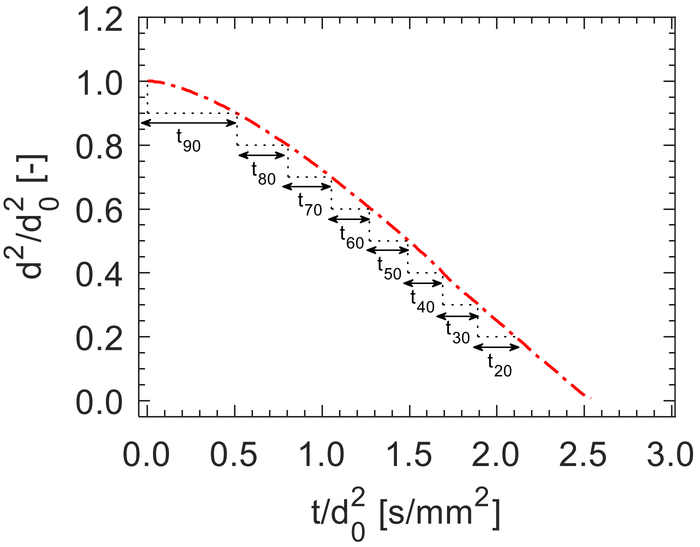

Figure 7.3, Evaporation metrics defined for characterizing the evaporation of nanofuel droplets.

These defined metrics are then calculated for the droplet evaporation curves of pure diesel and the three nanofuels displayed in Figure 7.1. Since multiple experimental instances were conducted for each experimental condition, the mean and standard deviation for each metric were calculated, being the computed values depicted in Figure 7.4. It should be noted that these evaporation metrics are only calculated for the evaporation curve region with a smooth and undisturbed vaporization. Consequently, the absence of some metrics within the subsequent sub-figures indicates instances of puffing and erratic behaviors for the evaporation curves in these intervals. The evaluation of evaporation metrics for these periods is excluded for this exploratory analysis, which is rather focused on the initial stages where no bubbles are formed (allowing therefore for a direct assessment of the vaporization rate based on the droplet size).

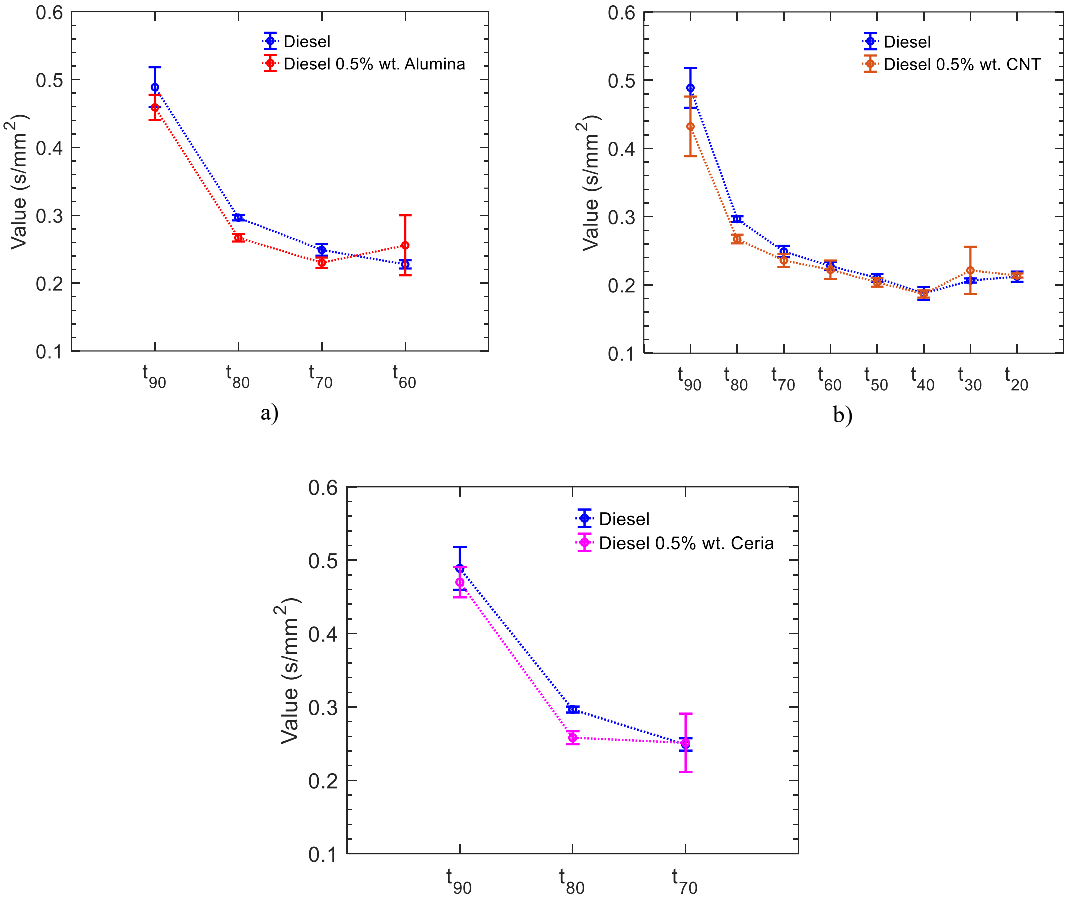

a) b)

c)

Figure 7.4, Evaporation metrics calculated for diesel and different nanofuels (average ± standard deviation).

According to Figure 7.4, nanoparticles appear to impact the process of droplet evaporation, especially during the initial phases of the droplet's lifespan. These early stages of droplet evaporation are described by metrics such as t_{90}, t_{80} and t_{70}, whose values are noticeably reduced when NPs are added to diesel, indicating an enhanced rate of evaporation in this interval. This observation aligns with findings in the existing literature, which have demonstrated that the enhancement of radiation absorption (Gan & Qiao, 2012) and thermal conductivity (Aboalhamayie et al., 2019) are the two main driving factors accelerating the droplet evaporation.

For the case of diesel + CNT, the evaporation process is found to be essentially smooth until the droplet depletion point, allowing for the extraction of the whole set of metrics. The metrics describing the initial region (t_{90}, t_{80}) are reduced for this nanofuel in comparison with pure diesel, obtaining essentially the same values for the rest of metrics. This convergence towards the values of diesel points to CNT impacting primarily the initial heat-up transient, where the liquid thermal conductivity plays a key role in distributing the heat input absorbed at the droplet surface. As the droplet increases its temperature, it eventually transitions into the quasi-steady phase where the liquid temperature would remain constant (for a monocomponent case), losing the liquid thermal conductivity its role in enhancing the evaporation process. Furthermore, since the impact of thermal radiation absorption is increased with the droplet size (see section 5.2), this mechanism is also expected to have a larger effect in this initial stage, decreasing its relevance for the smaller droplets evaluated in the quasi-steady region. The experiments performed on the other two nanofuels (diesel + alumina/ceria) displayed clear instances of bubbling, as shown in Figure 7.4. Therefore, only the initial metrics related to the heat-up transient could be extracted, yielding analogous results to those already discussed for diesel + CNT (i.e., noticeable reduction in t_{90} and t_{80}, converging afterwards toward the values obtained for pure diesel).

In summary, even if this exploratory work had a limited scope due to time constraints, the extracted tendencies are thought to be clear and in accordance with some previous studies using lower temperature conditions. More work is planned to extend this initial assessment, namely by performing parametric studies addressing additional relevant variables, such as the nanoparticles concentration, the oxygen level (i.e., extending it to droplet combustion conditions), or the impact of NPs addition to different base fuels. Additional studies aiming to gain insight into relevant phenomena taking place in nanofuel evaporation (bubbling, gelation, formation of nanoparticles shells, etc.) are also planned as a continuation of this exploratory work.

7.3 Surrogate formulation for nanofuel droplet evaporation

The surrogate formulation method described in Chapter 6 can be readily used to capture the high-temperature evaporation characteristics of any liquid. However, the inception of bubbles for some nanofuels (Figure 7.1) hinders its direct applications, since it relies on the premise of a droplet containing only liquid (so that any change in the droplet size is either due to evaporation or to a change in liquid density). Therefore, the method has been slightly modified, so that the target evaporation metrics are only those corresponding to the smooth evaporation region. That is, for pure diesel and diesel + CNT the whole set of metrics displayed in Figure 7.3 has been targeted. However, for diesel + alumina only t_{90}, t_{80}, t_{70} and t_{60} are employed, whereas the earlier onset of bubbles for diesel + ceria restricts the available metrics to t_{90}, t_{80} and t_{70}.

Applying the surrogate formulation approach on each set of experimental measurements for pure diesel and the different nanofuels results in the following composition for the optimized surrogate blends:

1. Pure diesel: 82.6% n-undecane (C_{11}) + 7.0% n-tetradecane (C_{14}) + 10.4% n-pentadecane (C_{15}).
2. Diesel + 0.5% alumina: 85.9% C_{11} + 11.1% C_{14} + 2.9% C_{15}.
3. Diesel + 0.5% CNT: 90.0% C_{11} + 5.0% n-C_{14} + 5.0% C_{15}.
4. Diesel + 0.5% ceria: 86.2% C_{11} + 7.2% C_{14} + 6.6% C_{15}.

Hereafter, comparing the mass composition of the different surrogate mixtures for nanofuels, it becomes clear that the mass fraction of the most volatile compound within the palette (C_{11}) increases in the surrogates designed for nanofuels when compared to diesel, while the summation of the other two less volatile compounds (C_{14} and C_{15}) decrease. This trend is consistent with the already discussed lower values of t_{90} and t_{80} for nanofuels in comparison with diesel, and points to the ability of the surrogate formulation method to capture these differences, generating more volatile blends for the nanofuels than for the pure diesel.

Figure 7.4, displays a comparison of the experiments on the different target fuels alongside with their predicted evaporation curves (as determined by the representative surrogate blends calculated by the model). As discussed before, during the surrogate formulation phase a particular subset of evaporation metrics (comprising intervals characterized by smooth evaporation) was targeted for each nanofuel. Consequently, the modeling evaporation curves are only depicted within these designated target intervals, specific for each target fuel.

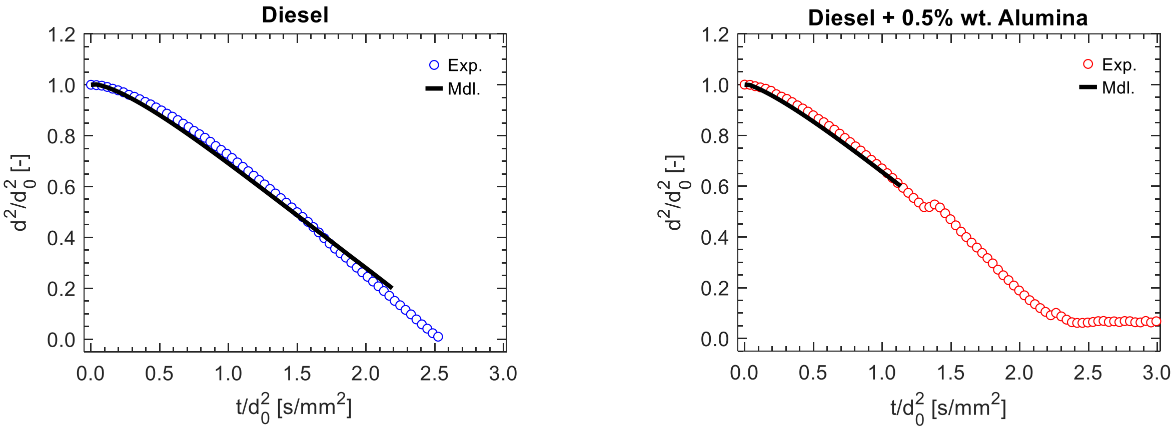

a) Pure diesel experiment and simulation for its surrogate (82.6% C_{11} + 7.0% C_{14} + 10.4% C_{15})

b) Diesel + 0.5% alumina experiment and simulation for its surrogate (85.9% C_{11} + 11.1% C_{14} + 2.9% C_{15})

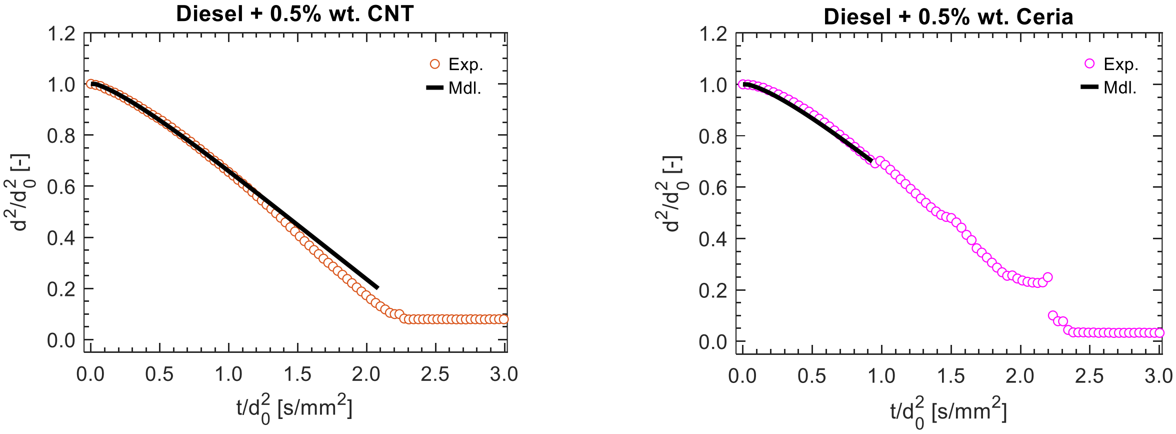

d) Diesel + 0.5% CNT experiment and simulation for its surrogate (90.0% C_{11} + 5.0% C_{14} + 5.0% C_{15})

c) Diesel + 0.5% ceria experiment and simulation for its surrogate (86.2% C_{11} + 7.2% C_{14} + 6.6% C_{15})

Figure 7.5, Predicted temporal evolution of the droplet diameter squared for the surrogate mixtures obtained for diesel and nanofuels, along with the experimental curves obtained at the SDF.

The overall agreement between the modeling results for the surrogate and the experimental data for the corresponding target fuel is found to be good, although the model tends to overestimate evaporation during the first stages. This overestimation occurs for the case of diesel, diesel + alumina and also diesel + ceria, whereas for diesel + CNT the emulation of this first transient phase is significantly improved. On the contrary, the two cases where the whole evaporation curve is targeted (diesel, diesel + CNT) display a noticeable underestimation of the evaporation rate for the final, quasi-steady phase. It is speculated that these shortcomings in the emulation of the target evaporation curve can be related to the lack of enough palette compounds, whose number may need to be increased to achieve a closer match.

The following Figure 7.6 shows the comparison among the evaporation metrics calculated from the experimental measurements and the predicted values for the surrogate blends. As noted before, the designed surrogates could acceptably predict the evaporation behaviors of the different nanofuels, especially for the case of diesel + CNT, where a remarkable agreement is reached in terms of t_{90} and t_{80}, with higher deviations in the quasi-steady phase. For the other two nanofuels, the aforementioned overestimation of the evaporation rate during the first stages is translated into shorter values of t_{90} for the surrogate, with a better emulation of t_{80}. As discussed before, the limited number of components in the surrogate palette (3 compounds) is ascribed as the main cause for these deviations. Future work is planned to extend this number, so that a closer agreement between surrogates and target fuels can be reached.

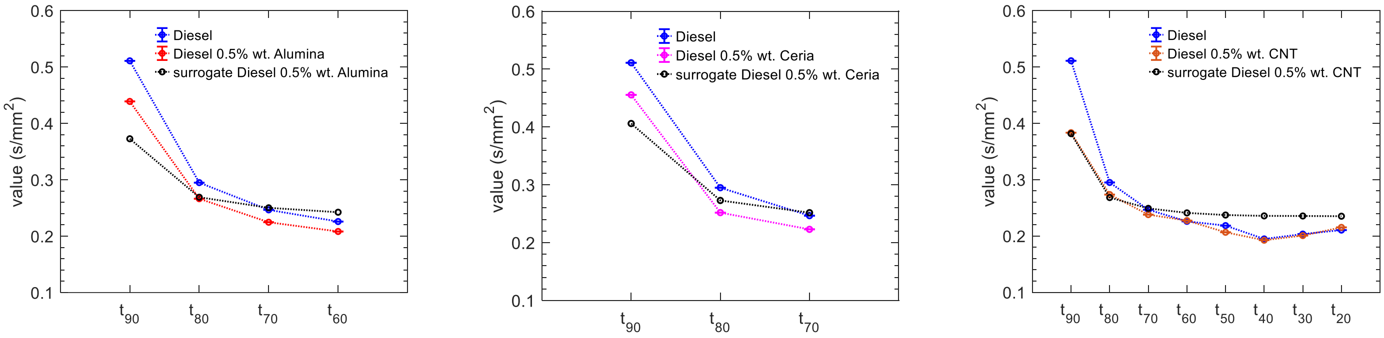

a) Diesel + Alumina *b) Diesel + Ceria* *c) Diesel + CNT*

Figure 7.6, Target metrics obtained from experimental measurements for pure diesel and nanofuels, compared to the predicted values for the corresponding surrogate mixtures.

For the cases of pure diesel and diesel + CNT in which the whole evaporation curves are considered for model validation, the root mean square of relative error (RMSRE) in predictions are calculated as 13.9% and 12.0%, for diesel and diesel + CNT, respectively. As for the cases of diesel + Alumina and diesel + Ceria, the surrogate models could predict the initial sequences of evaporation curve with RMSRE of 12.5% and 10.8%, respectively.

Besides the quantitative data specifically obtained for the nanofuels considered, this analysis is also intended as another example of application of the surrogate formulation procedure described in Chapter 6. The results demonstrate the versatility and generality of the method, since it can be readily adapted for new fuels and target properties, avoiding the need for *ad-hoc*, expert rules both for the selection of palette compounds or the identification of optimal composition.

8. Conclusions

8.1 Summary and concluding remarks

In this dissertation, a multifaceted approach combining experimental and modeling techniques has been employed to investigate the dynamics of fuel droplet evaporation at high-temperature environments. The motivation behind this approach lies in the necessity to gain a deeper understanding of the evaporation process, particularly in scenarios relevant to practical applications such as those found in liquid fuel combustion units (e.g., boilers or furnaces).

In doing so, two different experimental setups have been used over the course of this dissertation to characterize isolated fuel droplet vaporization at flame-like conditions, namely: the Droplet Combustion Facility (DCF) and the Suspended Droplet Facility (SDF). The former was previously developed according to the free-falling droplet framework, providing test conditions with unsupported, small-sized droplets (~150 μm) vaporizing at high temperature (~1700 K). The latter has been developed in this PhD study according to suspended droplet approach and it features significantly larger droplets (~300-1100 μm), which in this case are anchored by different solid fibers. The SDF setup has been designed to allow for testing different gas temperatures (~700, 1000, 1336 K), being the last one used throughout this dissertation. Moreover, in both facilities it is possible to adjust the gas coflow composition, enabling a wide range of experiment conditions, from pure evaporation to conventional or oxy-fuel combustion. Despite the fact that experiments in both setups are conducted under normal gravity, the consistent presence of nearly spherical envelope flames provided compelling evidence that droplet vaporization occurs at conditions approximating spherical symmetry. A large number of experiments using a remarkably broad range of conditions have been conducted at both facilities both for pure compounds (e.g., ethanol, butanol, glycerol) and also for real fuels (diesel, kerosene, heating oil). The obtained empirical results at these facilities have the potential to serve various purposes within academic research and engineering applications. Specifically, they may be employed for comparative analyses across different types of fuels, as fuel-specific data required for the simulation of sprays in computational tools or as a means to validate models related to droplet evaporation and combustion, as it is detailed further on.

Another crucial component of this thesis involves the development and validation of theoretical models on isolated droplet vaporization, with a specific focus on practical scenarios involving high temperature environments and multicomponent fuels. This evaporation model has been developed and successfully validated, both by means of literature data and also by comparison with DCF and SDF results. Furthermore, in the context of a single droplet vaporizing within a high-temperature environment while suspended by fibers (e.g., tests conditions applied at SDF), two distinct sub-models have been developed to account for the impact of the conduction of heat through the fibers and the absorption of thermal radiation on the evaporation process. These sub-models have also been successfully validated against both existing literature data and the results obtained from SDF.

Any computational tool predicting evaporation/combustion behaviors requires not only a reliable mathematical description of the process being modelled, but also accurate values for the many physico-chemical properties involved. A specific search revealed a significant gap in the literature for this issue, even though it is acknowledged as a relevant source of error that can undermine the reliability of evaporation calculations. To address this, a local sensitivity analysis has been carried out to assess the influence of uncertainties in properties on the predictions of the validated droplet vaporization model, confirming the potentially high impact of inaccuracies in these properties on the reliability of predictions. The propagation of uncertainties from the input data towards evaporation parameters was analyzed, yielding multiplication factors of the order of one (i.e., relative uncertainties in the outputs similar to those in the inputs) for a number of properties, including specific heat, thermal conductivity or liquid density, and increased up to 3 for the boiling temperature. For the specific test case considered in this study (evaporation of diesel droplets at high temperatures), variations of up to ~90% in some evaporation metrics should be expected depending on the particular assumptions applied, among those normally considered in published works. Therefore, a correct evaluation of the properties for a given fuel appears as a key issue to achieve accurate predictions of droplet evaporation and, hence, of spray flames.

Within the context of single droplets experiments, most test rigs aim to emulate the simplified, canonical configuration where an isolated droplet is being vaporized solely by gas-liquid conduction of heat in a completely quiescent atmosphere devoid of any convection. Under these conditions, the process becomes spherico-symmetric, significantly easing modeling efforts and results interpretation. However, it is well-known that real experiments are often affected by experimental artifacts that may lead to significant deviations from this assumed ideal scenario, such as the conduction of heat through the suspension fibers, the absorption of thermal radiation or the onset of convection due to relative velocities between the droplet and the surrounding gas. The onset of these effects can be considered to be ubiquitous in most droplet evaporation experiments, and therefore, most of the published literature data on droplet evaporation is, to some degree, affected by them. A literature review identified that deviations in the droplet evaporation rate (K) can even exceed 100% due to these artifacts, as compared to the canonical case where the only heat-transfer mode is conduction through the gas-droplet interface ($\dot{Q}_{gc}$). Thus, the magnitude of these deviations should be assessed in order to allow a correct interpretation and utilization of the experimental results. To that end, a theoretical analysis has been performed, aiming to determine the relevant parameters and magnitudes of the different experimental artifacts. A dimensionless number is proposed for each artifact, based on the ratio of the heat input due to these respective additional heat-transfer modes and $\dot{Q}_{gc}$. In this manner, the fiber, radiation, and convective numbers (*FN*, *RN* and *CN*, respectively) are formulated. For moderate values of these additional heat inputs, a linear correlation is obtained, indicating that the deviation of the droplet evaporation rate from the canonical case (K/K_{can}) can be predicted based on *FN*, *RN* and *CN*. Since these dimensionless numbers can be readily calculated based on the global characteristic parameters of the problem, the impact of each experimental artifact on the droplet evaporation rate can be easily estimated.

This theoretical analysis has been validated with results from both DCF and SDF, for a remarkably wide range of test conditions, which is thought to constitute a unique database in this respect. The extracted evaporation rates display a wide variability, with K/K_{can} ranging from ~ 1.1 to ~ 2.1, depending on the size and conductivity of the support fibers used in SDF tests. In contrast, results for the DCF display much smaller deviations from the canonical evaporation rate (K/K_{can} ~ 1.03), mainly due to the fact that unsuspended and very small droplets were tested. All these experimental results, along with literature data for quite different test conditions, prove the usefulness of the proposed approach to analyze the deviations in evaporation rate due to these artifacts. Moreover, for small to moderate values of *FN*, *RN* and *CN*, the results depicted well-defined trends consistent with a superposition of the different heat transfer modes, so that the ratio K/K_{can} can be easily estimated as ~ (1+*FN*+*RN*+*CN*).

The occurrence and potential relevance of non-ideal effects in single droplet setups is therefore profusely demonstrated in this work. Given the great importance of isolated droplet experiments as source of reference data for spray evaporation and combustion, the magnitude of these potential deviations needs to be critically assessed in order to correctly interpret and use experimental data. The analysis proposed here, in terms of easily calculable dimensionless numbers, is thought to provide a novel and valid framework in this regard that can be used, among others, to assess the magnitude of deviations for a particular case or to select the experimental conditions that minimize or limit the impact of the various experimental artifacts.

The coupling of experiments and the evaporation model also allowed to develop and validate a novel methodology to formulate evaporation surrogates of liquid fuels for high-temperature applications. This method is conceived as a comprehensive and systematic procedure covering the different phases of the problem. In the first place, the knowledge obtained through the sensitivity analysis detailed before was used to define in an objective manner the most important target properties for the physical surrogate. Secondly, the palette compounds are chosen following a systematic approach, by defining hypothetical pseudo-components that reproduce the properties of the target fuel and, then, identifying the set of real hydrocarbons that best match those properties. Finally, the optimal mass fractions of the mixture are determined through a multi-objective optimization procedure that combines a genetic algorithm and an artificial neural network.

This method has been applied on three practical multicomponent fuels, namely diesel, Jet A and heating oil, covering therefore a broad range of real applications. Predicted fuel droplet evaporation curves for the surrogates showed a remarkable agreement with experimental data for the three target fuels tested. In the case of the diesel surrogate, the modeling results were also compared with different surrogates from the literature, revealing the importance of using a multicomponent scheme to accurately reproduce the evaporation behavior of a real fuel. In addition, it was noticed that evaporation surrogates satisfactorily validated under low temperature conditions may not perform well when evaluated at high temperature conditions representative of real combustion applications.

The current approach is thought to be a novel and promising method to systematically develop physical surrogates, allowing to select the palette compounds in a systematic manner. Even if the model has been used here to match evaporation behaviors, it has been conceived as a general purpose method that can be readily combined with other relevant combustion criteria (e.g., gas-phase chemistry, sooting propensity, etc.).

Finally, the evaporation behaviors of nanofuel droplets for high temperature applications have been explored at the SDF, using diesel as a base fuel and different nanoparticles (ceria, alumina, carbon nanotubes) as additives. The experimental results revealed the influence of nanoparticle addition, showcasing distinct phases in the evaporation process of nanofuel droplets, spanning from smooth evaporation to fluctuating evaporation and concluding with gelation and dry-out. Moreover, a quantitative evaluation of the impact of adding these nanoparticles revealed heightened evaporation rates in the early stages, ascribed to an enhanced thermal conductivity for the droplet and an augmented absorption of thermal radiation. This study also employed the surrogate formulation approach detailed before aiming to emulate the nanodroplet evaporation behavior within specific intervals, yielding promising results. This preliminary exploration is thought to contribute to the understanding of nanofuel droplet evaporation behaviors, particularly in high-temperature environments, and lays the groundwork for future research in this domain. Also, the application of the surrogate formulation procedure developed in this thesis to nanofuels serves to demonstrate the versatility of the method, which can be adapted to different case studies and target behavior indices in a systematic and straightforward manner.

8.2 Future work

The comprehensive investigation of droplet evaporation presented in this thesis has opened up several avenues for future research and further exploration in the field of liquid fuel combustion.

Building upon the foundations established in this work, the following areas represent promising directions for future research.

From the modeling side, the developed modeling tools are thought to require further elaboration to include relevant combustion phenomena, in particular gas-phase chemical reactions. The inclusion of this feature in the modeling tool would provide the opportunity to study relevant phenomena during droplet combustion (ignition, location and temperature of the envelope flame, etc.) or to characterize the impact of pyrolysis reactions for multi-component fuels. This tool could also be used to formulate fuel surrogate blends targeting gas-phase related combustion behaviors. Furthermore, this expanded model could be used to evaluate the effect of experimental artifacts on the experimental measurements for droplet combustion conditions, complementing the current work developed for high-temperature droplet evaporation.

Regarding the surrogate formulation approach, this methodology could be extended to encompass a wider range of hydrocarbon families, including olefins, aromatics, paraffins, and naphthenes. Such extensions would enhance the representation of real-world fuel behaviors, contributing to the development of multi-objective surrogates capable of also capturing complex chemical behaviors (given that they are included in the droplet modeling tool, as discussed in the previous point).

As for the empirical studies, while this thesis has primarily focused on droplet evaporation and its modeling, future research can delve into the intricacies of gas-phase chemistry within fuel droplet combustion. Exploring droplet combustion dynamics and pollutant emissions will provide valuable insights into the overall combustion process, contributing to the development of cleaner and more efficient combustion technologies. More specifically, investigating into the soot and particulate matter formation is an important aspect that merits further investigation. Moreover, some residual, viscous fuels (such as heavy fuel oil) or alternative fuels derived from waste (such as pyrolysis oils) are known to generate cenospheres upon their combustion. The minimization of these solid carbonaceous emissions is a paramount challenge for a clean and efficient conversion of this kind of fuels. Therefore, the developed experimental and modeling tools on isolated droplets could be extended to characterize and study this phenomenon of great practical relevance.

Regarding the increasing interest in sustainable and alternative fuel sources, future research can explore the behavior of novel, alternative liquid fuels (e.g., the aforementioned pyrolysis oils, bio-kerosenes, by-products from industrial processes, etc.), whose combustion behaviors are usually not well characterized. The detailed characterization methods developed in this dissertation could be helpful in gaining insight into these novel fuels, both at conventional combustion conditions and also under more advanced combustion environments such as oxy-fuel or MILD combustion atmospheres, and can also be extended to address other relevant thermal conversion methods such as gasification.

9. Conclusiones

9.1 Resumen y conclusiones

En esta tesis se ha empleado un enfoque multifacético que combina técnicas experimentales y de modelización para investigar la dinámica de la evaporación de gotas de combustible en entornos de alta temperatura. La motivación detrás de este enfoque radica en la necesidad de obtener una comprensión más profunda del proceso de evaporación, particularmente en escenarios relevantes para aplicaciones prácticas como las que se encuentran en las unidades de combustión de combustibles líquidos (por ejemplo, calderas u hornos).

Para ello, a lo largo de esta tesis se han utilizado dos configuraciones experimentales diferentes para caracterizar la vaporización de gotas de combustible aisladas en condiciones similares a las de una llama, a saber: la Instalación de Combustión de Gotas (DCF) y la Instalación de Gotas Suspendidas (SDF). La primera se desarrolló previamente de acuerdo con el marco de la gota en caída libre, proporcionando condiciones de prueba con gotitas de pequeño tamaño (~150 µm) sin soporte que se vaporizan a alta temperatura (~1700 K). Este último se ha desarrollado en este estudio de doctorado de acuerdo con el enfoque de gotas suspendidas y presenta gotas significativamente mayores (~300-1100 µm), que en este caso están ancladas por diferentes fibras sólidas. La instalación SDF ha sido diseñada para permitir probar diferentes temperaturas de gas (~700, 1000, 1336 K), siendo esta última la utilizada a lo largo de esta tesis doctoral. Además, en ambas instalaciones es posible ajustar la composición del coflujo de gas, permitiendo una amplia gama de condiciones experimentales, desde la evaporación pura hasta la combustión convencional u oxicombustión. A pesar de que los experimentos en ambas instalaciones se realizan en condiciones de gravedad normal, la presencia constante de llamas envolventes casi esféricas proporcionó pruebas convincentes de que la vaporización de las gotas se produce en condiciones que se aproximan a la simetría esférica. En ambas instalaciones se ha llevado a cabo un gran número de experimentos utilizando una gama notablemente amplia de condiciones, tanto para compuestos puros (por ejemplo, etanol, butanol, glicerol) como para combustibles reales (gasóleo, queroseno, gasóleo de calefacción). Los resultados empíricos obtenidos en estas instalaciones tienen potencial para servir a diversos fines dentro de la investigación académica y las aplicaciones de ingeniería. En concreto, pueden emplearse para análisis comparativos entre distintos tipos de combustibles, como datos específicos de combustibles necesarios para la simulación de pulverizaciones en herramientas computacionales o como medio para validar modelos relacionados con la evaporación y combustión de gotas, como se detalla más adelante.

Otro componente crucial de esta tesis implica el desarrollo y la validación de modelos teóricos sobre la vaporización de gotas aisladas, con un enfoque específico en escenarios prácticos que implican entornos de alta temperatura y combustibles multicomponentes. Este modelo de evaporación se ha desarrollado y validado con éxito, tanto mediante datos bibliográficos como por comparación con los resultados de DCF y SDF. Además, en el contexto de una sola gota que se vaporiza en un entorno de alta temperatura mientras está suspendida por fibras (por ejemplo, las condiciones de ensayo aplicadas en el SDF), se han desarrollado dos submodelos distintos para tener en cuenta el impacto de la conducción del calor a través de las fibras y la absorción de la radiación térmica en el proceso de evaporación. Estos submodelos también se han validado con éxito comparándolos tanto con los datos bibliográficos existentes como con los resultados obtenidos en el SDF.

Cualquier herramienta computacional que prediga los comportamientos de evaporación/combustión requiere no sólo una descripción matemática fiable del proceso que se modela, sino también valores precisos para las numerosas propiedades físico-químicas implicadas. Una búsqueda específica reveló una importante laguna en la literatura para esta cuestión, aunque se reconoce como una fuente relevante de error que puede socavar la fiabilidad de los cálculos de evaporación. Para abordar esta cuestión, se ha llevado a cabo un análisis de sensibilidad local para evaluar la influencia de las incertidumbres en las propiedades sobre las predicciones del modelo de vaporización de gotas validado, confirmando el impacto potencialmente elevado de las imprecisiones en estas propiedades sobre la fiabilidad de las predicciones. Se analizó la propagación de las incertidumbres desde los datos de entrada hacia los parámetros de evaporación, obteniéndose factores de multiplicación del orden de uno (es decir, incertidumbres relativas en las salidas similares a las de las entradas) para una serie de propiedades, entre las que se incluyen el calor específico, la conductividad térmica o la densidad del líquido, e incrementándose hasta 3 para la temperatura de ebullición. Para el caso de prueba específico considerado en este estudio (evaporación de gotas de gasóleo a altas temperaturas), deben esperarse variaciones de hasta ~90% en algunas métricas de evaporación dependiendo de las hipótesis particulares aplicadas, entre las normalmente consideradas en los trabajos publicados. Por lo tanto, una evaluación correcta de las propiedades de un combustible determinado parece ser una cuestión clave para conseguir predicciones precisas de la evaporación de las gotas y, por lo tanto, de las llamas de pulverización.

En el contexto de los experimentos con gotas individuales, la mayoría de los bancos de pruebas pretenden emular la configuración simplificada y canónica en la que una gota aislada se vaporiza únicamente por conducción de calor gas-líquido en una atmósfera completamente quiescente carente de convección. En estas condiciones, el proceso se vuelve esférico-simétrico, lo que facilita considerablemente los esfuerzos de modelización y la interpretación de los resultados. Sin embargo, es bien sabido que los experimentos reales a menudo se ven afectados por artefactos experimentales que pueden dar lugar a desviaciones significativas de este supuesto escenario ideal, como la conducción de calor a través de las fibras de suspensión, la absorción de radiación térmica o el inicio de la convección debido a las velocidades relativas entre la gota y el gas circundante. La aparición de estos efectos puede considerarse omnipresente en la mayoría de los experimentos de evaporación de gotas y, por lo tanto, la mayoría de los datos publicados en la literatura sobre la evaporación de gotas están, en cierta medida, afectados por ellos. Una revisión bibliográfica identificó que las desviaciones en la tasa de evaporación de gotas(K) pueden incluso superar el 100% debido a estos artefactos, en comparación con el caso canónico en el que el único modo de transferencia de calor es la conducción a través de la interfaz gas-gotas ($\dot{Q}_{gc}$). Por tanto, la magnitud de estas desviaciones debe ser evaluada para permitir una correcta interpretación y utilización de los resultados experimentales. Para ello, se ha realizado un análisis teórico con el objetivo de determinar los parámetros relevantes y las magnitudes de los diferentes artefactos experimentales. Se propone un número adimensional para cada artefacto, basado en la relación entre el aporte de calor debido a estos respectivos modos adicionales de transferencia de calor y . De esta forma, se formulan los números de fibra, radiación y convección (*FN*, *RN* y *CN*, respectivamente). Para valores moderados de estos aportes adicionales de calor, se obtiene una correlación lineal, lo que indica que la desviación de la tasa de evaporación de las gotas con respecto al caso canónico(*K/Kcan*) puede predecirse basándose en *FN*, *RN* y *CN*. Dado que estos números adimensionales pueden calcularse fácilmente a partir de los parámetros característicos globales del problema, puede estimarse fácilmente el impacto de cada artefacto experimental en la tasa de evaporación de las gotas.

Este análisis teórico se ha validado con resultados tanto de DCF como de SDF, para una gama notablemente amplia de condiciones de ensayo, lo que se cree que constituye una base de datos única a este respecto. Las tasas de evaporación extraídas muestran una amplia variabilidad, con *K/Kcan* que oscila entre ~ 1,1 y ~ 2,1, dependiendo del tamaño y la conductividad de las fibras de soporte utilizadas en las pruebas SDF. Por el contrario, los resultados del DCF muestran desviaciones mucho menores de la tasa de evaporación canónica(*K/Kcan* ~ 1,03), debido principalmente a que se ensayaron gotas no suspendidas y muy pequeñas. Todos estos resultados experimentales, junto con los datos de la literatura para condiciones de ensayo bastante diferentes, demuestran la utilidad del enfoque propuesto para analizar las desviaciones de la tasa de evaporación debidas a estos artefactos. Además, para valores entre pequeños y moderados de *FN*, *RN* y *CN*, los resultados mostraron tendencias bien definidas coherentes con una superposición de los distintos modos de transferencia de calor, de modo que la relación *K/K* puede estimarse fácilmente como ~ (*1+FN+RN+CN*).

Por tanto, en este trabajo se demuestra profusamente la aparición y relevancia potencial de los efectos no ideales en configuraciones de gotas aisladas. Dada la gran importancia de los experimentos con gotas aisladas como fuente de datos de referencia para la evaporación y combustión de aerosoles, es necesario evaluar críticamente la magnitud de estas posibles desviaciones para interpretar y utilizar correctamente los datos experimentales. Se cree que el análisis propuesto aquí, en términos de números adimensionales fácilmente calculables, proporciona un marco novedoso y válido a este respecto que puede utilizarse, entre otras cosas, para evaluar la magnitud de las desviaciones para un caso particular o para seleccionar las condiciones experimentales que minimizan o limitan el impacto de los diversos artefactos experimentales.

El acoplamiento de los experimentos y el modelo de evaporación también permitió desarrollar y validar una metodología novedosa para formular sustitutos de evaporación de combustibles líquidos para aplicaciones a alta temperatura. Este método se concibe como un procedimiento global y sistemático que abarca las distintas fases del problema. En primer lugar, se utilizaron los conocimientos obtenidos mediante el análisis de sensibilidad detallado anteriormente para definir de forma objetiva las propiedades objetivo más importantes para el sustituto físico. En segundo lugar, se eligen los compuestos de la paleta siguiendo un enfoque sistemático, definiendo pseudocomponentes hipotéticos que reproducen las propiedades del combustible objetivo y, a continuación, identificando el conjunto de hidrocarburos reales que mejor se ajustan a dichas propiedades. Por último, se determinan las fracciones másicas óptimas de la mezcla mediante un procedimiento de optimización multiobjetivo que combina un algoritmo genético y una red neuronal artificial.

Este método se ha aplicado a tres combustibles multicomponentes prácticos, a saber, gasóleo, Jet A y gasóleo de calefacción, cubriendo así una amplia gama de aplicaciones reales. Las curvas de evaporación de gotas de combustible predichas para los sustitutos mostraron una notable concordancia con los datos experimentales para los tres combustibles objetivo ensayados. En el caso del sustituto del gasóleo, los resultados de la modelización también se compararon con diferentes sustitutos de la bibliografía, lo que revela la importancia de utilizar un esquema multicomponente para reproducir con precisión el comportamiento de evaporación de un combustible real. Además, se observó que los sustitutos de evaporación validados satisfactoriamente en condiciones de baja temperatura pueden no funcionar bien cuando se evalúan en condiciones de alta temperatura representativas de las aplicaciones de combustión reales.

El enfoque actual se considera un método novedoso y prometedor para desarrollar sistemáticamente sustitutos físicos, lo que permite seleccionar los compuestos de la paleta de forma sistemática. Aunque el modelo se ha utilizado aquí para igualar los comportamientos de evaporación, se ha concebido como un método de uso general que puede combinarse fácilmente con otros criterios de combustión pertinentes (por ejemplo, la química en fase gaseosa, la propensión al hollín, etc.).

Por último, se han explorado en el SDF los comportamientos de evaporación de gotas de nanocombustible para aplicaciones a alta temperatura, utilizando gasóleo como combustible base y diferentes nanopartículas (ceria, alúmina, nanotubos de carbono) como aditivos. Los resultados experimentales revelaron la influencia de la adición de nanopartículas, mostrando distintas fases en el proceso de evaporación de las gotas de nanocombustible, que van desde la evaporación suave a la evaporación fluctuante y concluyen con la gelificación y el secado. Por otra parte, una evaluación cuantitativa del impacto de la adición de estas nanopartículas reveló un aumento de las tasas de evaporación en las primeras etapas, atribuido a una mayor conductividad térmica de la gota y un aumento de la absorción de la radiación térmica. En este estudio también se empleó el enfoque de formulación sustitutiva detallado anteriormente con el objetivo de emular el comportamiento de evaporación de las nanogotas en intervalos específicos, lo que arrojó resultados prometedores. Se cree que esta exploración preliminar contribuirá a la comprensión de los comportamientos de evaporación de las gotas de nanocombustible, especialmente en entornos de alta temperatura, y sienta las bases para futuras investigaciones en este campo. Asimismo, la aplicación del procedimiento de formulación de sustitutos desarrollado en esta tesis a los nanocombustibles sirve para demostrar la versatilidad del método, que puede adaptarse a diferentes casos de estudio e índices de comportamiento objetivo de forma sistemática y sencilla.

9.2 Trabajos futuros

La investigación exhaustiva de la evaporación de gotas presentada en esta tesis ha abierto varias vías para futuras investigaciones y una mayor exploración en el campo de la combustión de combustibles líquidos. Partiendo de las bases establecidas en este trabajo, las siguientes áreas representan direcciones prometedoras para futuras investigaciones.

Desde el punto de vista de la modelización, se considera que las herramientas de modelización desarrolladas requieren una mayor elaboración para incluir fenómenos de combustión relevantes, en particular las reacciones químicas en fase gaseosa. La inclusión de esta característica en la herramienta de modelización brindaría la oportunidad de estudiar fenómenos relevantes durante la combustión de gotas (ignición, localización y temperatura de la llama envolvente, etc.) o de caracterizar el impacto de las reacciones de pirólisis para combustibles multicomponentes. Esta herramienta también podría utilizarse para formular mezclas de combustibles sustitutos que tengan como objetivo comportamientos de combustión relacionados con la fase gaseosa. Además, este modelo ampliado podría utilizarse para evaluar el efecto de los artefactos experimentales en las mediciones experimentales de las condiciones de combustión de gotas, complementando el trabajo actual desarrollado para la evaporación de gotas a alta temperatura.

En cuanto al enfoque de la formulación de sustitutos, esta metodología podría ampliarse para abarcar una gama más amplia de familias de hidrocarburos, incluidas las olefinas, los aromáticos, las parafinas y los naftenos. Tales extensiones mejorarían la representación de los comportamientos de los combustibles en el mundo real, contribuyendo al desarrollo de sustitutos multiobjetivo capaces de capturar también comportamientos químicos complejos (dado que se incluyen en la herramienta de modelado de gotas, como se ha comentado en el punto anterior).

En cuanto a los estudios empíricos, aunque esta tesis se ha centrado principalmente en la evaporación de gotas y su modelización, futuras investigaciones pueden profundizar en los entresijos de la química en fase gaseosa dentro de la combustión de gotas de combustible. Explorar la dinámica de la combustión de las gotas y las emisiones contaminantes proporcionará información valiosa sobre el proceso general de combustión, contribuyendo al desarrollo de tecnologías de combustión más limpias y eficientes. Más concretamente, investigar la formación de hollín y partículas es un aspecto importante que merece una mayor investigación. Además, se sabe que algunos combustibles residuales y viscosos (como el fuelóleo pesado) o combustibles alternativos derivados de residuos (como los aceites de pirólisis) generan cenosferas en su combustión. La minimización de estas emisiones carbonosas sólidas es un reto primordial para una conversión limpia y eficiente de este tipo de combustibles. Por lo tanto, las herramientas experimentales y de modelización desarrolladas en gotas aisladas podrían ampliarse para caracterizar y estudiar este fenómeno de gran relevancia práctica.

En relación con el creciente interés por las fuentes de combustible sostenibles y alternativas, futuras investigaciones pueden explorar el comportamiento de nuevos combustibles líquidos alternativos (por ejemplo, los ya mencionados aceites de pirólisis, bioquerosenos, subproductos de procesos industriales, etc.), cuyos comportamientos de combustión no suelen estar bien caracterizados. Los métodos de caracterización detallada desarrollados en esta tesis podrían ser útiles para conocer mejor estos nuevos combustibles, tanto en condiciones de combustión convencionales como en entornos de combustión más avanzados, como atmósferas de oxicombustión o combustión MILD, y también pueden extenderse para abordar otros métodos de conversión térmica relevantes, como la gasificación.

Appendices

Appendix A: Radiation heat flux measurements for McKenna burner

In order to measure the radiative heat flux reaching the droplet location at both experimental facilities (DCF and SDF), an ellipsoidal radiometer is employed. A schematic of this probe is shown in Figure A.1.a. Since both facilities share a common flat-flame burner operating at exactly the same conditions, all the measurements could be performed in a single setup (DCF). The ellipsoidal probe is mounted on the DCF setup as shown in the Figure A.1.b to measure the radiation heat flux at few required locations. These locations are the following:

- L=65 mm: axial distance between the burner and the droplet location for the nominal conditions used in SDF tests (T_g ~1400 K).
- L=147 mm: axial distance between the burner and the droplet location for the intermediate temperature conditions at the SDF tests (not used in this thesis, T_g~1000 K).
- L=259 mm: axial distance between the burner and the droplet location for the low temperature conditions at the SDF tests (not used in this thesis, T_g~700 K).

As for the DCF setup, the free-falling droplets continuously vary their axial distance to the flat-flame burner (i.e., the main emitter of thermal radiation). Therefore, additional points were added to the test matrix in order to obtain the radiation flux (Q''_{rad}) profiles displayed in Figure A.2.

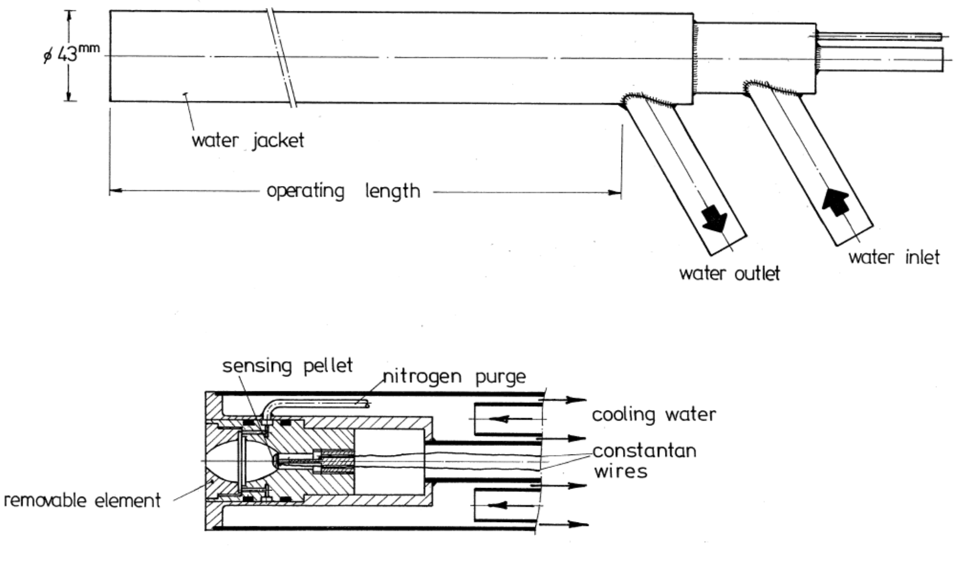

a)

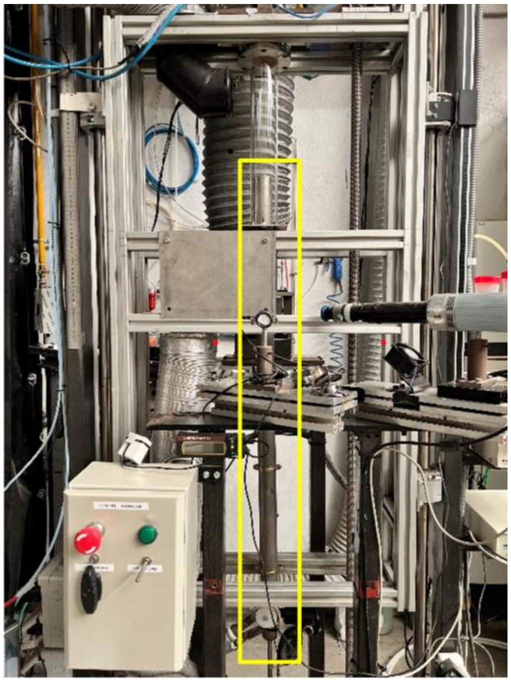

b)

Figure A.1, a) Schematic of ellipsoidal radiometer probe used for the measurements, b) Radiometer probe mounted on the DCF.

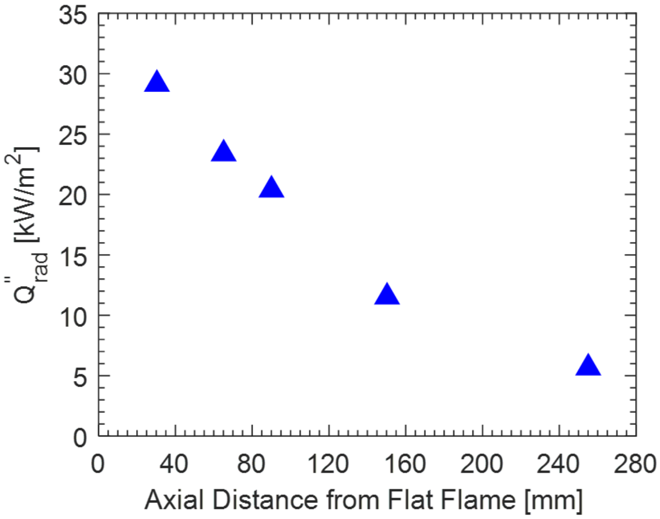

Figure A.2, Radiative heat flux measured at various distances from the flat flame using the ellipsoidal radiometer probe

As expected, the radiative heat flux decreases as the probe moves farther away from the main emitter (flat flame). For the SDF arrangement used in this thesis, the Q''_{rad} reaching the droplet location is 23.5 kW/m^2 at 65 mm from the burner surface.

Appendix B: Gas temperature measurement at the SDF

In order to perform the transient temperature measurement at the SDF setup, a 70μm S-type thermocouple was used. The hot junction of this thermocouple was placed at the droplet location in order to record the temperature transient when the air shield was cut. A National Instruments USB 6210 data logger was used with MATLAB to record the temperature response from the thermocouple by using a sampling frequency of 2000 Hz.

The obtained raw data displayed a quite high variability and noise, and therefore a moving average was applied, using a windows size of 10 points. The resulting data are plotted in Figure B.1, where the transient heat-up of the thermocouple is shown in blue. However, the purpose of these measurements is to obtain the temperature profile of the surrounding gas, since this information is required as an input by the model described in Chapter 3. Assuming a first order system, the temperatures of gas (T_g) and thermocouple (T_{thc}) can be related with the following equation:

$$\tau \frac{\partial T_{thc}}{\partial t} + T_{thc} = T_g \tag{B1}$$

Where, τ is the time constant for the 70 μm S-type thermocouple ($\tau = mC/(hA)$, estimated as 92 ms). The gas temperature temporal evolution obtained is also plotted in Figure B.1.

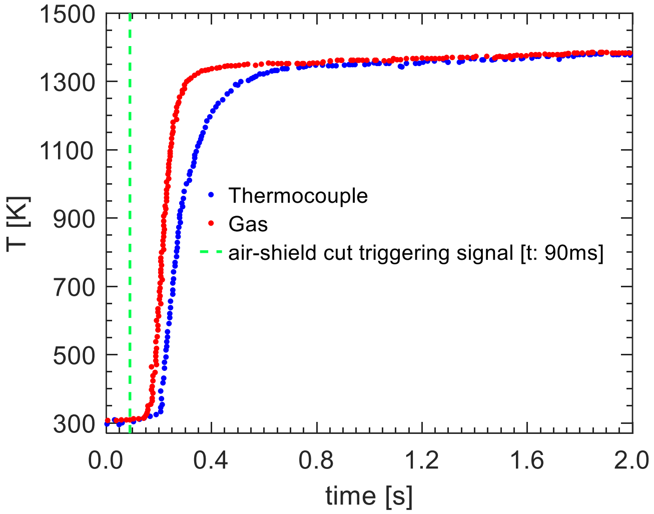

Figure B.1, Thermocouple temperature response versus gas temperature response

Appendix C: Methods for the estimation of thermophysical and transport properties

This supplementary section includes the methods and references employed in determining the thermophysical and transport properties required by the droplet evaporation model described in Chapter 3.

C.1 Liquid density

The density of the liquid phase, ρ_l, for any pure component is calculated according to (Linstrom, 1997) and (Perry, 1950). Regarding the determination of the density of mixtures, $\rho_{l,mix}$, the methodology employed involved the application of the mixture rule outlined in the work of Poling et al. (Poling et al., 2001):

$$\rho_{l,mix} = \frac{1}{\sum_{i=1}^{N} {}^{Y_i}/_{\rho_{l,i}}} \tag{C1}$$

where Y_i is the mass fraction of the i$^{\text{th}}$ compound.

C.2 Liquid specific heat

The correlations to calculate the specific heat of pure liquids, c_l, was adopted from (Linstrom, 1997) and (Perry, 1950). The following expression is used to estimate the c_l of mixture:

$$c_{l,mix} = \sum_{i=1}^{N} \left(Y_i c_{l,i}\right) \tag{C2}$$

C.3 Latent heat of vaporization

The correlations to estimate the latent heat of vaporization of pure liquids (L_v) are adopted from (Linstrom, 1997) and (Perry, 1950). L_v for mixtures is calculated using the following expression:

$$L_{v,mix} = \sum_{i=1}^{N} \left(\epsilon_i L_{v,i}\right) \tag{C3}$$

here $\epsilon_i = {}^{Y_i}/_{\sum_{i=1}^{N} Y_i}$ is the relative volatility of the i$^{\text{th}}$ component over the total mass of fuel in the vapor phase.

C.4 Liquid viscosity

The viscosity of pure liquids was obtained from (Linstrom, 1997) and (Perry, 1950). The mixture rule of Grunberg and Nissan (Poling et al., 2001) was employed to calculate the viscosity of liquid mixtures according the following expression:

$$\mu_{l,mix} = e^{\sum_{i=1}^{N}\left(X_i ln(\mu_{l,i})\right)} \tag{C4}$$

here X_i is the molar fraction of the ith compound.

C.5 Liquid thermal conductivity

The thermal conductivity of pure liquids (k_l) was adopted from (Perry, 1950) and (Yaws, 1995). For binary mixtures, the Filippov equation introduced in (Perry, 1950) was utilized:

$$k_{l,mix} = Y_1 k_{l,1} + Y_2 k_{l,2} - 0.72 \cdot Y_1 Y_2 |k_{l,2} - k_{l,1}| \tag{C5}$$

As for mixtures of more than two compounds, the Li method was used (Perry, 1950):

$$k_{l,mix} = \sum_{i=1}^{N} \sum_{j=1}^{N} \phi_i \phi_j \frac{2k_{l,i} k_{l,j}}{k_{l,i} + k_{l,j}} \tag{C6}$$

Here $\phi_i = \frac{X_i/\rho_{l,i}}{\sum_{j=1}^{N} X_j/\rho_{l,i}}$

C.6 Liquid mass diffusion coefficient

The binary liquid diffusion coefficients at infinite dilution (D_{AB}^0) are calculated using the Wilke-Chang approach (Poling et al., 2001):

$$D_{AB}^0 = \frac{7.4 \times 10^{-12} \sqrt{\varphi M W_B} T}{\mu_B V_A^{0.6}} \tag{C7}$$

here φ represents the association factor, μ_B the viscosity of the solvent (B) and V_A the molecular volume of the solute (A). From the calculated values of D_{AB}^0, the Sanchez-Clifton formula was used to estimate the mass diffusion coefficient (D_l). As detailed in (Poling et al., 2001):

$$D_l = (D_{BA}^0 X_A + D_{AB}^0 X_B)(1 - m + m \cdot \alpha) \tag{C8}$$

Being α a thermodynamic correction factor. Since a thermodynamically ideal mixture ($\alpha = 1$) was assumed (e.g., see (Sazhin et al., 2010)), the value of m was not required.

It is imperative to acknowledge that the Sanchez-Clifton formula possesses limited applicability, restricted solely to binary mixtures. When attempting to estimate the diffusion coefficient, D_l, for liquid blends containing multiple species, the process becomes considerably more intricate. This complexity necessitates the utilization of highly detailed methods, demanding an extensive array of chemical parameters specific to the mixture. To reach a balance between precision and simplicity in such instances, this work has adopted the Wilke-Chang approximation, as initially presented in the work of Sazhin (2014):

$$D_l = \frac{7.4 \times 10^{-12} \sqrt{MW_{mix}} T}{\mu_B V_{mix}^{0.6}} \tag{C9}$$

C.7 Gas density

Given the assumption of an ideal gas model, the determination of vapor density can be computed as:

$$\rho_{mix} = \frac{P\, MW_{mix}}{RT} \tag{C10}$$

C.8 Gas specific heat at constant pressure

The required correlations for the estimation of the specific heat at constant pressure (c_p) of pure gases and vapors were adopted from (McBride, 1993) and (Perry, 1950). The calculation of the c_p of mixtures was performed through the following expression:

$$c_{p,mix} = \sum_{i=1}^{N} \left(Y_i c_{p,i}\right) \tag{C11}$$

C.9 Gas viscosity

The dynamic viscosity (μ) of pure gases and vapors was obtained from (McBride, 1993) and (Perry, 1950). As for estimating the viscosity of mixtures, the Wilke rule (Kee et al., 2005), (Poling et al., 2001) was applied:

$$\mu_{mix} = \sum_{i=1}^{N} \frac{X_i \mu_i}{\sum_{j=1}^{N} X_j \Phi_{ij}} \tag{C12}$$

being:

$$\Phi_{ij} = \frac{1}{\sqrt{8}} \left(1 + \frac{MW_i}{MW_j}\right)^{-0.5} \left[1 + \left(\frac{\mu_i}{\mu_j}\right)^{0.5} \left(\frac{MW_j}{MW_i}\right)^{0.25}\right]^2 \tag{C13}$$

C.10 Gas thermal conductivity

The thermal conductivity (k) of pure gases was obtained through the kinetic theory of gases, namely by following the method proposed in (Kee et al. (2005)). As for the estimation of the thermal conductivity of blends, the mixture average formula recommended in (Kee et al., 2005) was used:

$$k_{mix} = \frac{1}{2}\left(\sum_{i=1}^{N} X_i k_i + \frac{1}{\sum_{i=1}^{N} X_i / k_i}\right) \tag{C14}$$

C.11 Gas mass diffusion coefficient

The binary mass diffusion coefficients (D_{fi}) for any pair of fuel-gas was calculated through the kinetic theory of gases, namely by following the method proposed in (Kee et al. (2005)). For the case of multicomponent gas mixtures, the combination of the different binary diffusion coefficients (D_{fi}) through the Wilke approximation recommended in (Fairbanks & Wilke, 1950) provided the final mass diffusion coefficient (*D*):

$$D = \frac{1 - X_f}{\sum_{i \neq f}^{N} X_i / D_{fi}} \tag{C15}$$

Appendix D: Pseudo-component breakdown

Following the approach detailed in (Castells et al., 1992), the distillation curve of the target fuel (i.e., complex hydrocarbon mixture) is divided into a number of equal temperature intervals. Hereafter, each temperature interval is treated as a petroleum cut or Pseudo-Component (PC), whose boiling point is set according to the average boiling temperature of the interval. This procedure is called pseudo-component breakdown. Since, the properties of hydrocarbons can be considered as functions of molecular weight, boiling point, density etc. Hence, in order to estimate the PCs properties, the values of those parameters have to be known. Knowing the normal boiling point (T_b) and the average density of the target fuel, the Watson factor hypothesis can be used (Riazi, 2005) to calculate the density of each PC. The Watson factor (K_w) is calculated as the following equation D1:

$$K_w = 1.8\left({T_b}^{1/3}\big/ SG_T\right) \tag{D1}$$

where SG_T is the standard specific gravity of the target fuel. Hereafter, the density of each PC can be calculated by Equation (D2).

$$\rho_{l,i} = 1215.253\left({T_{b,i}}^{1/3}\big/ K_w\right) \tag{D2}$$

here, $T_{b,i}$ and $\rho_{l,i}$ are the boiling point and density of a PC, respectively. In order to relax the constant Watson factor assumption, Castells et al. (1992) developed a more efficient approach in which the estimated density and boiling point for the PCs have to satisfy the following conservation equations for mass, volume, moles and molar fraction balances:

$$\sum_{i=1}^{N_{PC}} x_{V_i} = 1 \tag{D3}$$

$$\rho = \sum_{i=1}^{N_{PC}} x_{V_i}\rho_{l,i} \tag{D4}$$

$$\frac{\rho}{M} = \sum_{i=1}^{N_{PC}} x_{V_i}\frac{\rho_{l,i}}{M_i} \tag{D5}$$

$$\sum_{i=1}^{N_{PC}} x_i = 1 \text{ where } x_i = x_{V_i}\frac{\rho_{l,i}}{\rho}\frac{M}{M_i} \tag{D6}$$

where N_{PC}, x_{V_i}, x_i, M_i, ρ and M are the number of PCs, volume fraction, mole fraction, the molecular weight of the ith PC and density of the target fuel, respectively. Solving the conservation equations in order to find the mass fractions, boiling point and density of the PCs requires for minimizing the following error functions (see Equation (D7)) through an iterative non-linear optimization procedure. The detail of this process is comprehensively explained in (Castells et al., 1992).

$$
\begin{gathered}
E(\rho_i) = \frac{E_1^2 + E_2^2}{2} \\
E_1 = \frac{\frac{\rho}{M} - \sum_{i=1}^{N_{PC}} x_{V_i} \frac{\rho_{l,i}}{M_i}}{\frac{\rho}{M}}, \qquad E_1 = 1 - \sum_{i=1}^{N_{PC}} x_{V_i} \frac{\rho_{l,i}}{\rho} \frac{M}{M_i}
\end{gathered}
\tag{D7}
$$

Once the optimized specific gravity and boiling point for each PC are obtained, the rest of the relevant properties for each PC are estimated on the basis of the correlations reported by Riazi (2005) (see Appendix E).

Appendix E: Pseudo-component properties

The correlations used to calculate the physicochemical properties for surrogate mixtures are mainly taken from (Poling et al., 2001; Riazi, 2005; Viswanath et al., 2007). The properties are assumed to be a function of temperature and composition (in the case of multicomponent mixtures). All formulas and variables are expressed in SI units.

E.1 Liquid density: modified Rackett correlation (Poling et al., 2001).

$$\rho_l = \frac{RT_c}{P_c} Z_{RA}{}^{[1+(1-T/T_c)^{2/7}]} \tag{E1}$$

Where T_c and P_c are the critical temperature (K) and critical pressure (Pa), respectively. R is the universal gas constant and Z_{RA} is the correction factor, which is calculated as:

$$Z_{RA} = \left(\frac{1}{\rho_{T_{RA}} V_c}\right)^{\frac{1}{[1+(1-T_{RA}/T_c)^{2/7}]}} \tag{E2}$$

where V_c is the critical volume, T_{RA} is equal to 293 K and $\rho_{T_{RA}}$is the saturated liquid density at T_{RA}.

E.2 Saturated vapor pressure: Riedel correlation (Poling et al., 2001).

$$\begin{gathered} ln(P_{vr}) = A^+ - \frac{B^+}{T_r} + C^+ ln(T_r) + D^+ T_r{}^6 A^+ = -35Q, \\ B^+ = -36Q, \qquad C^+ = 42Q + \alpha_c, D^+ = -Q, Q = K(3.758 - \alpha_c) \\ \alpha_c = \frac{3.758K\psi_b + ln(P_c/1.01325)}{K\psi_b - ln(T_{br})}, \qquad K = 0.0838, \qquad T_{br} = \frac{T_b}{T_c}, T_r = \frac{T}{T_c} \\ \psi_b = -35 + \frac{36}{T_{br}} + 42ln(T_{br}) - (T_{br})^6 \end{gathered} \tag{E3}$$

where T_{br} and T_r are the reduced temperature and reduced boiling point temperature.

E.3 Liquid viscosity: Dutt's development correlation (Viswanath et al., 2007).

$$ln(\mu_l/\rho_l) = -3.0171 \left[\frac{442.78 + 1.6452(T_b - 273)}{T + \left(239 - 0.19(T_b - 273)\right)}\right] \tag{E4}$$

where ρ_l is the density of saturate liquid at T in g/mL.

E.4 Vapor viscosity: (Yoon and Thodos (Riazi, 2005).

$$\mu_v \zeta \times 10^5 = 1 + 46.1T_r{}^{0.618} - 20.4e^{(-0.449T_r)} + 19.4e^{(-4.058T_r)} \tag{E5}$$

$$T_r = \frac{T}{T_c}, \; \zeta = T_c^{\frac{1}{6}} M^{-\frac{1}{2}} (0.987 P_c)^{-\frac{2}{3}}$$

where M is the molecular mass.

E.5 Liquid thermal conductivity: Tsonopoulos correlation (Riazi, 2005).

$$\lambda_l = 0.05351 + 0.10177 \times (1 - T_r)^{\frac{2}{3}}, \qquad T_r = \frac{T}{T_c} \tag{E6}$$

E.6 Vapor thermal conductivity: Riazi and Faghri correlation (Riazi, 2005).

$$\begin{gathered} \lambda_v = 1.7307 A (1.8 T_b)^B SG^C \\ A = exp(21.78 - 8.0798t + 1.12981t^2 - 0.05309t^3) \\ B = exp(-4.13948 + 1.29924t - 0.17813t^2 + 0.00833t^3) \\ C = 0.19876 - 0.0312t - 0.00567t^2 \\ t = \frac{1.8T - 460}{100} \end{gathered} \tag{E7}$$

where SG is the standard specific gravity.

E.7 Latent heat of vaporization: Riazi and Daubert correlation (Riazi, 2005).

$$\begin{gathered} Lv = \frac{Lv_{norm}^{T_b}}{MW} \times \left(\frac{1 - T_r}{1 - T_{br}}\right)^{0.38} \\ Lv_{norm}^{T_b} = 37.32315 \times \left(T_b{}^{1.14086} SG^{9.77089 \times 10^{-3}}\right) \end{gathered} \tag{E8}$$

E.8 Liquid specific heat capacity: Lee-Kesler method (Riazi, 2005).

$$\begin{gathered} Cp_l = a(b + cT) \\ a = 1.4651 + 0.2302k_w \\ b = 0.306469 - 0.16734SG \\ c = 0.001467 - 0.000551SG \end{gathered} \tag{E9}$$

E.9 Vapor specific heat capacity: Lee-Kesler method (Riazi, 2005).

$$\begin{gathered} Cp_v = MW(A_0 + A_1 T + A_2 T^2 - C[B_0 + B_1 T + B_2 T^2]) \\ \begin{cases} A_0 = -1.41779 + 0.11828 \times \mathrm{k}_w \\ A_1 = -\left(6.99724 - 8.69326 \times \mathrm{k}_w + 0.27715 * \mathrm{k}_w{}^2\right) \times 10^{-4} \\ A_2 = -2.2582 \times 10^{-6} \end{cases} \\ \begin{cases} B_0 = 1.09223 - 2.48248\omega \\ B_1 = -(3.434 - 7.14\omega) \times 10^{-3} \\ B_2 = -(7.2661 - 9.2561\omega) \times 10^{-7} \end{cases} \end{gathered} \tag{E10}$$

where ω and k_w are the acentric factor and Watson K factor, respectively.

References

Abdelghaffar, W. A., Elwardany, A., & Sazhin, S. S. (2010). Modeling of the processes in Diesel engine−like conditions: Effects of fuel heating and evaporation. *Atomization and Sprays*, *20* (8), 737-747.

Aboalhamayie, A., Festa, L., & Ghamari, M. (2019). Evaporation rate of colloidal droplets of jet fuel and carbon-based nanoparticles: Effect of thermal conductivity. *Nanomaterials*, *9* (9), 1297.

Abramzon, B., & Sazhin, S. (2005). Droplet vaporization model in the presence of thermal radiation. *International Journal of Heat and Mass Transfer*, *48*(9), 1868-1873.

Abramzon, B., & Sirignano, W. A. (1989). Droplet vaporization model for spray combustion calculations. *International Journal of Heat and Mass Transfer*, *32*(9), 1605-1618.

Agarwal, D. K., Vaidyanathan, A., & Kumar, S. S. (2016). Experimental investigation on thermal performance of kerosene–graphene nanofluid. *Experimental Thermal and Fluid Science*, *71*, 126-137.

Allen, M. R., Frame, D. J., Huntingford, C., Jones, C. D., Lowe, J. A., Meinshausen, M., & Meinshausen, N. (2009). Warming caused by cumulative carbon emissions towards the trillionth tonne. *Nature*, *458*, 1163-1166.

Annamalai, K., & Ryan, W. (1992). Interactive processes in gasification and combustion. Part I: Liquid drop arrays and clouds. *Progress in Energy and Combustion Science*, *18*(3), 221-295.

Aspen. (2017). *Aspen HYSYS V9*. AspenTech, Bedford.

ASTM, D (1997). *Standard test method for distillation of petroleum products at atmospheric pressure*. American Society for Testing Materials. West Conshohocken PA, USA

ASTM, D (2019). *ASTM D2887-19ae2, Standard Test Method for Boiling Range Distribution of Petroleum Fractions by Gas Chromatography*. In. West Conshohocken, PA.

Avedisian, C. T. (1985). The homogeneous nucleation limits of liquids. *Journal of Physical and Chemical Reference Data*, *14*(3), 695-729.

Avedisian, C. T. (2014). Developing Surrogates for Liquid Transportation Fuels: The Role of Spherically Symmetric Droplet Combustion. *Novel Combustion Concepts for Sustainable Energy Development,* 379-402.

Avedisian, C. T., & Jackson, G. S. (2000). Soot patterns around suspended n-heptane droplet flames in a convection-free environment. *Journal of Propulsion and Power*, *16*(6), 974-979.

Azimi, A., Arabkhalaj, A., Markadeh, R. S., & Ghassemi, H. (2018). Fully transient modeling of the heavy fuel oil droplets evaporation. *Fuel*, *230*, 52-63.

Babinsky, E., & Sojka, P. (2002). Modeling drop size distributions. *Progress in Energy and Combustion Science*, *28*(4), 303-329.

Baek, S. W., Park, J. H., & Choi, C. E. (1999). Investigation of droplet combustion with nongray gas radiation effects. *Combustion Science and Technology*, *142*(1-6), 55-79.

Bai, Y., Wang, Y., Wang, X., Zhou, Q., & Duan, Q. (2021). Development of physical-chemical surrogate models and skeletal mechanism for the spray and combustion simulation of RP-3 kerosene fuels. *Energy*, *215*, 119090.

Ballester, J., & Dopazo, C. (1994). Experimental study of the influence of atomization characteristics on the combustion of heavy oil. *Combustion Science and Technology*, *103*(1-6), 235-263.

Ballester, J., & Dopazo, C. (1996). Drop size measurements in heavy oil sprays from pressure-swirl nozzles. *Atomization and Sprays*, *6*(4), 377-408.

Ballester, J. M., Fueyo, N., & Dopazo, C. (1996). Combustion characteristics of heavy oil-water emulsions. *Fuel*, *75*(6), 695-705.

Baumgarten, C. (2006). *Mixture formation in internal combustion engines*. Springer Science & Business Media.

Bayvel, L. P. (2019). *Liquid atomization*. Routledge.

Bergman, T. L., Lavine, A. S., Incropera, F. P., & Dewitt, D. P. (2015). *Fundamentals of heat and mass transfer*. (2011). John Wiley & Sons Hoboken, NJ, USA.

Bertoli, C., & Na Migliaccio, M. (1999). A finite conductivity model for diesel spray evaporation computations. *International Journal of Heat and Fluid Flow*, *20*(5), 552-561.

Binkele, L. (1986). Significance of discrete Lorenz function levels at high temperatures resulting from new metallic conductivity measurements. *High Temperatures. High Pressures*, *18*(6), 599-607.

Brandt, E. (2001). Suspended by sound. *Nature*, *413*(6855), 474-475.

Bruno, T. J. (2006). Improvements in the measurement of distillation curves. 1. A composition-explicit approach. *Industrial & Engineering Chemistry Research*, *45*(12), 4371-4380.

Castells, F., Miquel, J., & Hernandez, J. (1992). A new method for petroleum fractions and crude oil characterization. *Society of Petroleum Engineers, Reservoir Engineering, 7*(2).

Chauveau, C., Birouk, M., & Gökalp, I. (2011). An analysis of the d2-law departure during droplet evaporation in microgravity. *International Journal of Multiphase Flow*, *37*(3), 252-259.

Chauveau, C., Birouk, M., Halter, F., & Gökalp, I. (2019). An analysis of the droplet support fiber effect on the evaporation process. *International Journal of Heat and Mass Transfer*, *128*, 885-891.

Chauveau, C., Halter, F., Lalonde, A., & Gökalp, I. (2008). An experimental study on the droplet vaporization: effects of heat conduction through the support fiber. *22nd Annual Conference on Liquid Atomization and Spray Systems.*

Chedaille, J., & Braud, Y. (1972). Industrial flames. Vol. l, Measurements in Flames. Edward Arnold Ltd., London.

Chen, X., Khani, E., & Chen, C. (2016). A unified jet fuel surrogate for droplet evaporation and ignition. *Fuel*, *182*, 284-291.

Choi, S. U., & Eastman, J. A. (1995). *Enhancing thermal conductivity of fluids with nanoparticles*, (No. ANL/MSD/CP-84938; CONF-951135-29). Argonne National Lab.(ANL), Argonne, IL, United States.

Churchill, S. W., & Bernstein, M. (1977). A Correlating Equation for Forced Convection From Gases and Liquids to a Circular Cylinder in Crossflow. *Journal of Heat Transfer* , 99(2), 300–306.

Churchill, S. W., & Chu, H. H. (1975). Correlating equations for laminar and turbulent free convection from a horizontal cylinder. *International Journal of Heat and Mass Transfer*, *18*(9), 1049-1053.

Clift, R., Grace, J. R., & Weber, M. E. (2005). *Bubbles, drops, and particles*. Dover Publications.

Colket, M., Edwards, T., Williams, S., Cernansky, N. P., Miller, D. L., Egolfopoulos, F., Lindstedt, P., Seshadri, K., Dryer, F. L., & Law, C. K. (2007). Development of an experimental database and kinetic models for surrogate jet fuels. *45th AIAA Aerospace Sciences Meeting and Exhibit*.

Correa, S. M. (1993). A review of NOx formation under gas-turbine combustion conditions. *Combustion Science and Technology*, *87*(1-6), 329-362.

D. Csemány, V. Józsa (2019), Uncertainty of droplet evaporation measurements and its effect on model validation, *9th European Combustion Meeting*, 6

Curran, H. J., Fisher, E. M., Glaude, P.-A., Marinov, N. M., Pitz, W., Westbrook, C., Layton, D., Flynn, P. F., Durrett, R. P., & Zur Loye, A. (2001). Detailed chemical kinetic modeling of diesel combustion with oxygenated fuels. *SAE Transactions*, 514-521.

Dai, M., Wang, J., Wei, N., Wang, X., & Xu, C. (2019). Experimental study on evaporation characteristics of diesel/cerium oxide nanofluid fuel droplets. *Fuel*, *254*, 115633.

Dietrich, D. L., Ferkul, P. V., Bryg, V. M., Nayagam, M. V., Hicks, M. C., Williams, F. A., Dryer, F. L., Shaw, B. D., Choi, M. Y., & Avedisian, C. T. (2015). Detailed results from the flame extinguishment experiment (FLEX) March 2009 to December 2011.

Dietrich, D. L., Nayagam, V., Hicks, M. C., Ferkul, P. V., Dryer, F. L., Farouk, T., Shaw, B. D., Suh, H. K., Choi, M. Y., & Liu, Y. C. (2014). Droplet combustion experiments aboard the international space station. *Microgravity Science and Technology*, *26*, 65-76.

Dombrovsky, L., & Sazhin, S. (2003). Absorption of thermal radiation in a semi-transparent spherical droplet: a simplified model. *International Journal of Heat and Fluid Flow*, *24*(6), 919-927.

El-Seesy, A. I., Abdel-Rahman, A. K., Bady, M., & Ookawara, S. (2017). Performance, combustion, and emission characteristics of a diesel engine fueled by biodiesel-diesel mixtures with multi-walled carbon nanotubes additives. *Energy Conversion and Management*, *135*, 373-393.

Elwardany, A. E., J. Badra, J. Sim, M. Khurshid, M. Sarathy, H. G. Im. (2016). Modeling of heating and evaporation of FACE I gasoline fuel and its surrogates. *SAE International*, 1-7.

Elwardany, A., Sazhin, S., & Im, H. G. (2016). A new formulation of physical surrogates of FACE A gasoline fuel based on heating and evaporation characteristics. *Fuel*, *176*, 56-62.

Errante, P., Corre, C., & Makhlouf, S. (2018). Uncertainty Quantification for the Eulerian-Lagrangian simulation of evaporating sprays. *Proceeding of 14th Triennial International Conference on Liquid Atomization Spray*, 1-8.

Fairbanks, D., & Wilke, C. (1950). Diffusion coefficients in multicomponent gas mixtures. *Industrial & Engineering Chemistry*, *42*(3), 471-475.

Fang, B., Chen, L., Li, G., & Wang, L. (2019). Multi-component droplet evaporation model incorporating the effects of non-ideality and thermal radiation. *International Journal of Heat and Mass Transfer*, *136*, 962-971.

Farouk, T., & Dryer, F. (2011). Microgravity droplet combustion: effect of tethering fiber on burning rate and flame structure. *Combustion Theory and Modelling*, *15*(4), 487-515.

Farouk, T., & Dryer, F. L. (2012). Tethered methanol droplet combustion in carbon-dioxide enriched environment under microgravity conditions. *Combustion and Flame*, *159*(1), 200-209.

Farrell, J. T., N. P. Cernansky, F. L. Dryer, D. G. Friend, C. A. Hergart, C. K. Law, R. M. McDavid, C. J. Mueller, A. K. Patel. and H. Pitsch. (2007). Development of an experimental database and kinetic models for surrogate diesel fuels. *SAE World Congress & Exhibition*, 201.

Fayaz, H., Mujtaba, M., Soudagar, M. E. M., Razzaq, L., Nawaz, S., Nawaz, M. A., Farooq, M., Afzal, A., Ahmed, W., & Khan, T. Y. (2021). Collective effect of ternary nano fuel blends on the diesel engine performance and emissions characteristics. *Fuel*, *293*, 120420.

Fiorina, B., Vié, A., Franzelli, B., Darabiha, N., Massot, M., Dayma, G., Dagaut, P., Moureau, V., Vervisch, L., & Berlemont, A. (2016). Modeling challenges in computing aeronautical combustion chambers. *Aerospace lab,* 11, 1-19.

Gad, M. S., Abdel Razek, S. M., Manu, P., & Jayaraj, S. (2021). Experimental investigations on diesel engine using alumina nanoparticle fuel additive. *Advances in Mechanical Engineering*, *13*(2).

Gan, Y., & Qiao, L. (2012). Radiation-enhanced evaporation of ethanol fuel containing suspended metal nanoparticles. *International Journal of Heat and Mass Transfer*, *55*(21-22), 5777-5782.

Ghassemi, H., Baek, S. W., & Khan, Q. S. (2006). Experimental study on binary droplet evaporation at elevated pressures and temperatures. *Combustion Science and Technology*, *178*(6), 1031-1053.

Godsave, G. (1953). Studies of the combustion of drops in a fuel spray—the burning of single drops of fuel. *Symposium (international) on combustion*, 4(1), 818-830.

Grosshans, H., Griesing, M., Mönckedieck, M., Hellwig, T., Walther, B., Gopireddy, S. R., Sedelmayer, R., Pauer, W., Moritz, H.-U., & Urbanetz, N. A. (2016). Numerical and experimental study of the drying of bi-component droplets under various drying conditions. *International Journal of Heat and Mass Transfer*, *96*, 97-109.

Hagan, M. T., Demuth, H. B., & Beale, M. (1997). *Neural network design*. PWS Publishing Co.

Han, K., Song, G., Ma, X., & Yang, B. (2016). An experimental and theoretical study of the effect of suspended thermocouple on the single droplet evaporation. *Applied Thermal Engineering*, *101*, 568-575.

Haynes, W. M. (2016). *CRC handbook of chemistry and physics*. CRC press.

Huang, Y., & Yang, V. (2009). Dynamics and stability of lean-premixed swirl-stabilized combustion. *Progress in Energy and Combustion Science*, *35*(4), 293-364.

Hubbard, G., Denny, V., & Mills, A. (1975). Droplet evaporation: effects of transients and variable properties. *International Journal of Heat and Mass Transfer*, *18*(9), 1003-1008.

Huber, M. L., Lemmon, E. W., & Bruno, T. J. (2010). Surrogate mixture models for the thermophysical properties of aviation fuel Jet-A. *Energy & Fuels*, *24*(6), 3565-3571.

IEA. (2022). World energy outlook 2022.

Jackson, G., & Avedisian, C. (1998). Combustion of unsupported water-in-n-heptane emulsion droplets in a convection-free environment. *International Journal of Heat and Mass Transfer*, *41*(16), 2503-2515.

Jang, S. P., & Choi, S. U. (2004). Role of Brownian motion in the enhanced thermal conductivity of nanofluids. *Applied Physics Letters*, *84*(21), 4316-4318.

Javed, I., Baek, S. W., & Waheed, K. (2013a). Evaporation characteristics of heptane droplets with the addition of aluminum nanoparticles at elevated temperatures. *Combustion and Flame*, *160*(1), 170-183.

Javed, I., Baek, S. W., Waheed, K., Ali, G., & Cho, S. O. (2013b). Evaporation characteristics of kerosene droplets with dilute concentrations of ligand-protected aluminum nanoparticles at elevated temperatures. *Combustion and Flame*, *160*(12), 2955-2963.

Javed, I., Baek, S. W., & Waheed, K. (2014). Effects of dense concentrations of aluminum nanoparticles on the evaporation behavior of kerosene droplet at elevated temperatures:

The phenomenon of microexplosion. *Experimental Thermal and Fluid Science*, 56, 33-44.

Johnson, D. D. (1981). Nextel 312 ceramic fiber from 3M. *Journal of Coated Fabrics*, *10*(4), 282-296.

Jüngst, N., Smallwood, G., & Kaiser, S. (2022). Visualization and image analysis of droplet puffing and micro-explosion in spray-flame synthesis of iron oxide nanoparticles. *Experiments in Fluids*, *63*(3), 60.

Kee, R. J., Coltrin, M. E., & Glarborg, P. (2005). *Chemically reacting flow: theory and practice*. John Wiley & Sons.

Khond, V. W., & Kriplani, V. (2016). Effect of nanofluid additives on performances and emissions of emulsified diesel and biodiesel fueled stationary CI engine: A comprehensive review. *Renewable and Sustainable Energy Reviews*, *59*, 1338-1348.

Kim, D., Martz, J., & Violi, A. (2014). A surrogate for emulating the physical and chemical properties of conventional jet fuel. *Combustion and Flame*, *161*(6), 1489-1498.

Kim, D., & Violi, A. (2018). Hydrocarbons for the next generation of jet fuel surrogates. *Fuel*, *228*, 438-444.

Kim, D., & Violi, A. (2021). On the importance of species selection for the formulation of fuel surrogates. *Proceedings of the Combustion Institute*, *38*(4), 5615-5624.

Kryukov, A., Levashov, V. Y., & Sazhin, S. (2004). Evaporation of diesel fuel droplets: kinetic versus hydrodynamic models. *International Journal of Heat and Mass Transfer*, 47(12-13), 2541-2549.

Kumagai, S., Sakai, T., & Okajima, S. (1971). Combustion of free fuel droplets in a freely falling chamber. *Symposium (International) on Combustion,* 13(1), 779-785.

Lai, Y.-W., & Pan, K.-L. (2023). Disruption and microexplosion mechanisms of burning alcohol droplets with the addition of nanoparticles. *Combustion and Flame*, 256, 112958.

Lasheras, J., Fernandez-Pello, A., & Dryer, F. (1980). Experimental observations on the disruptive combustion of free droplets of multicomponent fuels. *Combustion Science and Technology*, *22*(5), 195-209.

Laurent, C., Biscos, Y., Doué, N., Maqua, C., Lemoine, F., Gréhan, G., & Lavergne, G. (2006). Thermal gradient determination inside vaporizing droplets by combining rainbow and laser induced fluorescence measurements. *Fluids Engineering Division Summer Meeting,* 909-916.

Law, C. K. (1982). Recent advances in droplet vaporization and combustion. *Progress in Energy and Combustion Science*, *8*(3), 171-201.

Lefebvre, A. H., & Ballal, D. R. (2010). *Gas turbine combustion: alternative fuels and emissions*. CRC press.

Liñán Martínez, A. (1985). Theory of droplet vaporization and combustion.

P.J. Linstrom, W.G. Mallard. (2001). NIST Chemistry Webbook, NIST Standard Reference Database Number 69, National Institute of Standards and Technology, Gaithersburg, M.D., USA.

Lippert, A. M. (1999). *Modeling of multicomponent fuels with application to sprays and simulation of diesel engine cold start*. The University of Wisconsin-Madison (PhD thesis).

Liu, Y. C., Farouk, T., Savas, A. J., Dryer, F. L., & Avedisian, C. T. (2013). On the spherically symmetrical combustion of methyl decanoate droplets and comparisons with detailed numerical modeling. *Combustion and Flame*, *160*(3), 641-655.

Long, W., Yi, P., Jia, M., Feng, L., & Cui, J. (2015). An enhanced multi-component vaporization model for high temperature and pressure conditions. *International Journal of Heat and Mass Transfer*, *90*, 857-871.

Luo, L., & Liu, Y. C. (2021). Variation of gas phase combustion properties of complex fuels during vaporization: Comparison for distillation and droplet scenarios. *Proceedings of the Combustion Institute*, *38*(2), 3287-3294.

Ma, X., Zhang, F., Han, K., Yang, B., & Song, G. (2015). Evaporation characteristics of acetone–butanol–ethanol and diesel blends droplets at high ambient temperatures. *Fuel*, *160*, 43-49.

Mao, Y., Xia, J., Ruan, C., Wu, Z., Feng, Y., Zhu, J., Wang, S., Yu, L., & Lu, X. (2021). An experimental and kinetic modeling study of a four-component surrogate fuel for RP-3 kerosene. *Proceedings of the Combustion Institute*, *38*(1), 555-563.

Marzo, A., Barnes, A., & Drinkwater, B. W. (2017). TinyLev: A multi-emitter single-axis acoustic levitator. *Review of Scientific Instruments*, *88*(8).

Matthews, H. D., Gillett, N. P., Stott, P. A., & Zickfeld, K. (2009). The proportionality of global warming to cumulative carbon emissions. *Nature*, *459*, 829-832.

Maxwell, J. C. (1890). *Collected Scientific Papers. Vol. 2*. CUP.

McBride, B. J. (1993). *Coefficients for calculating thermodynamic and transport properties of individual species* (Vol. 4513). National Aeronautics and Space Administration, Office of Management.

Mei, D., Fang, Y., Zhang, D., Guo, D., & Chen, Z. (2023). Evaporation and micro-explosion performances of nano-fuel droplets. *Fuel*, *334*, 126623.

Meinshausen, M., Meinshausen, N., Hare, W., Raper, S. C., Frieler, K., Knutti, R., Frame, D. J., & Allen, M. R. (2009). Greenhouse-gas emission targets for limiting global warming to 2 C. *Nature*, *458*(7242), 1158-1162.

Miller, R., Harstad, K., & Bellan, J. (1998). Evaluation of equilibrium and non-equilibrium evaporation models for many-droplet gas-liquid flow simulations. *International Journal of Multiphase Flow*, *24*(6), 1025-1055.

Muelas, Á. (2021). *Experimental characterization and modeling of liquid fuel combustion. From pure compounds to real fuels.* Universidad de Zaragoza (PhD thesis).

Muelas, Á., Carpio, J., Ballester, J., Sánchez, A. L., & Williams, F. A. (2020). Pyrolysis effects during high-temperature vaporization of alkane droplets. *Combustion and Flame*, *217*, 38-47.

Muelas, Á., Remacha, P., & Ballester, J. (2019). Droplet combustion and sooting characteristics of UCO biodiesel, heating oil and their mixtures under realistic conditions. *Combustion and Flame*, *203*, 190-203.

Muelas, Á., Aranda, D., & Ballester, J. (2019). Alternative method for the formulation of surrogate liquid fuels based on evaporative and sooting behaviors. *Energy & Fuels*, *33*(6), 5719-5731.

Mueller, C. J., Cannella, W. J., Bruno, T. J., Bunting, B., Dettman, H. D., Franz, J. A., Huber, M. L., Natarajan, M., Pitz, W. J., & Ratcliff, M. A. (2012). Methodology for formulating diesel surrogate fuels with accurate compositional, ignition-quality, and volatility characteristics. *Energy & Fuels*, *26*(6), 3284-3303.

Niranjan, R., & Thakur, A. K. (2017). The toxicological mechanisms of environmental soot (black carbon) and carbon black: focus on oxidative stress and inflammatory pathways. *Frontiers in Immunology*, *8*, 763.

Noh, D., Gallot-Lavallée, S., Jones, W. P., & Navarro-Martinez, S. (2018). Comparison of droplet evaporation models for a turbulent, non-swirling jet flame with a polydisperse droplet distribution. *Combustion and Flame*, *194*, 135-151.

Nomura, H., Ujiie, Y., Rath, H. J., Sato, J. i., & Kono, M. (1996). Experimental study on high-pressure droplet evaporation using microgravity conditions. Symposium (International) on Combustion, 26(1), 1267-1273.

Otsu, N. (1979). A threshold selection method from gray-level histograms. *IEEE Transactions on Systems, Man, and Cybernetics*, *9*(1), 62-66.

Perry, J. H. (1950). *Chemical engineers' handbook*. ACS Publications.

Philp, R. P. (1994). High temperature gas chromatography for the analysis of fossil fuels: a review. *Journal of High Resolution Chromatography*, *17*(6), 398-406.

Pinheiro, A. P., Rybdylova, O., Zubrilin, I. A., Sazhin, S. S., Sacomano Filho, F. L., & Vedovotto, J. M. (2021). Modelling of aviation kerosene droplet heating and evaporation using complete fuel composition and surrogates. *Fuel*, *305*, 121564.

Pitz, W. J., Cernansky, N. P., Dryer, F. L., Egolfopoulos, F., Farrell, J., Friend, D. G., & Pitsch, H. (2007). Development of an experimental database and chemical kinetic models for surrogate gasoline fuels. *SAE Transactions*, 195-216.

Pitz, W. J., & Mueller, C. J. (2011). Recent progress in the development of diesel surrogate fuels. *Progress in Energy and Combustion Science*, *37*(3), 330-350.

Poling, B. E., Prausnitz, J. M., & O'connell, J. P. (2001). *Properties of gases and liquids*. McGraw-Hill Education.

Potts, H., Barrett, R., & Diver, D. (2001). Dynamics of freely-suspended drops. *Journal of Physics D: Applied Physics*, *34*(17), 2529.

Poulton, L., Rybdylova, O., Zubrilin, I., Matveev, S., Gurakov, N., Al Qubeissi, M., Al-Esawi, N., Khan, T., Gun'ko, V. M., & Sazhin, S. (2020). Modelling of multi-component kerosene and surrogate fuel droplet heating and evaporation characteristics: A comparative analysis. *Fuel*, *269*, 117115.

Prasher, R., Bhattacharya, P., & Phelan, P. E. (2005). Thermal conductivity of nanoscale colloidal solutions (nanofluids). *Physical Review Letters*, *94*(2), 25901.

Ra, Y., & Reitz, R. D. (2009). A vaporization model for discrete multi-component fuel sprays. *International Journal of Multiphase Flow*, *35*(2), 101-117.

Rapp, B. E. (2022). *Microfluidics: modeling, mechanics and mathematics*. Elsevier.

Raza, A., Latif, R., Raza, M., & Shafi, I. (2018). Numerical modelling of diesel fuel multiphase evaporation in heavy duty diesel engine. *Proceedings of the 21st Australasian Fluid Mechanics Conference (AFMC), Adelaide, Australia (10-13)*.

Rehman, H. L.-u., Weiss, J., & Seers, P. (2016). Effect of heat conduction on droplet life time and evaporation rate under forced convection at low temperatures. *Experimental Thermal and Fluid Science*, *72*, 59-66.

Renksizbulut, M., Bussmann, M., & Li, X. (1992). A droplet vaporization model for spray calculations. *Particle & Particle Systems Characterization*, *9*(4), 59-65.

Riazi, M. (2005). *Characterization and properties of petroleum fractions* (Vol. 50). ASTM international.

Rosebrock, C. D., Shirinzadeh, S., Soeken, M., Riefler, N., Wriedt, T., Drechsler, R., & Mädler, L. (2016). Time-resolved detection of diffusion limited temperature gradients inside single isolated burning droplets using rainbow refractometry. *Combustion and Flame*, *168*, 255-269.

Saltelli, A., Ratto, M., Andres, T., Campolongo, F., Cariboni, J., Gatelli, D., Saisana, M., & Tarantola, S. (2008). *Global sensitivity analysis: the primer*. John Wiley & Sons.

Sánchez, A. L., Urzay, J., & Liñán, A. (2015). The role of separation of scales in the description of spray combustion. *Proceedings of the Combustion Institute*, *35*(2), 1549-1577.

Sarathy, S. M., Farooq, A., & Kalghatgi, G. T. (2018). Recent progress in gasoline surrogate fuels. *Progress in Energy and Combustion Science*, *65*, 67-108.

Sazhin, S. (2014). *Droplets and sprays* (Vol. 345). Springer.

Sazhin, S. S. (2006). Advanced models of fuel droplet heating and evaporation. *Progress in Energy and Combustion Science*, *32*(2), 162-214.

Sazhin, S. S., Al Qubeissi, M., Kolodnytska, R., Elwardany, A., Nasiri, R., & Heikal, M. (2014). Modelling of biodiesel fuel droplet heating and evaporation. *Fuel*, *115*, 559-572.

Sazhin, S. S., Elwardany, A., Krutitskii, P., Castanet, G., Lemoine, F., Sazhina, E. M., & Heikal, M. R. (2010). A simplified model for bi-component droplet heating and evaporation. *International Journal of Heat and Mass Transfer*, *53*(21-22), 4495-4505.

Setyawan, H. Y., Zhu, M., Zhang, Z., & Zhang, D. (2015). An experimental study of effect of water on ignition and combustion characteristics of single droplets of glycerol. *Energy Procedia*, *75*, 578-583.

Setyawan, H. Y., Zhu, M., Zhang, Z., & Zhang, D. (2016). Ignition and combustion characteristics of single droplets of a crude glycerol in comparison with pure glycerol, petroleum diesel, biodiesel and ethanol. *Energy*, *113*, 153-159.

Shaddix, C., & Hardesty, D. (1999). Combustion properties of biomass flash pyrolysis oils: final project report. (No. SAND99-8238). Sandia National Lab, Albuquerque, NM, United States.

Shashank, E. K., Knudsen, E., & Pitsch, H. (2011). Spray evaporation model sensitivities. *Annual Research Briefs*, 213-224.

Sirignano, W. A. (1983). Fuel droplet vaporization and spray combustion theory. *Progress in Energy and Combustion Science*, *9*(4), 291-322.

Sirignano, W. A. (2010). *Fluid dynamics and transport of droplets and sprays*. Cambridge University Press.

Skeel, R. D., & Berzins, M. (1990). A method for the spatial discretization of parabolic equations in one space variable. *SIAM Journal on Scientific and Statistical Computing*, *11*(1), 1-32.

Spalding, D. B. (1950). Combustion of liquid fuels. *Nature*, *165*(4187), 160-160.

Sparrow, E., & Gregg, J. (1958). The variable fluid-property problem in free convection. *Transactions of the American Society of Mechanical Engineers*, *80*(4), 879-886.

Su, M., & Chen, C. (2015). Heating and evaporation of a new gasoline surrogate fuel: a discrete multicomponent modeling study. *Fuel*, *161*, 215-221.

Szymkowicz, P. G., & Benajes, J. (2018). Development of a diesel surrogate fuel library. *Fuel*, *222*, 21-34.

Tanvir, S., & Qiao, L. (2012). Surface tension of nanofluid-type fuels containing suspended nanomaterials. *Nanoscale Research Letters*, *7*, 1-10.

Tanvir, S., & Qiao, L. (2015). Effect of addition of energetic nanoparticles on droplet-burning rate of liquid fuels. *Journal of Propulsion and Power*, *31*(1), 408-415.

Turns, S. R. (1996). *Introduction to combustion*. McGraw-Hill Companies, New York, USA.

Verwey, C., & Birouk, M. (2018). Experimental investigation of the effect of natural convection on the evaporation characteristics of small fuel droplets at moderately elevated temperature and pressure. *International Journal of Heat and Mass Transfer*, *118*, 1046-1055.

Viswanath, D. S., Ghosh, T. K., Prasad, D. H., Dutt, N. V., & Rani, K. Y. (2007). *Viscosity of liquids: theory, estimation, experiment, and data*. Springer Science & Business Media.

Wang, J., Huang, X., Qiao, X., Ju, D., & Sun, C. (2020). Experimental study on effect of support fiber on fuel droplet vaporization at high temperatures. *Fuel*, *268*, 117407.

Wang, J., Qiao, X., Ju, D., Wang, L., & Sun, C. (2019). Experimental study on the evaporation and micro-explosion characteristics of nanofuel droplet at dilute concentrations. *Energy*, *183*, 149-159.

Wang, J., Wang, X., Chen, H., Jin, Z., & Xiang, K. (2018). Experimental study on puffing and evaporation characteristics of jatropha straight vegetable oil (SVO) droplets. *International Journal of Heat and Mass Transfer*, *119*, 392-399.

Wang, Y., Chen, Z., Haefner, M., Guo, S., DiReda, N., Ma, Y., Wang, Y., & Avedisian, C. T. (2021). Combustion of n-butyl acetate synthesized by a new and sustainable biological process and comparisons with an ultrapure commercial n-butyl acetate produced by conventional Fischer esterification. *Fuel*, *304*, 121324.

Warnatz, J., Maas, U., Dibble, R. W., & Warnatz, J. (2006). *Combustion: Physical and Chemical Fundamentals, Modeling and Simulation, Experiments, Pollutant Formation*. Springer.

Williams, A. (2013). *Combustion of liquid fuel sprays*. Butterworth-Heinemann.

Williams, F. A. (2018). *Combustion theory*. CRC Press.

Wise, H., & Agoston, G. A. (1958). Burning of a liquid droplet. ACS Publications.

Wu, M., & Yang, S. (2016). Combustion characteristics of multi-component cedar bio-oil/kerosene droplet. *Energy*, *113*, 788-795.

Wu, Y., Li, H., Wu, X., Gréhan, G., Mädler, L., & Crua, C. (2019). Change of evaporation rate of single monocomponent droplet with temperature using time-resolved phase rainbow refractometry. *Proceedings of the Combustion Institute*, *37*(3), 3211-3218.

Xuan, Y., Li, Q., & Hu, W. (2003). Aggregation structure and thermal conductivity of nanofluids. *AIChE Journal*, *49*(4), 1038-1043.

Yang, G., Yang, Z., He, Y., Shi, Z., & Dong, T. (2023). Evaporation Issues of Acoustically Levitated Fuel Droplets. *Ultrasonics Sonochemistry*, 106480.

Yang, J.-R., & Wong, S.-C. (2001). On the discrepancies between theoretical and experimental results for microgravity droplet evaporation. *International Journal of Heat and Mass Transfer*, *44*(23), 4433-4443.

Yang, J.-R., & Wong, S.-C. (2002). An experimental and theoretical study of the effects of heat conduction through the support fiber on the evaporation of a droplet in a weakly convective flow. *International Journal of Heat and Mass transfer*, *45*(23), 4589-4598.

Yang, S., & Wu, M. (2017). The droplet combustion and thermal characteristics of pinewood bio-oil from slow pyrolysis. *Energy*, *141*, 2377-2386.

Yao, T., Pei, Y., Zhong, B.-J., Som, S., Lu, T., & Luo, K. H. (2017). A compact skeletal mechanism for n-dodecane with optimized semi-global low-temperature chemistry for diesel engine simulations. *Fuel*, *191*, 339-349.

Yaws, C. L. (1995). *Handbook of Thermal Conductivity, Volume 2: Organic Compounds C5 to C7*. Elsevier.

Yi, P., Li, T., Fu, Y., & Xie, S. (2021). Transcritical evaporation and micro-explosion of ethanol-diesel droplets under diesel engine-like conditions. *Fuel*, *284*, 118892.

Yu, W., & Choi, S. (2004). The role of interfacial layers in the enhanced thermal conductivity of nanofluids: a renovated Hamilton–Crosser model. *Journal of Nanoparticle Research*, *6*, 355-361.

Zhang, Y., Huang, R., Huang, Y., Huang, S., Ma, Y., Xu, S., & Zhou, P. (2018). Effect of ambient temperature on the puffing characteristics of single butanol-hexadecane droplet. *Energy*, *145*, 430-441.

Zhang, Y., Huang, R., Xu, S., Huang, Y., Huang, S., Ma, Y., & Wang, Z. (2017). The effect of different n-butanol-fatty acid methyl esters (FAME) blends on puffing characteristics. *Fuel*, *208*, 30-40.

Zhang, Y., Huang, R., Zhou, P., Huang, S., Zhang, G., Hua, Y., & Qian, Y. (2021). Numerical study on the effects of experimental parameters on evaporation characteristic of a droplet. *Fuel*, *293*, 120323.